ABSTRACT

HIGH PRESSURE EFFECTS ON ELECTRON TRANSPORT AND STRUCTURE OF COLOSSAL MAGNETORESISTIVE MATERIALS

by
Congwu Cui

Pressure effects on the electronic, magnetic properties and structure of several typical colossal magnetoresistive manganites, $La_{0.60}Y_{0.07}Ca_{0.33}MnO_3$, $Pr_{1-x}Ca_xMnO_3$ (x = 0.25, 0.30, 0.35), $Nd_{1-x}Sr_xMnO_3$ (x = 0.45, 0.50), were explored through high pressure resistivity and structure measurements. It was shown that pressure up to ~7 GPa induces more complicated charge, spin and lattice state changes than in the low pressure range explored previously. In $La_{0.60}Y_{0.07}Ca_{0.33}MnO_3$, pressure induces a local atomic structure transformation at a critical point P*, and hence, a non-monotonic change in metal-insulator (MI) transition temperature (T_{MI}) and spin state. In $Pr_{0.75}Ca_{0.25}MnO_3$, with pressure increase, T_{MI} increases and T_C decreases below P* and the trend is reversed above P*. In $Pr_{0.7}Ca_{0.3}MnO_3$, pressure induces reentrant electronic and magnetic states: between ~0.8-5 GPa, T_{MI} and T_C are coupled and have a behavior similar to $La_{0.60}Y_{0.07}Ca_{0.33}MnO_3$, outside of this range, T_{MI} and T_C are decoupled and at low and high pressure the material is insulating. In all three $Pr_{1-x}Ca_xMnO_3$ compounds, charge ordering is suppressed below P*. Above P*, an insulating state with unknown conducting mechanism is induced. In $Nd_{1-x}Sr_xMnO_3$, at x = 0.45, in addition to the effect on T_{MI}, pressure possibly induces an A-type antiferromagnetic phase. For x = 0.5, the charge ordering transition temperature is increased, which is different from $Pr_{1-x}Ca_xMnO_3$ system. The effects of chemical doping (bandwidth) and pressure are not equivalent in the high pressure range. This is unlike the results in the low pressure range acquired by other groups previously. A universal P* exists for samples with metal-insulator transitions.

HIGH PRESSURE EFFECTS ON ELECTRON TRANSPORT AND STRUCTURE OF COLOSSAL MAGNETORESISTIVE MATERIALS

by
Congwu Cui

A Dissertation
Submitted to the Faculty of
New Jersey Institute of Technology and Rutgers,
The State University of New Jersey-Newark
In Partial Fulfillment of the Requirements for the Degree of
Doctor of Philosophy in Applied Physics

Federated Physics Department

May 2003

APPROVAL PAGE

HIGH PRESSURE EFFECTS ON ELECTRON TRANSPORT AND STRUCTURE OF COLOSSAL MAGNETORESISTIVE MATERIALS

Congwu Cui

Trevor A. Tyson, Dissertation Advisor — Date
Associate Professor of Applied Physics, NJIT

Gordon A. Thomas — Date
Professor of Applied Physics, NJIT

Ken K. Chin — Date
Professor of Applied Physics, NJIT

John F. Federici — Date
Associate Professor of Applied Physics, NJIT

Zhen Wu — Date
Associate Professor of Physics, Rutgers, The State University of New Jersey - Newark

BIOGRAPHICAL SKETCH

Author: Congwu Cui

Degree: Doctor of Philosophy

Date: May 2003

Undergraduate and Graduate Education:

- Doctor of Philosophy in Applied Physics, Federated Physics Department, New Jersey Institute of Technology, Newark, NJ, 2003 and Rutgers, the State University of New Jersey - Newark, Newark, NJ, 2003

- Master of Science in Physics, University of Science and Technology, Beijing, Beijing, P. R. China, 1995

- Bachelor of Science in Physics, University of Science and Technology, Beijing, Beijing, P. R. China, 1990

Major: Applied Physics

Publications and Presentations:

Congwu Cui, Trevor A. Tyson, Zhong Zhong, Jeremy P. Carlo, and Yuhai Qin, "Effects of pressure on electron transport and atomic structure of manganites: Low to high pressure regimes", Phys. Rev. B, 67, 104107 (2003).

Congwu Cui and Trevor A. Tyson, "High-pressure induced reentrant electronic and magnetic state in $Pr_{0.7}Ca_{0.3}MnO_3$ manganite", Submitted to Phys. Rev. Lett.

Congwu Cui and Trevor A. Tyson, "High pressure study on electron transport and structure of $Nd_{0.55}Sr_{0.45}MnO_3$ and $Nd_{0.5}Sr_{0.5}MnO_3$", manuscript to be submitted.

Congwu Cui and Trevor A. Tyson, "Effects of high pressure and bandwidth on metal-insulator transition in manganites", manuscript in preparation.

Congwu Cui and Trevor A. Tyson, "Electron transport and structure of narrow bandwidth manganite $Pr_{1-x}Ca_xMnO_3$ under pressure", manuscript in preparation.

Congwu Cui and Trevor A. Tyson, "High pressure studies of metal-insulator-transitions in manganites: Effect on bandwidth", American Physics Society Meeting, Mar., 2003. Oral report.

Congwu Cui and Trevor Tyson, "High-pressure effects on local structure of manganites", 2001 Summer School Synchrotron Radiation Applications, Beijing, August 27 - September 5, 2001. Invited talk.

Congwu Cui and Trevor Tyson, "High-pressure transport and structural studies of manganites", American Physics Society Meeting, Mar. 2001, Oral report.

Congwu Cui, Trevor A. Tyson, and Jeremy P. Carlo, "Electron-lattice interactions in manganites probed by high pressure transport and structural measurements", International Workshop Electron-Phonon Effects in Nanosystems, 2002. Poster

Congwu Cui and Trevor A. Tyson, J. Ablett and C.-C. Kao, "Transport properties and local structure of manganites under high-pressure", 2nd AIMS Materials Research Symposium. Poster.

To my beloved family

ACKNOWLEDGMENT

I would like to thank Prof. Trevor A. Tyson, my academic advisor, both for his excellent academic support with valuable and extensive knowledge and insight to keys in physics related fields, and for his support in financial and even personal things. To Prof. Gordon Thomas, Prof. Ken K. Chin, Prof. John F. Federici and Prof. Zhen Wu, I would like to give my special thanks for serving as committee members and providing valuable guidance.

The author is very thankful to: Dr. Zhong Zhong, Dr. Jingzhu Hu, Dr. Chi-Chang Kao and Dr. James Ablett at National Synchrotron Light Source (NSLS) for their assistance in x-ray absorption, x-ray diffraction (XRD) and pressure calibration; and Dr. Ho-Kwang Mao, Dr. Jian Xu and Dr. Jinfu Shu at Geophysical Laboratory at Carnegie Institution of Washington for help in high pressure techniques. Jeremy P. Carlo and Yuhai Qin are thanked for making one sample and help in sample characterization, respectively.

This work was funded by National Science Foundation Career Grant DMR-9733862 and DOE Grant DE-FG02-97ER45665.

The high pressure XRD measurements were performed at beamline X17B1, NSLS, Brookhaven National Laboratory (BNL) which is funded by Department of Energy. Pressure calibrations in XRD measurements were performed with the equipments belonging to X17C, at NSLS, BNL.

My family is also worthy of my thanks. My parents have always been a solid support. In my four years of study, they have been taking care my daughter. My dear wife has been supportive by taking care of home and baby at the expense of her own higher education. I am indebted to my daughter, Yuyang, and son, Alex, for being a father who did not spend much time with them. This dissertation contains more than just scientific and technical results. It is also composed of the forever-lasting love of my family.

TABLE OF CONTENTS

TABLE OF CONTENTS
(Continued)

TABLE OF CONTENTS
(Continued)

TABLE OF CONTENTS
(Continued)

LIST OF TABLES

LIST OF FIGURES

LIST OF FIGURES
(Continued)

LIST OF FIGURES
(Continued)

LIST OF FIGURES
(Continued)

LIST OF FIGURES
(Continued)

Figure **Page**

CHAPTER 1

COLOSSAL MAGNETORESISTANCE BASICS

1.1 Introduction

In the 1950s, the large magnetoresistance (MR) effect in $La_{1-x}Ca_xMnO_3$ [1, 2] and $La_{0.8}Sr_{0.2}MnO_3$ [3] had been investigated. In the last decade, the mixed valence manganites attracted renewed attention because of the extremely high MR effect observed in thin films.[4,5] Hence, the name colossal magnetoresistance (CMR) was associated with these materials. The renewed interest was based on the possibility of new applications as devices and on the use of the materials as a tool to understand the physics of strongly correlated electron physics due to the strong electron, spin and lattice correlation exhibited by these materials.

The CMR materials are promising material for applications, such as magnetic record, magnetic sensors and other new magnetic electronic functions due to the magnetic field, pressure, x-ray, VI-IR laser, electrical field/current effects. At present, although no functional device has been made, some possible applications have been proposed.[6,7] Since at the metal-insulator transition (MIT) the resistance change occurs over a relatively narrow temperature range, it is accompanied by very large temperature coefficients of resistance in the region of phase transition, making these materials ideal for IR optoelectronic devices controlled by thermal and magnetic fields.[8,9] Several patents have been applied, such as: memory device with the $A_{1-x}B_xMnO_3$ (A = La, Pr, Nd, or Sm; B = Ca, Sr, or Ba; $x > 0.17$) Mn oxides[10] which comprises of a magnetic device of two magnetic layers sandwiching a granular magnetic film of $A_{1-x}B_xMnO_3$ in a dielectric matrix; high-temperature magnetic refrigerating working medium.[11] A principle device (Figure 1.1) of epitaxial heterostructure of a ferromagnet $La_{2/3}Sr_{1/3}MnO_3$, an insulator La_2CuO_4 and a high-T_C superconductor $DyBa_2Cu_3O_7$ has been fabricated, in which

current injected from the ferromagnetic layer reduces the critical current of the superconductor significantly. This is attributed to weakening of superconductivity by the injection of spin-polarized carriers into the superconductor. It is possible that fast switching devices based on this phenomenon could be fabricated.[12]

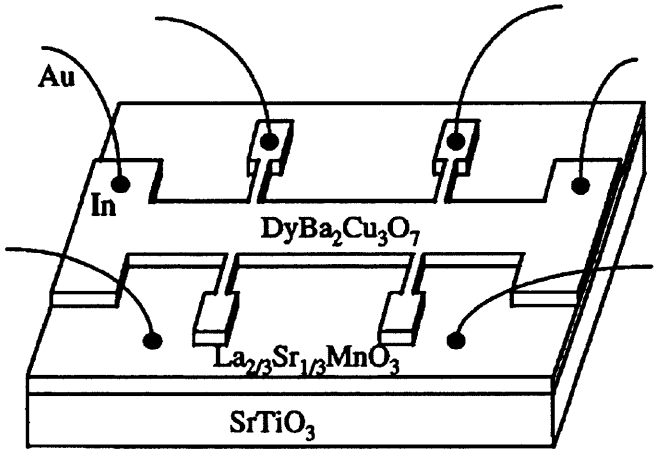

Figure 1.1 Geometry of a pilot device using colossal magnetoresistive material and superconductor.

Note: the width of the $DyBa_2Cu_3O_7$ bridge is 300 μm, and the distance between the voltage leads is 3 mm. The substrate is 6 x 6 mm^2 in area.[12]

In this class of complex transition metal oxides, there are abundant physical phenomena, such as ferromagnetic metal (FMM) to paramagnetic insulator (PMI) transition, Chare/orbital ordering (CO/OO), double exchange (DE), superexchange (SE), Jahn-Teller distortion (JTD) and the complex interactions between them. The manganites are good prototypes of correlated electron systems where spin, charge, orbital degrees of freedom, and lattice effects are correlated. Neglecting any interaction leads to large difference from experimental results. Therefore, they can be used to test various condensed matter physics theories. Understanding manganites will also shed light on other questions in condensed matter physics, such as the high Tc superconductor mechanism.

1.1.1 Colossal Magnetoresistance

The magnetoresistance is the relative change of resistance/resistivity in external magnetic field. It is generally defined as:

$$MR = \frac{\rho(H) - \rho(0)}{\rho(0)} \times 100\% \tag{1.1}$$

where $\rho(H)$ and $\rho(0)$ are the resistances with and without magnetic field at given temperature. Generally for CMR materials, MR is very close to ~100%.[5] To emphasize this very large MR, an alternative definition of the MR is also used:

$$MR' = \frac{\rho(H) - \rho(0)}{\rho(H)} \times 100\% \tag{1.2}$$

in this way, the MR may get to millions percent.[5,13] That is where the "colossal" comes to distinguish it from the traditional MR or the so-called giant magnetoresistance (GMR), which is only of the order of 10%, in magnetic multilayers alternatively deposited with different metals.

In the GMR multilayers, the ferromagnetic layers are spaced by a layer of nonmagnetic metal layers, each of them is only a few nanometers thick. If the thickness of the space layer is chosen properly, the coupling between adjacent ferromagnetic layers is antiferromagnetic. An external magnetic field can override this coupling and hence, decrease the angle between magnetic alignments. This in turn reduces the electron scattering on the boundary and leads to an electrical resistance decrease. Grünberg *et al.*[14] first reported this effect. They investigated the exchange coupling of Fe layers across Au and Cr interlayers. For Au interlayers, the coupling decreases continuously to zero as the Au thickness is increased from 0 to 20 Å. For Cr interlayers with proper thickness, the coupling between Fe layers can be antiferromagnetic. Figure 1.2 is the magnetoresistance of a typical magnetic multilayer $[Fe/Cr]_{40}$.

Most of the CMR materials are the chemically doped manganites $A_{1-x}B_xMnO_3$, where A is a trivalent element, such as La, Y, Pr, Nd, Sm, Eu, Gd, Bi, etc.; B is a divalent element, like Ca, Ba, Sr, Pb, etc. The other kind of interesting CMR materials is the

layered-structure manganites, which is characterized by the Ruddlesden-Poper series $(A_{1-x}B_x)_{n+1}Mn_nO_{3n+1}$. This thesis focuses on the cubic system. More details about the layered manganites can be found in several reviews.[15,16,17,18,19]

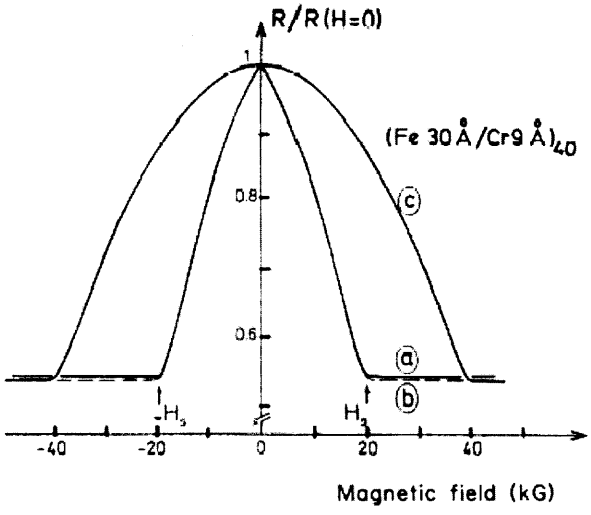

Figure 1.2 The magnetoresistance of a Fe/Cr multilayer at 4.2 K.

Note: the current is along [110] and the field is in the layer plane along the current direction (curve a), in the layer plane perpendicular to the current (curve b) or perpendicular to the layer plane (curve c). The resistivity at zero field is 54 μΩ.cm.[20]

1.2 Basic Physics in CMR Materials

1.2.1 Brief Facts about Parent Compounds

All the manganites can be regarded as the trivalent element substitution in parent compounds, such as $LaMnO_3$, $PrMnO_3$, $NdMnO_3$, with divalent element. A typical parent compound is $LaMnO_3$ with an ideal cubic perovskite structure (Figure 1.3). Due to the size mismatch between Mn and La ions, the structure is distorted orthorhombically (Figure 1.4) or rhombohedrally. The orthorhombic distortion of $LaMnO_3$ leads the MnO_6 octahedra to tilt in long range - coherent static Jahn-Teller distortion. The Mn-O-Mn bond angle decreases from the ideal 180°. The structure symmetry is Pbnm and the lattice parameters at 1.5 K are listed in Table 1.1. Rodríguez-Carvajal *et al.*[21] listed more data at room and high temperatures about this compound.

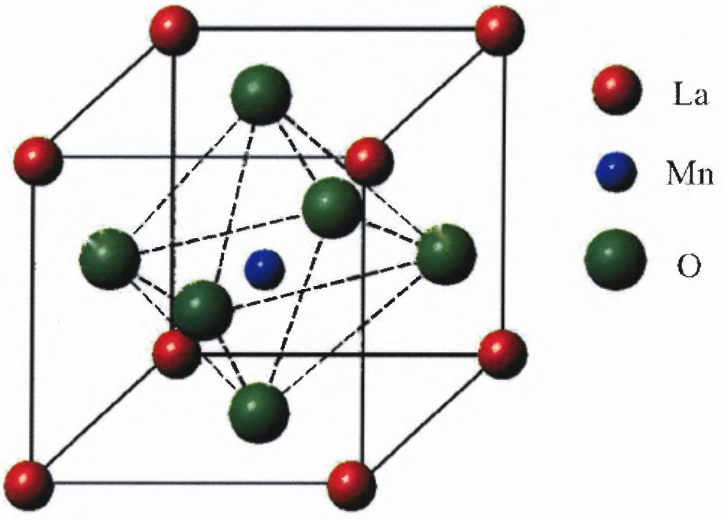

Figure 1.3 Ideal perovskite structure.

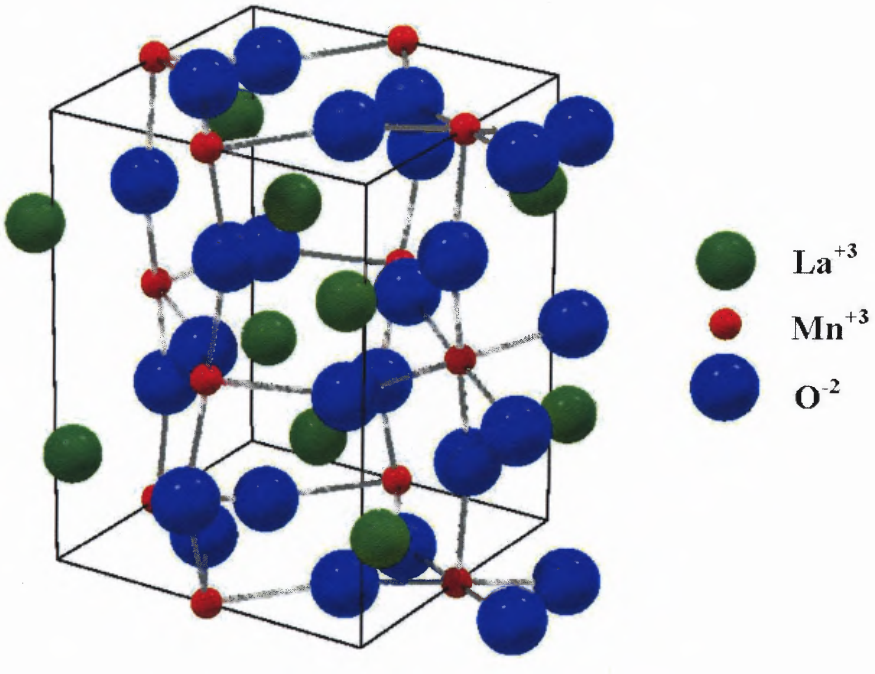

Figure 1.4 Distorted perovskite structure ($LaMnO_3$).

Note: the figure was drawn with the data in Table 1.1.

Table 1.1 $LaMnO_3$ Structure Parameters at 1.5 K

	x	y	z
La (4c)	-0.0095	0.0513	1/4
Mn (4b)	1/2	0	0
O1 (4c)	0.0777	0.4849	1/4
O2 (8d)	0.7227	0.3085	0.0408

Note: the space group is Pbnm, Z = 4; a = 5.5333(2) Å, b = 5.7461(2) Å, c = 7.6637(4) Å, Mn-O1 = 1.966(1) Å, Mn-O2 = 1.914(3) Å and 2.181(3) Å.[22]

In ambient environment, the symmetry of many manganites is orthorhombic Pbnm. With the symmetry distortion, there is also a Jahn-Teller distortion of the MnO_6 octahedra. The 5-fold degenerate 3d orbitals of Mn^{3+} ion are split by the distorted octahedral crystal fields into two subgroups: 3 t_{2g} orbitals (d_{xy}, d_{yz}, d_{zx}) and two e_g orbitals ($d_{x^2-y^2}$, $d_{3z^2-r^2}$) (Figure 1.5). The electronic structure is $t_{2g}^3 e_g^1$. The 3 t_{2g} electrons are tightly bound to the Mn Site to form a core spin with S = 3/2. Because of strong Hund's rule interaction, the spin of the e_g electron is parallel to the core spin. In the high spin Mn^{3+}: $t_{2g}^3 e_g^1$ ion, e_g^1 electron occupies a 2-fold degenerate orbital. This orbital freedom makes the Mn^{3+} a strong Jahn-Teller active ion and makes orbital ordering possible. Due to the 3d orbital splitting, Fermi level lies in the gap so that the material is insulating (Figure 1.5). At low temperature, the spin structure is A-type (Figure 1.6) antiferromagnetic with a Néel temperature at ~120K.

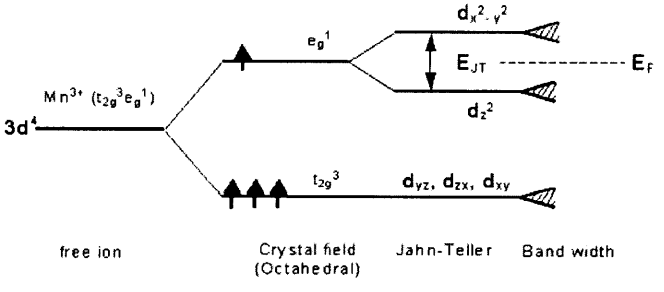

Figure 1.5 Energy level scheme of $LaMnO_3$.[23]

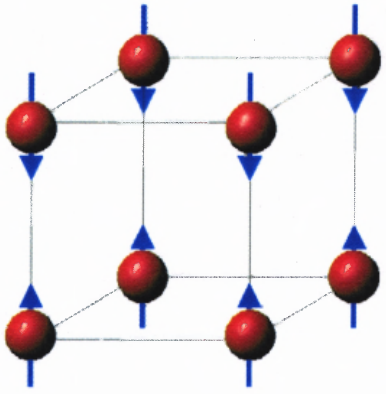

Figure 1.6 A-type antiferromagnetic magnetic structure.

In manganites, there are several energy parameters play crucial role in their various properties:

1) on-site d-d Coulomb energy U, the energy of creating a $d^{n+1}d^{n-1}$ charge excitation in an array of d^n ions;
2) charge transfer energy Δ_{CT}, the energy of transferring an O^{2-} 2p electron to the neighboring Mn 3d orbital to create a charge excitation which leaves a hole in the oxygen 2p orbital: $Mn^{3+}:3d^4O^{2-}:2p^6 \Rightarrow Mn^{2+}:3d^5O^{1-}:2p^5$;
3) p-d transfer integral t (carrier hoping), which determines the 3d electron bandwidth W ($W = 2Zt$, where Z is the number of Mn nearest neighbors[18]);
4) Hund's rule magnetic coupling energy J_H (= $U_{ex}/2$, where U_{ex} is the on-site exchange interaction energy to flip a d-electron spin[18]);
5) crystal field splitting Δ_{CF} (10Dq), the energy difference between the e_g orbital and t_{2g} orbital split by the MnO_6 octahedral crystal field;
6) Jahn-Teller split energy Δ_{JT}, the energy difference between the two e_g orbitals split by Jahn-Teller effect;
7) intra-atomic exchange J between neighboring Mn sites;[24]

For the compound $LaMnO_3$, electronic structure calculations show that these energies are all of the order of 1 eV (Table 1.2). The parameters produce small difference in total

energy in the structural and magnetic states of manganites. The close separation in energy makes easy for the delicate balances between these energies to be modified by changes in temperature, chemical doping, pressure, strain, magnetic field, etc. These factors have lead to fascinating property changes in CMR materials.

Table 1.2 Electronic Structure Energy Parameters of $LaMnO_3$

U	8-10[a], 4.0[b], 7.8[c]	W=12t	2.4[a], 1.0[b], 1.8[c]	Δ_{CF}	2.0[a], 1.8[b]
Δ_{CT}	4.5[b, c]	$J_H=U_{ex}/2$	1.5[a], 1.0[b]	Δ_{JT}	1.5[a], 0.6[b]
J	0.86[a]				

Note: the unit is eV; [a]: results from ref. 24; [b]: results from ref. 18; [c]: results from ref. 25.

1.2.2 Chemically Doped Manganites

Chemical doping is the primary method used to study and acquire various properties of manganites. By choosing different trivalent elements, e.g. La, Pr, Nd, Sm, Eu, Gd, Bi, and the doping divalent elements, like Ca, Sr, Ba, and Pb, and by changing the doping concentration in different systems of $A_{1-x}B_xMnO_3$, complicated phase diagrams with abundant magnetic, electronic and structure phases have been acquired (Figure 1.7).

By chemical doping, two important parameters can be modified: the band filling 1-x (or doping concentration x); the bandwidth W.

In parent compound, there are 4 d electrons in the Mn^{3+} 3d band. By substituting the trivalence ion with divalence element, the charge carrier density of 3d band is changed. The average electron number in 3d band is 4-x, or x holes are induced.

In addition to band filling, the bandwidth W is also modified. The different doping element and concentration change the average A-site ion size $\langle r_A \rangle$ $[= r_A(1-x)+r_B x]$ or equivalently the tolerance factor t.[26,27] With t ($\langle r_A \rangle$) decreasing/increasing, Mn-O-Mn bond angles decrease/increase. The W of manganite is correlated to the overlap of Mn 3d orbital and O^{2-} 2p orbital. So bandwidth is correspondingly modified by chemical doping.

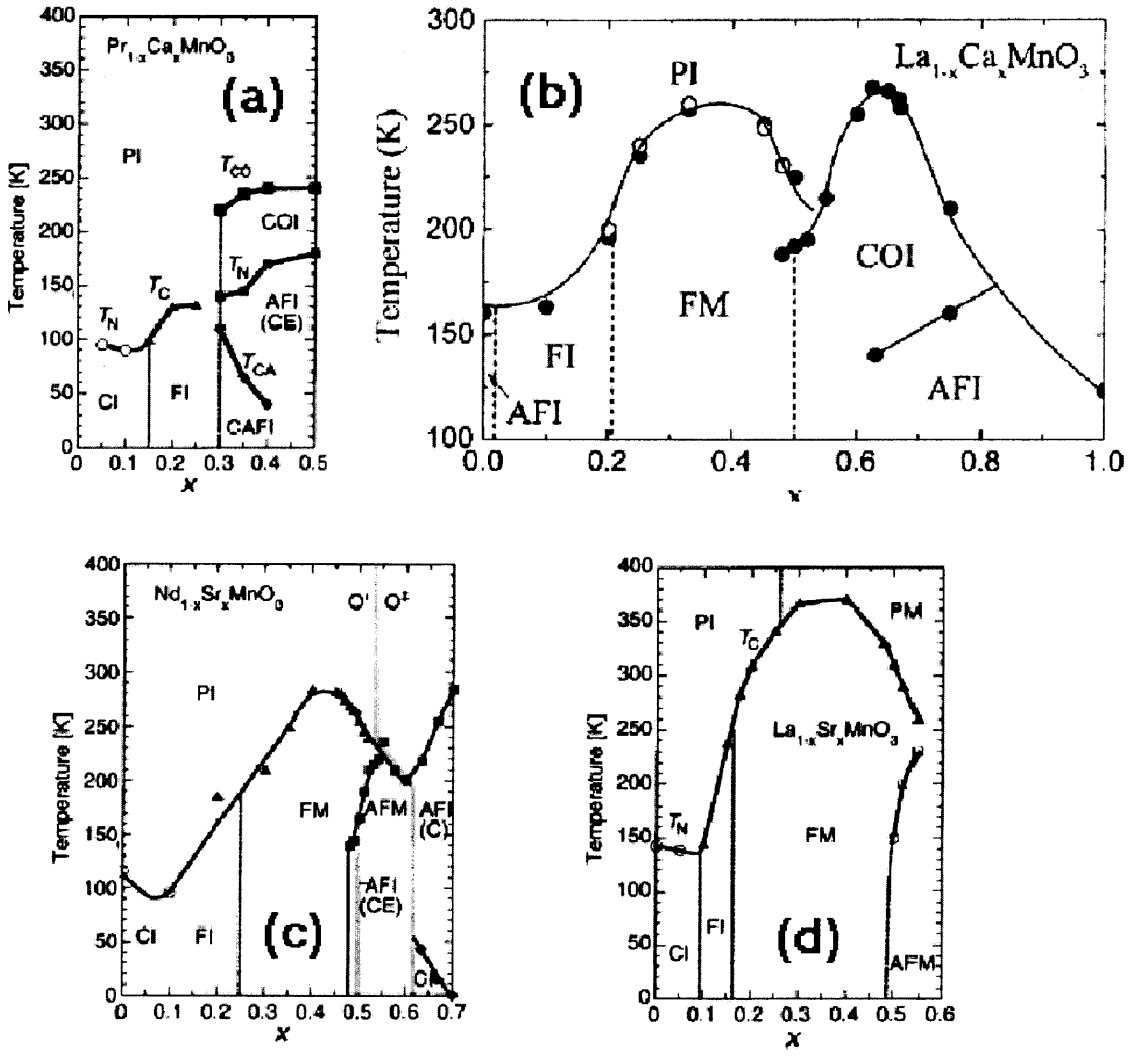

Figure 1.7 Magnetic and electronic phase diagrams of typical CMR systems.

Note: (a) $Pr_{1-x}Ca_xMnO_3$; (b) $La_{1-x}Ca_xMnO_3$; (c) $Nd_{1-x}Sr_xMnO_3$; (d) $La_{1-x}Sr_xMnO_3$. The denotations: PI: paramagnetic insulating; PM: paramagnetic metallic; CI: spin-canted insulating states; FI: ferromagnetic insulating; FM: ferromagnetic metallic; AFM: antiferromagnetic (A-type) metallic states; COI: charge-ordered insulating; CAFI: canted antiferromagnetic insulating. [(a), (c), (d) are reproduced from ref. 15; (b) is reproduced from ref. 28 and 16].

In the phase diagrams in Figure 1.7, in the (La, Sr)MnO_3, (La, Ca)MnO_3 and (Nd, Sr)MnO_3 systems, in the doping range of 0.2~0.5, there is a ferromagnetic metal to paramagnetic insulator transition which implies the coupled electronic transport and magnetic ordering. This is qualitatively explained by the double exchange theory. In other doping concentrations and in the (Pr, Ca)MnO_3 system with large ion size

mismatch, the materials are insulating, but with more complicated magnetic phases.

The very complicated electronic, magnetic and structure phase diagrams result from the subtle balances between the charge, spin and lattice structure interactions tuned by chemical doping. For different doping system, the system with smaller A-site atom has larger orthorhombic distortion. With t ($<r_A>$) decreasing from (La, Sr)MnO_3, through (Nd, Sr)MnO_3 to (Pr, Ca)MnO_3, the orthorhombic distortion increase, inducing the Mn-O-Mn bond bending and therefore, the decreasing of bandwidth W. However, from the phase diagrams, it can be seen that the bandwidth is not the only factor determining the CMR properties. In fact, it has been shown that the bandwidth effect is very small that only account for several percent of the experiment results. Another important factor is lattice distortion, especially the Jahn-Teller distortion. By introducing divalent elements, the lattice distortion is also changed to contribute to the various electronic and magnetic phases.

1.2.3 CMR Origins

For manganites, when an external magnetic field is applied, the resistivity can be greatly suppressed, displaying very large negative magnetoresistance effect. This negative MR originates from three different mechanisms according to the magnetic field effects on the spin states, charge states and the long range and local structure of the materials.

1.2.3.1 Magnetic Field Induced Spin Alignment. This is the so-called double exchange system. A typical compound is the $La_{1-x}Sr_xMnO_3$ (x = ~0.2-0.3) system. The characteristic is the metal-insulator transition accompanied by the ferromagnetic-paramagnetic magnetic transition.

Although the electron-lattice interaction is strong so that the resistivity is much larger than that calculated with the DE model, the spin ordering is the most obvious reason of the large magnetoresistance. The resistance comes from spin disordering. While

transported, electrons are scattered by the spin disorder. According to DE theory, the hoping rate of Mn^{3+} e_g electron to its neighbor Mn^{4+} site is proportional to $\cos(\theta/2)$, where θ is the relative angle between the neighboring localized t_{2g} electron spins (S=3/2). When an external magnetic field is applied, the disordered spins are aligned, the Curie temperature T_C is shifted to higher temperature, the resistance is also suppressed, resulting large negative magnetoresistance (Figure 1.8). The MR can be expressed as: $MR \sim C(M/M_s)^2$, where M and M_s are the magnetization and saturation magnetization respectively, C is a scaling constant.[15,29,30]

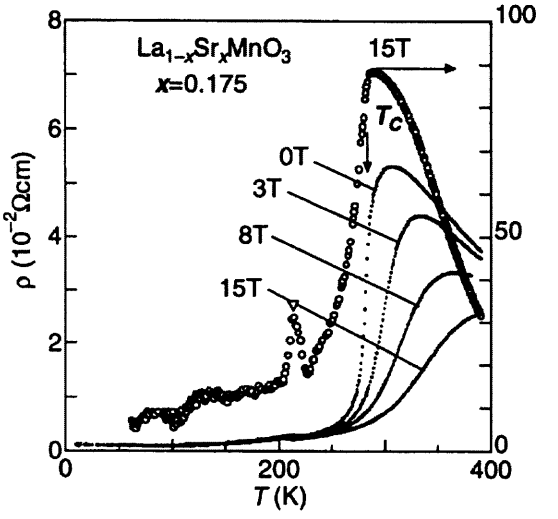

Figure 1.8 Temperature dependence of resistivity of $La_{0.825}Sr_{0.175}MnO_3$ in magnetic field.

Note: open circles represent the magnetoresistance in a magnetic field of 15 T.[15]

1.2.3.2 Magnetic Field Induced Charge Ordering Collapse. In charge ordering state, electrons are localized by strong lattice distortion. The material is in AFM or PM state and insulating. The double exchange induced electron hoping between Mn^{3+} and Mn^{4+} sites is destructive to the CO state. An external magnetic field can change the spin states, leading to CO state collapse into FMM state and hence, inducing large MR. Two typical examples are $Nd_{0.5}Sr_{0.5}MnO_3$ and $Pr_{1-x}Ca_xMnO_3$ ($x = 0.3 \sim 0.5$).

In $Nd_{0.5}Sr_{0.5}MnO_3$, there is a metal-insulator transition at T_C = ~255 K. Upon

cooling, CO state arises from the FMM state accompanied by a transition to AFM state at $T_{CO} = T_N = \sim 160$ K [Figure 1.9(c)], indicating the competition between CO state and FMM state. When a magnetic field high enough is applied, the charge order state is destroyed and $\sim 10^6$ % MR is induced (Figure 1.9 A-D).

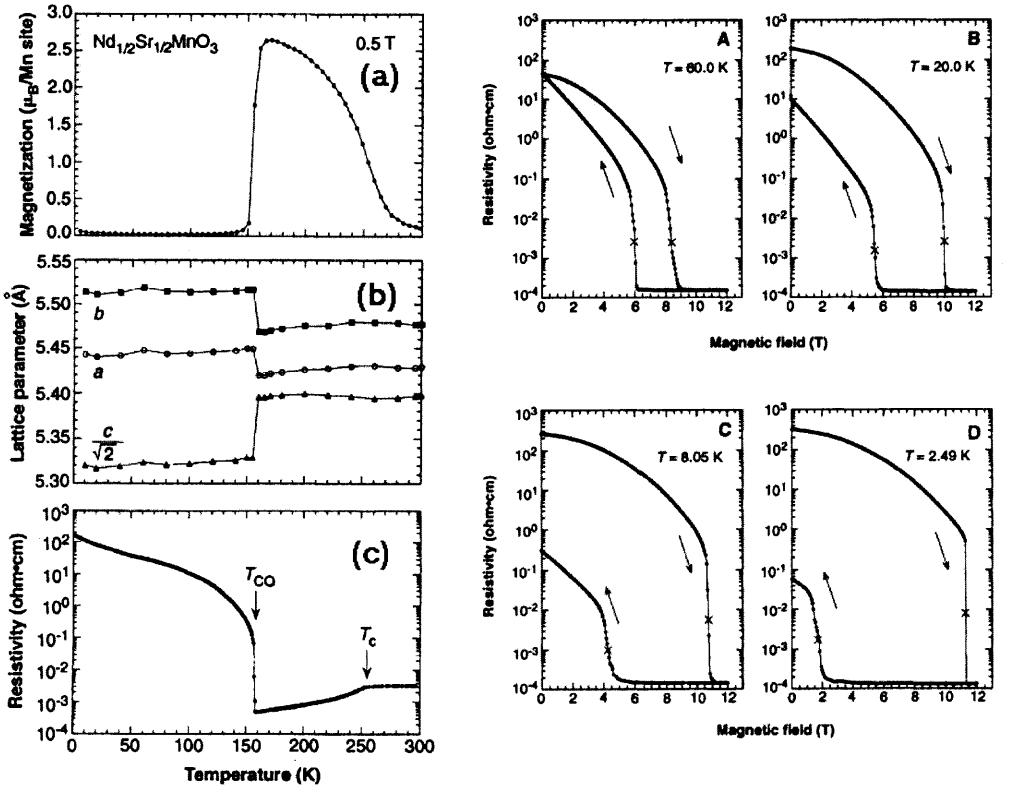

Figure 1.9 $Nd_{1/2}Sr_{1/2}MnO_3$ properties.

Note: left panel: temperature dependence of magnetization (a), lattice parameters (b), and resistivity (c). T_{CO} and T_C are charge ordering and Curie temperature respectively. Right panel: the magnetic field dependence of resistivity at different temperature. (Reproduced from Ref 31)

In $Pr_{1-x}Ca_xMnO_3$ (x = 0.3~0.5), because of the small $<r_A>$, the crystal local structure is highly distorted so that the electrons are tightly localized. The CO state is strong and doping dependent. No metallic phase appears in this system in the whole doping range. A magnetic field can melt the CO state and induce a metallic state at low temperature. The MR below the transition temperature can be larger than 10^{10} % (Figure 1.10).

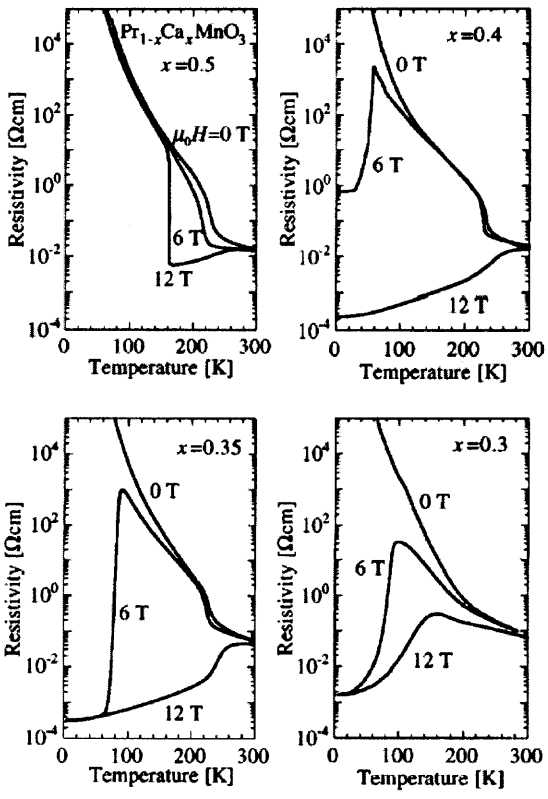

Figure 1.10 Temperature dependence of resistivity of $Pr_{1-x}Ca_xMnO_3$ in magnetic field.[32]

1.2.3.3 Magnetic Field Induced Crystal Structure Transition. Some manganites have structure transitions from orthorhombic to rhombohedral structure with temperature, pressure and/or doping. Although rare, it was found that external magnetic field can induce such a transition and result magnetoresistance due to structure changing[33] (Figure 1.11).

1.2.4 CMR Physics

In the doped manganites, there exist various charge, spin and structure states and complicated interactions between them. These interactions and their relative strength cause the complicated electronic, magnetic properties. Some important interactions will be briefly reviewed below.

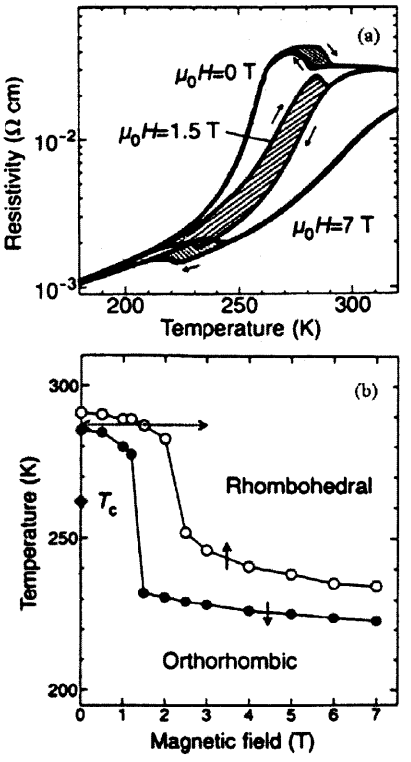

Figure 1.11 Magnetic field induced structure transition on $La_{0.83}Sr_{0.17}MnO_3$.

Note: (a) Temperature dependence of resistivity in different fields, the hatched regions represent the hysteresis loop of the structure phase transition between rhombohedral form (high temperature phase) and orthorhombic one (low temperature phase); (b) structure phase diagram in magnetic field, The filled circles represent the rhombohedral ($R\bar{3}c$) to orthorhombic (Pbnm) phase transition in the cooling run, the open circles represent the reversed process. (Reproduced from ref. 33)

1.2.4.1 Double Exchange. To explain the strong correlation between conductivity and the ferromagnetism and the value of zero temperature saturation magnetization corresponding to the sum of all unpaired electron spins in $La_{1-x}A_xMnO_3$, Zener[34] proposed the double exchange theory which was further developed by Anderson[35] and De Gennes.[36]

The theory involves the real hoping of electrons from Mn^{3+} (d^4, $t_{2g}^3e_g^1$, $S_c = 2$) to Mn^{4+} (d^3, $t_{2g}^3e_g^0$, $S_c = 3/2$) via the O^{2-} 2p orbital, as: $Mn^{3+}O^{2-}Mn^{4+} \rightarrow Mn^{4+}O^{2-}Mn^{3+}$. The Mn^{3+} e_g conductive electron is ferromagnetically coupled to the on-site t_{2g} electrons because of the strong Hund's rule interaction. In order to hop from a Mn site i to the neighboring Mn site j, the spin of the e_g electron must change from parallel to S_c^i to

parallel to S_c^j. Ferromagnetically ordered core spins minimize the kinetic energy needed for hoping, while antiferromagnetically ordered ones maximize it. Only electrons with spins parallel to the t_{2g} electrons contribute to conductivity while hoping among the Mn sites. The spin disorder leads to electron scattering, and therefore, high resistance.

DE is always a ferromagnetic coupling and sensitive to the Mn-O-Mn local structure. The bending of the Mn-O-Mn bond results the canting of spins and a narrower bandwidth. This reduces the hoping probability of electrons and correspondingly, the conductivity. The hoping rate or the transfer integral between two neighboring Mn site is expressed as:

$$t_{ij} = t_{ij}^0 \cos(\frac{\theta_{ij}}{2}) \tag{1.3}$$

where t_{ij}^0 is the transfer integral that depends on the spatial wave functions, θ_{ij} is the relative angle between two neighboring spins.

The DE theory successfully explains the coupled ferromagnetism and conductivity qualitatively. When spins are disordered, resistivity is much higher due to the low hoping probability. In an external magnetic field, spins are aligned, hence, the hoping rate is increased and high negative magnetoresistance is induced.

In equation (1.3), both t_{ij}^0 and θ_{ij} are local structure related and can be modified by chemical substitution of the trivalent elements with divalent elements and other methods. Because it is over-simplified, the conductivity estimated with it is much higher than observed in experiments. Millis *et al.*[37,38] argued that DE alone cannot explain the resistivity of CMR and electron-lattice interaction induced by Jahn-Teller type lattice distortion of the MnO_6 octahedra should be considered.

In ideal case, the Mn e_g orbital is twofold degenerate. The JTD of the MnO_6 octahedra lowers the local cubic symmetry to tetragonal at Mn^{3+} site. This induces strong electron-phonon coupling. The energy gained by formation of a local lattice distortion can be ~0.6 eV per site, which is much greater than the electron kinetic energy.[39] The

strong electron-phonon coupling "self-traps" the conduction electrons at high temperatures and hence, forms polarons.[37] The competition between the self-trap energy E_{JT} and the electron itinerancy energy that can be parameterized by effective hoping matrix element t_{eff}, can lead to the CMR phenomenon. Millis *et al.*[38,40,41] incorporated the dynamic Jahn-Teller effect into DE theory to explain the resistivity difference between DE theoretical predication and experimental results:

The Hamiltonian of the model is expressed as:

$$H_{eff} = H_{el} + H_{JT} \tag{1.4}$$

with

$$H_{el} = -\sum_{ij\alpha} t_{ij}^{ab} d_{ia\alpha}^{+} d_{jb\alpha} + J_H \sum_{ia\alpha} \vec{S_c^i} \cdot d_{ia\alpha}^{+} \vec{\sigma} d_{ia\alpha} + \vec{h} \cdot \vec{S_c} / S_c \tag{1.5}$$

and

$$H_{JT} = g \sum_{ja\sigma} d_{ja\sigma}^{+} Q^{ab}(j) d_{jb\sigma} + \frac{k}{2} \sum_{j} Q^2(j) \tag{1.6}$$

where $d_{ia\sigma}^{+}$ creates an outer-shell d electron of spin σ in the a orbital on site i; $\vec{S}_c^{\,i}$ is the core spin at i site; h is the external magnetic field; g is the electron-phonon coupling; k is the phonon stiffness. The local lattice distortions causes the JT splitting transform as a twofold degenerate representation of the cubic group which is parameterized by magnitude r and angle Φ. They couple to the electron as a traceless symmetric matrix $\mathbf{Q} = r[\cos(\phi)\tau_z + \sin(\phi)\tau_x]$. The electron-phonon coupling is characterized by a dimensionless parameter λ, which is defined as $\lambda = g/\sqrt{kt}$. The external magnetic field aligns the spins and increases the kinetic energy, hence, suppresses the effective electron-phonon coupling, resulting a large resistivity decrease. With the decreasing of effective electron-phonon coupling, large magnetoresistance is induced when the system across the metal-insulator transition.

Figure 1.12 is the resistivity with and without magnetic field. It is calculated by solving the Hamiltonian via dynamical mean field approximation. The calculated results

reproduce most features of experimental results, implying that electron-phonon coupling play important role in CMR physics.

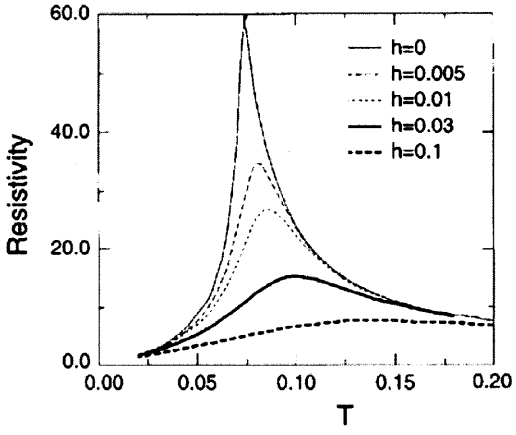

Figure 1.12 Calculated temperature dependence of resistivity at different values of magnetic field h for $\lambda = 1.12$.

Note: the parameter h is related to the physical field h_{phys} by $h = g\,\mu_B S_c h_{phys}/t$. Using $g = 2$, $t = 0.6$ eV, and $S_c = 3/2$ means $h = 0.01$ corresponds to $h_{phys} = 15$ T.[41]

1.2.4.2 Superexchange. Superexchange describes the interaction between neighboring magnetic cations well separated by a non-magnetic anion. Kramers[42] first pointed out the possibility of superexchange spin coupling through an intermediate non-magnetic atom. The superexchange was found theoretically and experimentally to have three different magnetic characteristics:[43,44,45,46,47]

When a filled e_g orbital and an empty one overlap opposite ends of an anion, the coupling is ferromagnetic (direct exchange between the e_g orbital and the t_{2g} shell);

When two empty e_g orbitals overlap an anion from each side, the coupling is a weaker antiferromagnetic (π-bond superexchange of the t_{2g} shells);

When two filled e_g orbitals overlap an anion from each side, the coupling is strong antiferromagnetic (ordinary superexchange between e_g (σ) orbitals).

Specifically for manganites, the superexchange coupling between Mn^{3+} and Mn^{4+} is ferromagnetic, that between two Mn^{4+} cations is antiferromagnetic. The superexchange

between two Mn^{3+} cations is a little complicated. It can be either ferromagnetic or antiferromagnetic, depending on the Mn-Mn distance. The coupling is antiferromagnetic when the distance is small, and ferromagnetic while the distance is large. When the Mn-Mn distance is large enough, the coupling is paramagnetic as indicated by Goodenough[48] because there is no indirect magnetic exchange between Mn ions.

In the case of Mn^{3+} and Mn^{4+} coupling through O^{2-} anion, because both the double exchange and the superexchange involve the interaction in the same Mn-O-Mn bond, confusion may arise: what exactly is the difference between these two exchanges?

In 1955, Goodenough[48] explained it by taking account of lattice: in a lattice with disordered Mn^{3+} and Mn^{4+} ions, the state of Mn^{3+}-O^{2-}-Mn^{4+} and Mn^{4+}-O^{2-}-Mn^{3+} is degenerate, so that below Curie temperature the e_g electron can hop between the two Mn ions, which is the case of double exchange. In an ordered lattice, the distance between Mn^{3+} and Mn^{4+} is large, the degeneracy is removed so that the double exchange is inhibited.

With crystal field theory, Anderson[47] expressed superexchange effect in terms of two parameters: Coulomb repulsive energy of d-electrons U and transfer integral t:

$$J_{eff} = 2\frac{t^2}{U} \tag{1.7}$$

because the transfer integral t and the Coulomb energy U relate to the local structure: Mn-O-Mn bond angle and Mn-Mn distance, the superexchange strongly depends on the bond angles[49] and Mn-Mn distance.[48]

The development of modern theories have proved that the superexchange is more complicatedly affected by many parameters, such as the cooperative static and/or dynamic Jahn-Teller distortions, electron-phonon interactions, etc. The strength of superexchange correlates to bandwidth W. In coupling Mn^{3+}-O^{2-}-Mn^{4+}, the bond is σ-type, the ferromagnetic coupling is due to strong e_g electron coupling to the oxygen displacements along the Mn-O-Mn bond axis.[50,51] When bandwidth W_σ is increased to

approach the small polaron stabilization energy $\hbar\omega_R$, where ω_R^{-1} is the time for the optical breathing mode to trap a carrier at a single cation site, a transition of electron state from localized to itinerant occurs. The ferromagnetic $e_g^1 - p_\sigma - e_g^0$ interactions changes from superexchange to double exchange. The superexchange varies as $\cos(\theta_{ij})$ while double exchange as $\cos(\theta_{ij}/2)$.[52] The bandwidth can be increased by applying hydrostatic pressure, choosing large A-site cations, or applying magnetic field.

It was shown that superexchange coupling is necessary for different spin ordering (F, A, G type) accompanied by CO, depending on inter-site Coulomb interaction U and SE coupling J.[53] Mryasov *et al.*[54] indicated that global and internal lattice distortions dramatically influence the character of exchange interactions in $LaMnO_3$: global distortions associated with variations of apical Mn-O bond length promotes DE contribution; bending of Mn-O bonds in ab-plane suppresses DE and promotes antiferromagnetic SE contribution to the interlayer exchange energy.

In $Pr_{0.7}Ba_{0.3}MnO_3$, a distinct ferromagnetic insulating state was found between T_C (~180 K) and metal-insulator transition (120 K) by Heilman *et al.*[55] They ascribed it to the suppress of the FM DE interactions relative to the competing FM superexchange interactions caused by the large A-site cation size mismatch.

In $La_{1-x}Sr_xMnO_3$, $0.1 \leq x \leq 0.15$, the compound shows a ferromagnetic and insulating ground state followed by a canted antiferromagnetic phase at higher temperatures. The ferromagnetic transition is strongly coupled to a structural transition from Jahn-Teller distorted phase to pseudocubic orthorhombic phase. Paraskevopoulos *et al.*[56] ascribed it to orbital ordering due to the interplay of superexchange interactions and Jahn-Teller distortions. This antiferromagnetic-type orbital ordering in the pseudocubic phase can enhance the ferromagnetic superexchange interaction, so that magnetic field can lead to phase transition from a ferromagnetic metallic phase to a ferromagnetic insulating phase.[57]

Substituting Mn atom with Al in $LaMnO_3$ forms a rhombohedral $LaMn_{1-x}Al_xO_{3+\delta}$

series ($0 \leq x \leq 20\%$). Krishnan and Banerjee[58] studied the electron transport properties. They found that there is a progressive crossover from ferromagnetic-metallic state to ferromagnetic-insulating state that all samples are ferromagnetic below transition temperature, but only the samples with $x \leq 5\%$ exhibit a metal-insulator transition at T_C while the samples with $x \geq 10\%$ are all semiconducting above and below T_C. While the systematic crossover from a double exchange dominated regime to an exclusively superexchange regime, the system preserves the rhombohedral symmetry. To explain the non-trivial temperature dependence of metallic resistivity in the medium x range, one needs to take into account superexchange interactions even in the double exchange dominated regime.

1.2.4.3 Charge Ordering. Charge ordering in manganites is the ordering of Mn^{3+}/Mn^{4+} in real space. In electron diffraction, CO reveals itself as a superlattice modulation to the fundamental Bragg reflections.[59] The CO has been observed in different manganite systems.[15,23,60,61]

Charge ordering is the result of competition between long-range Coulomb interactions between atoms and bandwidth. CO happens in compounds with narrow bandwidth W in which electrons is localized to Mn sites. With bandwidth decrease, Coulomb interaction among atoms becomes relatively important. When the Coulomb interaction is comparable to bandwidth, two sets of lattice, Mn^{4+} and Mn^{3+}, form (Figure 1.13). Although CO can exist in any doping concentration, when x is a rational number, CO state is much easier to form and more robust.

Bandwidth is directly determined by lattice structure. Structure distortion, such as orthorhombic distortion, static coherent Jahn-Teller distortion and Mn-O-Mn bond angle, reduce W. The study to CO has built up intimate relation between lattice distortions and CO. The lattice distortion can be modified by changing the A-site ion size $\langle r_A \rangle$ or the tolerance factor t. So CO state extensively exists in compounds with small $\langle r_A \rangle$ (Figure 1.14). It was found that T_{CO} decreases almost linearly with increasing $\langle r_A \rangle$.[62] The most

direct condition to form CO is electron localization. Therefore, any factors affecting electron localization state changes CO state. Chemical doping is one of the methods. Other examples, such as high pressure can suppress local structure distortion to destroy CO state and magnetic field can do so by aligning spins to increase the electron mobility.

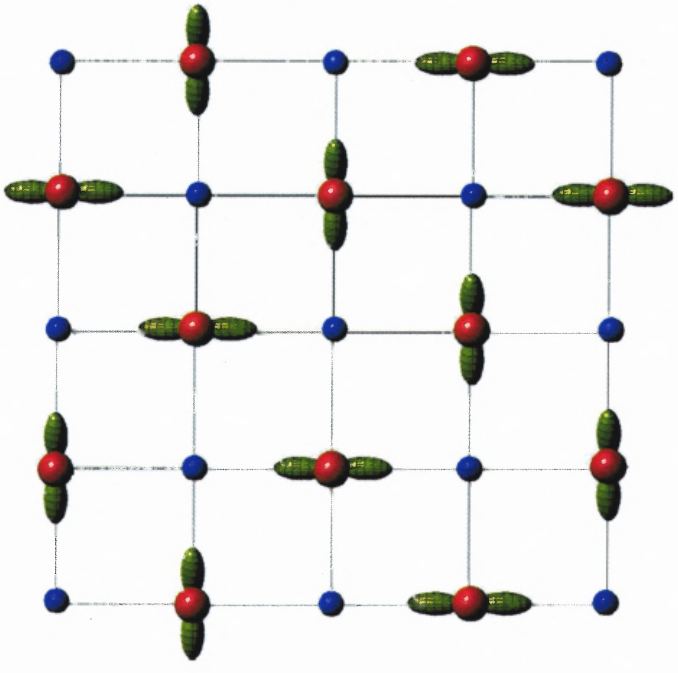

Figure 1.13 Sketch of combined charge and orbital order at x=1/2.

Note: the bare ball is Mn^{4+}, the ball with lobe is Mn^{3+}, the ordered orbital is $d_{3x^2-r^2}$ and $d_{3y^2-r^2}$.

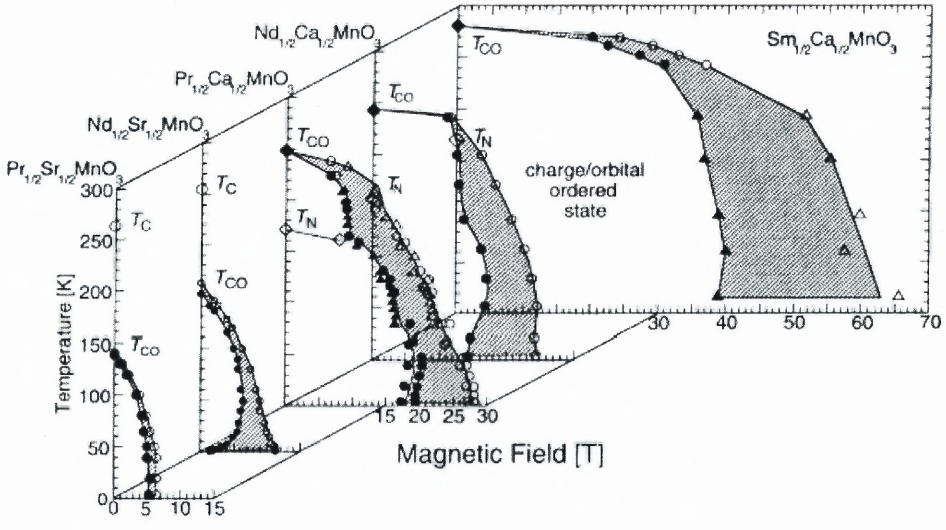

Figure 1.14 The charge/orbital-ordered phase of various $RE_{1/2}AE_{1/2}MnO_3$.[15]

1.2.4.4 Orbital Ordering. In Mn^{3+}, one electron occupies the doubly degenerate e_g orbital, there is an orbital freedom of e_g electron between $d_{x^2-y^2}$ and $d_{3z^2-r^2}$. This freedom is strongly coupled to charge, spin and lattice through its shape and extension direction and can affect the ordering structure, charge and spin dynamics.[63] Theoretical works indicate that the orbital state needs to be considered to explain the complicated electronic and magnetic states.[64,65,66]

The orbital states can be controlled with external fields, such as magnetic, stress, electric fields and electromagnetic radiation fields. The electric field may directly affect the direction of OO, if the compound has high dielectric strength, the magnetic state may also be changed.[67] A new elementary excitation, orbiton, caused by the symmetry breaking of OO is proposed and observed in $LaMnO_3$ with Raman spectroscopy.[68]

Orbital ordering is coupled to lattice distortion, especially coherent static JTD. The electron energy can be lowered by Jahn-Teller effect and hence, OO and CO are induced. The t_{2g} system also has strong electron-electron interaction, which is possibly also the source of OO.[69] The interplay of the charge and orbital ordering to minimize the lattice energy is possibly the origin of CO.[66] From *ab initio* density-functional calculations and exact diagonalization studies, Popovic and Satpathy[70] proposed that the dominant mechanism responsible for the charge order is the Jahn-Teller coupling, with a lesser but significant contribution from the on-site Coulomb interaction.

Another interaction need to be considered is the superexchange interaction between Mn sites. It was theoretically shown that superexchange promotes an antiferromagnetic state accompanied by orbital ordering in the insulating $LaMnO_3$. The superexchange interactions, which stabilize orbital order at low doping, are frustrated in the orbital liquid in which the material shows FMM state and orbitals are disordered.[71] Theoretical study on the combined influence of superexchange interaction and coupling to lattice degrees of freedom of strongly correlated e_g electrons in the ferromagnetic phase of $LaMnO_3$ indicates that the JT effect stabilizes the orbital ordering, and changes qualitatively the

spectrum of orbital excitations.[72] The orbital order-disorder transition is of the first order in a wide region of hole concentration, and the Néel temperature for the anisotropic spin ordering, such as the layer-type antiferromagnetic one, is lower than the orbital ordering temperature due to the anisotropy in the orbital space.[73] It was also found that Coulomb interaction disfavors the A-type charge and orbital order phase in energy, but favors the CE-type charge and orbital order phase.[74]

Orbital ordering exists in many CMR manganites and is coupled with spin, charge and lattice to affect the properties. In $LaMnO_3$, the $d_{3x^2-r^2}$ and $d_{3y^2-r^2}$ orbitals are alternately ordered (C-type OO) in the ab plane below ~780 K (Figure 1.15).[75]

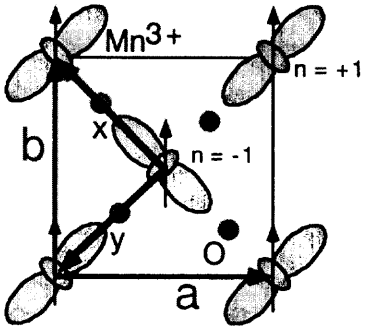

Figure 1.15 Schematic view of orbital and spin ordering in ab-plane of $LaMnO_3$.
Note: the orbital ordering along c-axis is expected to repeat the same pattern.[75]

In $Nd_{1-x}Sr_xMnO_3$ system, in doping range $0.25 \leq x \leq 0.48$, the compound is FMM and due to the DE effect, orbitals are disordered. For $x \sim 0.5$, the material has a CE-type AFM CO state, CO transition is accompanied by OO. In $0.52 \leq x \leq 0.62$, the material is A-type AFM, the ordering of $d_{x^2-y^2}$ orbitals induces the 2D-metallic in the ab-plane while along c-axis it is insulting.[63,76]

In $La_{1-x}Ca_xMnO_3$, near $x \sim 0.2$, it was reported that the insulator-to-metal transition is driven by the suppression of coherent Jahn-Teller distortions, originating from orbital ordering. The orbital ordered state is characterized by large long-range Q2 distortions of the MnO_6 octahedra below orbital ordering to orbital disordering transition temperature; above that, an orbital-ordered and orbital-disordered state coexist.[77]

By the x-ray scattering study, Zimmermann *et al.*[78,79] revealed that in $Pr_{1-x}Ca_xMnO_3$ (x = 0.25, 0.4, 0.5), the charge- and orbital-order scattering wave vectors are commensurate with the lattice. While long-range charge order is present, long-range orbital order is never established. Above the charge and orbital ordering temperature, charge-order fluctuations are more highly correlated than orbital fluctuations, suggesting that charge ordering drives orbital ordering in these samples.

High pressure was found to completely suppress JT effect and the concomitant orbital ordering above 18 GPa in $LaMnO_3$.[80]

Unlike other properties, an orbital represents a possible energy state of electrons in atoms. It cannot be observed directly by experiments. Only when occupied by an electron is it visualized as electron cloud. Therefore, OO can only be observed through the anisotropy of physical properties. Some experimental techniques have been developed to observe the orbital ordering state.

Through the induced anisotropy in the originally tetragonal MnO_2 lattice, OO can be probed in terms of optical birefringence effect. The principle of birefringence technique is: when sample is anisotropic and an optical axis of the sample is not parallel to the electric field of linearly polarized incident light, the reflected light is elliptically polarized and hence, has a component of the electric field perpendicular to the polarization of incident light. Two polarizers with polarizations perpendicular to each other can be used to detect the perpendicular component.[81] Figure 1.16 is the orbital ordering domain, long range OO induced by the substrate, in $Nd_{0.5}Sr_{0.5}MnO_3$ thin film, which is observed with polarizing optical microscopy.[82]

By measuring charge-density distribution, orbital ordering can also be revealed. By analyzing the synchrotron radiation x-ray powder diffraction data with maximum entropy method (MEM), Takata *et al.* [83] extracted the charge-density distribution of the antiferromagnetic bi-layered manganite, $NdSr_2Mn_2O_7$, which directly reveals the $d_{x^2-y^2}$-orbital polarization in the A-type antiferromagnetic state.

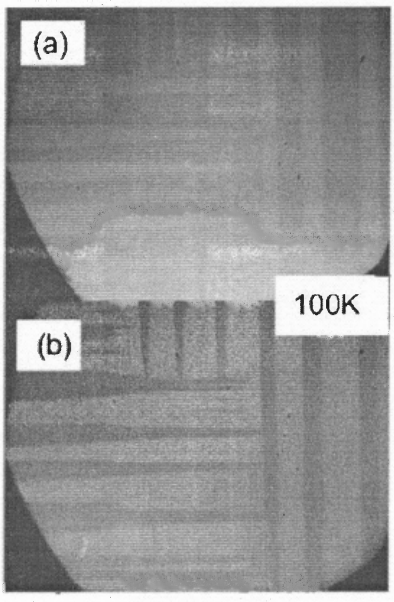

Figure 1.16 Orbital ordering domain in $Nd_{0.5}Sr_{0.5}MnO_3$ thin films.

Note: (a) and (b) differ in the orientation of the Fresnel rotator by 45°. A clear stripe pattern is observed. The film thickness is 300 nm.[82]

In CMR manganites, the Mn 4p states are empty and split by the interactions with e_g electrons in ordered orbitals.[84] The OO state induces an anisotropy of the atom scattering factor, which causes the scattering in the orbital superlattice reflection point to induce the nonzero resonant scattering intensity at reflections sensitive to the difference between orbitally ordered sublattices. Synchrotron radiation anomalous x-ray scattering can be used to detect OO state by studying the polarization dependence of scattering intensity.[75,84,85,86] With the resonant x-ray scattering techniques at Mn K-edge, the OO states in some manganites have been investigated, such as $LaMnO_3$,[75] $Nd_{1/2}Sr_{1/2}MnO_3$.[87]

Jiang *et al.*[88] suggested another method that uses energy-filtered quantitative convergent-beam electron diffraction (QCBED) to detect orbital ordering. Their calculations on structure factor of $LaMnO_3$ crystals indicates that several low-order electron structure factors show more pronounced change with orbital ordering, in which the e_g electron orders in the $d_{3z^2-r^2}$ orbital, leaving the $d_{x^2-y^2}$ unoccupied, than that of the x-ray structure factors.

1.2.4.5 Electron-Lattice Interaction. That DE theory cannot fully explain the CMR phenomenon indicates that electron-lattice interaction plays an important role. According to Millis,[89] there are two kinds of electron-lattice coupling: the tolerance factor which affects the electron hoping through the static crystal structure; the conventional dynamical electron-phonon coupling which represents the instantaneous deviations of atoms from its ideal positions and electron configuration. When electron-lattice coupling is relatively weak, it merely causes electron-phonon scattering. However, when it is strong, the charge carriers are localized, causing lattice to distort locally to produce a potential minimum. Then non-linear phenomena, such as polaron formation, take place. Polaron phenomenon is the most significant evidence of electron-lattice interaction that will be specifically discussed in next section.

The electron-lattice effects have been investigated both theoretically and experimentally. By considering electron-lattice interaction arising from Jahn-Teller splitting of the out Mn d level, Millis *et al.*[37] explained the large resistivity difference between prediction of DE theory and experimental results. Röder *et al.*[90] also found that accompanying the magnetic transition, there is also a continuous crossover of polaron state from large polaronic state to a quasi-self-trapped small polaron state in $La_{1-x}A_xMnO_3$ (A = Ca, Sr, Ba). The electron-lattice interaction was also shown by Ibarra *et al.*[91] experimentally: the magnetoelastic and magnetotransport properties are correlated in $La_{0.60}Y_{0.07}Ca_{0.33}MnO_3$, indicating the strong electron-lattice interaction [Figure 1.17(a)]. The electron-lattice interaction is suppressed in magnetic field [Figure 1.17 (b)].

In pseudocubic compounds, such as $La_{1-x}Ca_xMnO_3$, the strong coupling is partly due to JT effect, which breaks the local cubic symmetry and therefore the degeneracy of e_g levels. Another electron-lattice coupling is the breathing distortion of MnO_6 octahedra, in which all 6 Mn-O bonds become shorter/longer by the same amount. This raises (lowers) the energy of an unoccupied Mn site relative to an occupied one by energy E_B.

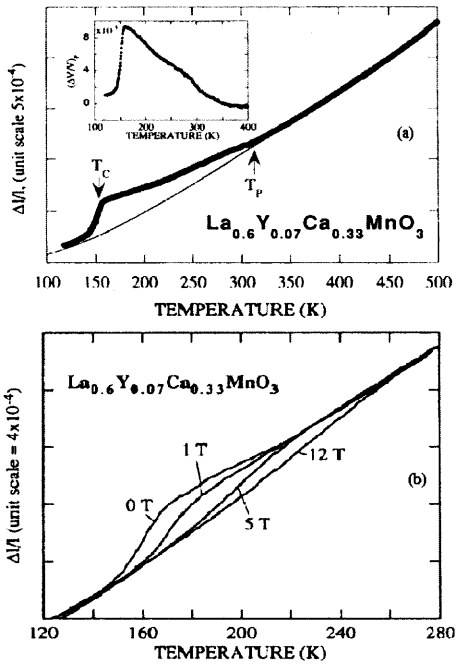

Figure 1.17 Linear thermal expansion of $La_{0.60}Y_{0.07}Ca_{0.33}MnO_3$.

Note: inset of (a) is anomalous thermal expansion contribution $(\Delta l/l)_P$, (b) is the linear thermal expansion in magnetic field.[91]

1.2.4.6 Polaron. Due to the strong electron-lattice interaction, polarons may form and play important role on CO state, transport and other properties. With strong electron-lattice interaction, local lattice structures deform and charge carriers are localized. The localized charge carriers have two states:[92]

One is the non-polaronic static state, in which the carriers are bound in large radius states associated with modest displacements of equilibrium atom positions;

The other is the small polaronic state, which exists in severely localized states with significant displacements of the atomic equilibrium positions. This inseparable combination of electron and lattice polarization/distortion is called a small polaron, in which the lattice distortion induces a potential well so that the electron is "self-trapped".

The size of small polaron is comparable to unit cell.[93] If the self-trapped carriers and the crystal deformation involve more than a single site, the cluster is considered a large polaron.

The small or large polaron formation depends on which electron-lattice interaction is important. Large polarons are formed when the long-range components of the electron-lattice interaction, the long-range Coulombic interactions between an electronic carrier and an ion, predominate. Small polarons form when the short-range components of the electron-lattice interaction, such as the deformation-potential interaction, predominate.[94]

For large polaron, the lattice polarization is small and electron moves in a band with slightly enhanced mass. For small polaron, lattice polarization is much greater, and electron is trapped to a single lattice site in most time.

The electronic transport properties of large and small polarons are qualitatively different: large polarons move with significant mobilities, $\mu > 1 cm^2/V.s$, falling with increasing temperature; small polarons move with very low mobilities, $\mu << 1\ cm^2/V.s$, increasing with increasing temperature.[92]

In manganites and other magnetic systems, there are different kinds polarons: dielectric small polaron, JT polaron and magnetic polaron. Dielectric small polaron is that electron bears with it a dilation of MnO_6 octahedra; for JT polaron, electron carries with it an axial distortion of MnO_6 octahedron; for magnetic polaron, the surrounding Mn core spins are ferromagnetically polarized.[18] Figure 1.18 shows the sketch of these polarons.

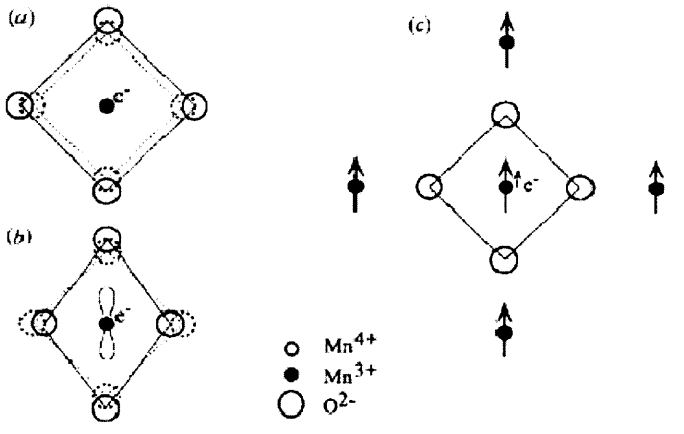

Figure 1.18 Schematic pictures of various polarons.

Note: (a) small dielectric polaron; (b) Jahn-Teller polaron; (c) magnetic (spin) polaron.[18]

The magnetic polarons are magnetically ordered clusters due to exchange between bound carriers and localized spins. Röder *et al.*'s[90] theoretical calculations indicate that magnetic polaron comprises a localized charge surround by a spin cloud on the nearest neighbors. The size of it is approximately several lattice sites (Figure 1.19). In the paramagnetic insulating phase of manganites, electron is bound as a magnetic polaron. It moves only by hopping from occupied to unoccupied sites so that the materials show an insulating behavior. When magnetic fields applied, the host spin is aligned and the electron becomes free to move diffusively through the lattice.[18] Consequently, the polaron mobility is drastically enhanced.[95,96]

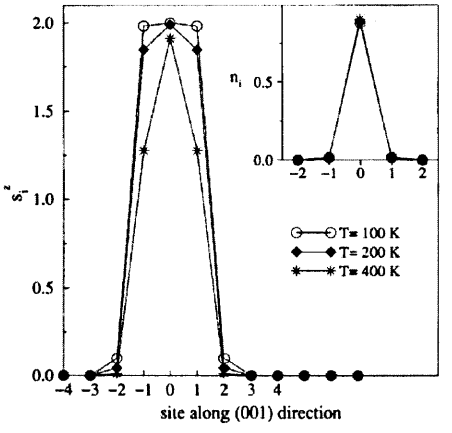

Figure 1.19 Magnetization and charge distribution of self-trapped magnetic polaron.
Note: the inset is the charge distribution; the lines are guides to the eye.[90]

The existence of polaron and its coupling with magnetic and electronic properties in manganites have been investigated extensively. Zhou *et al.*[97] found that there is a polaronic state that can be suppressed by pressure in temperature range of $T_{CO} < T < T_C$ in $La_{0.85}Sr_{0.15}MnO_3$. Billinge *et al.*[98] observed small lattice polarons in $La_{1-x}Ca_xMnO_3$ (x = 0.12, 0.21, and 0.25) with neutron pair distribution function analysis. The polaronic distortion of lattice is modeled as a uniform collapse of MnO_6 octahedron associated with the Mn^{4+} site.

The polaron formation is closely associated with the metal-insulator transition and

charge carrier transport. For x = 0.3 compounds, Tyson *et al.*'s[99] EXAFS results indicate that local structure change is significantly correlated to small polaron formation at $T > T_C$, displaying that in manganites with metal-insulator transition and magnetization increasing small polarons are delocalized.

Some other experiments indicated that polarons have a magnetic character.[91,100,101] Teresa *et al.*[102] showed that polaron in single crystalline $La_{0.7}Ca_{0.3}MnO_{3-\delta}$ thin films has Jahn-Teller-type nature and the polaron binding energy plays key role in determining the transport and magnetic properties.

Localization is the result of competition between kinetic energy and interaction. In double exchange systems, it may be affected by magnetic order. While spin order changing with temperature, a large-small polaron transition may occur.[90,103,104] It is well established that carriers form polarons in paramagnetic insulating phase. However, many evidences also show that polarons survive below T_C in the FMM phase. In the FMM to PMI transition, polarons in fact crossover from a state in which large polaron dominates to that small polaron dominates.[105,106]

Polaron formation is correlated to lattice structure, which can be modified by the average A-site atom size $\langle r_A \rangle$. The ionic size effect on polaron stability can be explained as: with $\langle r_A \rangle$ reduced, electron bandwidth is decreased because of the bending of Mn-O-Mn bond, leading to the formation of polarons. With small $\langle r_A \rangle$, polaron is much stable, and the system is an antiferromagnetic or ferromagnetic insulator. It is found that while $\langle r_A \rangle$ is below 1.34 Å, the system is FMI, if greater than 1.386 Å, the polarons will not form and the material is a homogeneous regular metal. In the crossover range of $1.34 < \langle r_A \rangle < 1.386$ Å, polarons are marginally stable and are influenced easily by external factors, such as magnetic field, producing the CMR phenomena (Figure 1.20).

Local Jahn-Teller distortion increases Mn-O bonds, which is accommodated by the Mn-O-Mn bond buckling. JT polaron is always stable. Thus the system is always insulating for $x > 0.5$. In this case, polarons order to form polaron lattice, or charge

ordering when doping levels are rational number. So the smaller $<r_A>$ is, the more stable the polaron is. This has been proved by the robustness of CO state in the small $<r_A>$ systems, such as $Pa_{1-x}Ca_xMnO_3$ and $Sm_{1-x}Ca_xMnO_3$ (Figure 1.14).

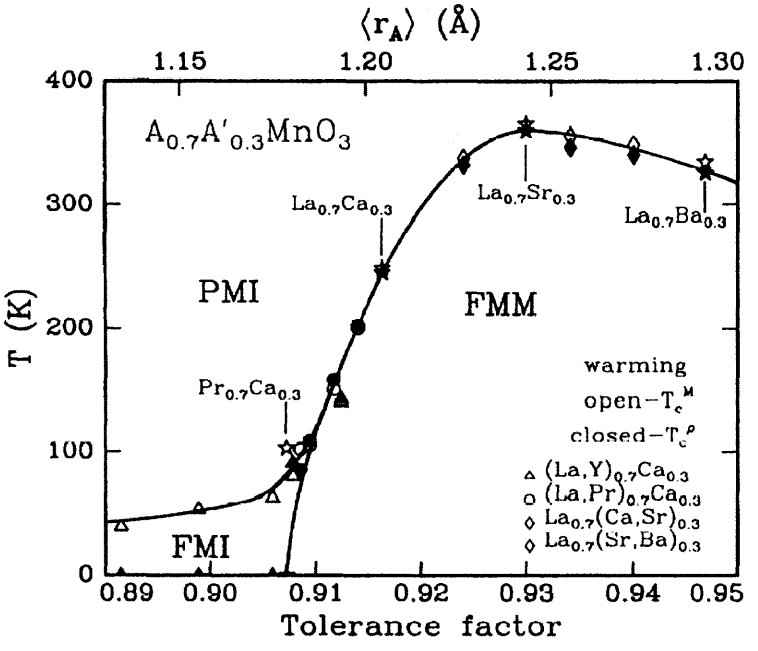

Figure 1.20 Phase diagram of temperature *vs.* tolerance factor for $A_{0.7}A'_{0.3}MnO_3$.

Note: A is a trivalent rare earth ion and A' is a divalent alkali earth ion. Open symbols denote T_C^M measured at 100 Oe. Solid symbols denote T_C^ρ data taken while warming. The tolerance factor and $<r_A>$ are calculated with the A-site ions in the 9-coordianation case.[27]

1.3 Structure and Distortions

The ideal perovskite structure ABO_3 is cubic. Because of the size mismatch of A-site and B-site atoms, the ideal structure is orthorhombically distorted. The orthorhombic distortion is related to the average A-site radii. The distortion degree is characterized by tolerance factor t, defined as:

$$t = \frac{r_A + r_O}{\sqrt{2}(r_B + r_O)} \tag{1.8}$$

where r_A, r_B and r_O are the radii of the A, B and oxygen ion size respectively. The

tolerance factor t can be calculated with the published ion radii (In Table 1.3 lists the mostly used data in manganites). When t is not unity, atoms are displaced from the ideal cubic position and various distortions are induced. The crystal symmetry is lowered. The structure is distorted through the rotation of BO_6 octahedra, leading the oxygen atoms displaced.

Table 1.3 Radii of Several Trivalent and Divalent Ions Used in Manganites

La^{3+}	1.36	Sm^{3+}	1.24	Mn^{4+}	1.53	Ca^{2+}	1.34
Y^{3+}	1.19	Bi^{3+}	0.96	Ba^{2+}	1.61	Cd^{2+}	1.31
Pr^{3+}	1.29	Gd^{3+}	1.22	Pb^{2+}	1.49	Sn^{2+}	1.30
Nd^{3+}	1.27	Mn^{3+}	0.645	Sr^{2+}	1.44		

Note: the unit is Å. Radii are the case of 12-coordinates. Data are from ref. 107.

If t is only slightly deviated from unity, there may be only a small distortion to rhombohedral structure with symmetry $R\bar{3}c$, due to the octahedra rotation about the [111] axis. In rhombohedral structure the six B-O bonds are identical.

When t is small, the cooperative rotation of BO_6 octahedra about [110] axis leads to the O-type orthorhombic $GdFeO_3$ structure, in which $a < c/\sqrt{2}$. In $LaMnO_3$, $a > c/\sqrt{2}$, which is designated as O'-type orthorhombic. Some manganites may have another kind of orthorhombic structure, in which we have $a \approx b < c/\sqrt{2}$, designated as $O^{\ddagger}$. Besides these kinds of distorted structure, the dynamic JTD leads to a quasi-cubic structure: O*-orthorhombic structure, in which $a \approx c/\sqrt{2}$.

In manganites of different doping system and concentration, in addition to symmetry lowering, the local atomic structure is distorted both statically and dynamically.

For the static local structure, there are two characteristic local distortions:

One is the cooperative tilting of MnO_6 octahedra. Because of the small A-site ions, the octahedra rotate along c-axis, leading to the Mn-O1-Mn bond angle decreasing from

180° (Figure 1.4). This induces the bandwidth decrease.

The other is the distortion of MnO_6 octahedra due to Jahn-Teller effect. The Jahn-Teller effect is important to the electronic properties of materials. In 1936, Jahn and Teller[108] first stated that: stability and degeneracy cannot simultaneously exist unless the molecule is linear. All orbitally degenerate electronic states of non-linear molecules are unstable whether the degeneracy is due to electronic orbital or to spin, except the twofold spin degeneracy in molecules containing an odd number of electrons (Kramer's doublet). These states may be stabilized by spontaneous distortion of the interstice to lower symmetry that removes the ground-state degeneracy and lower energy.

In manganites, the octahedral crystal field splits the degenerate 3d orbital of the Mn^{3+} to two subgroups: t_{2g} and e_g. The t_{2g} orbitals lie below the e_g orbitals because the orientations of the three t_{2g} orbitals are directed between bond axes while the two e_g orbitals point along bond axis. The t_{2g} and e_g orbitals are 3-fold and 2-fold degenerate, respectively. The Jahn-Teller theorem indicates that distortions occur for any degenerate state. Therefore, the degeneracy of both t_{2g} and e_g orbitals splits through the distortions of MnO_6 octahedra. The degeneracy removal induces the electronic structure in Figure 1.5.

As indicated by Goodenough,[109] distortions to lower crystalline symmetry require cooperative distortions of the JT ions. Spontaneous electron ordering to render a low temperature structure of low symmetry only occurs when the concentration of JT cations is greater than some critical fraction. Since they are cooperative phenomena, they may exhibit thermal hysteresis. JT effect is only due to lattice-orbital interactions. It is independent of spin, and therefore, of spin ordering at Curie or Néel temperature.

With Jahn-Teller distortion, the three identical Mn-O bonds are split to long and short Mn-O bonds. The Jahn-Teller distortion of MnO_6 octahedra can be described by the combination of two vibronic modes Q2 and Q3 (the Q1 mode is the so-called breathing mode that the six Mn-O bonds simultaneously elongate or contract). The ab-plane distortion mode Q2 and the c-axis elongation mode Q3 are shown in Figure 1.21. The

static JTD can be coherent or not, depending on the A-site ion size and doping level. When $<r_A>$ or the tolerance factor is small, the JTD is long range ordered, such as in $LaMnO_3$. But with some trivalent A-site atoms are replaced by divalent atoms, the number of JT active ions is reduced so that the long range order of JTD is suppressed, which induces the metal-insulator transition at $x \sim 0.3$.

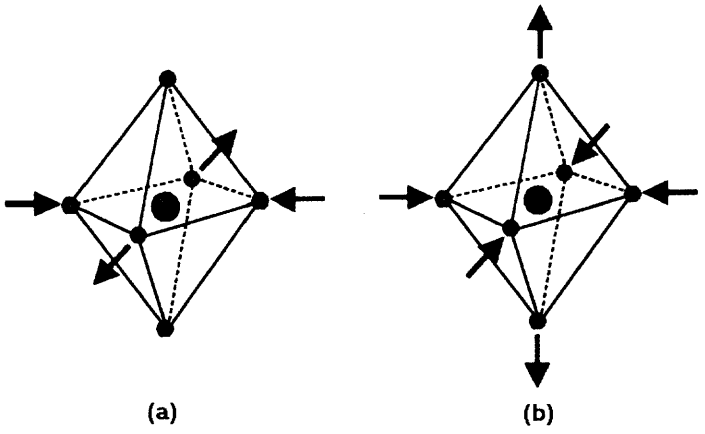

Figure 1.21 Jahn-Teller distortion of BO_6 octahedron.

Note: (a) Q2 mode, in which two of the in-plane Mn-O bonds elongate while the other two contract; (b) Q3 mode, in which the four in-plane Mn-O bonds contract and the two apical Mn-O bonds elongate.

Jahn-Teller distortions are critically important in the orbital, spin and charge states in manganites. In the manganite system $LaMn_{1-x}Cr_xO_3$ ($x \leq 0.5$), upon Cr-doping, because of JT active cation decreasing, Jahn-Teller distortion is reduced, yielding less distorted orthorhombic structures.[110] Jahn-Teller coupling is the dominant mechanism of charge ordering.[70] In CO phase, the cooperative JTD are crucial for the formation of orbital structure. Together with charge superstructure, JTD induces and stabilizes magnetic structure in insulating phase.[111,112] The interference of totally symmetry and the cooperative Jahn-Teller distortions can induce stripe phase formation in manganite compounds.[113]

The Jahn-Teller distortion states may change with temperature, pressure and other parameters, such as in $La_{0.52}Y_{0.15}Ca_{0.33}MnO_3$ ($T_{IM} \sim 115$ K), accompanying the insulator-

to-metal transition, Jahn-Teller distortion of MnO_6 octahedra is remarkably decreased, in which the basal-plane collective distortion mode Q2, responsible for the gap opening, reduces, giving more perfect octahedra with MnO_4 equatorial square planes.[114]

In addition to the static structure distortion, dynamic distortion is important as suggested by Millis[37,89] and Röder.[90] One of the dynamic effects is the dynamic Jahn-Teller effect in which the octahedra spontaneously change its form. The other one is the "breathing" mode distortion of the MnO_6 octahedra. These dynamic distortions induce strong electron-phonon coupling and is an important factor affecting the charge transport.

Considering structure and various physics in the perovskite manganites, we can say that the question of CMR physics is that of the distortions and their stability with changes in $<r_A>$, temperature, pressure, magnetic field, etc. For example, due to the lattice distortion, charges and orbitals can be ordered. In $Nd_{1/2}Sr_{1/2}MnO_3$, with temperature increasing, while the CO state collapses into FMM state, the structure also undergoes transition from higher orthorhombic distortion to low distortion state [Figure 1.9(b)]. By adjusting $<r_A>$, both static and dynamic distortion, even the structure symmetry, can be tuned in a large range. Radaelli *et al.*[115] investigated the correlation of $<r_A>$ and static coherent distortion of MnO_6 octahedra with doping systems $A_{0.7}B_{0.3}MnO_3$ (Figure 1.22) and the static coherent and incoherent distortion as a function of temperature of $La_{0.75}Ca_{0.25}MnO_3$ (Figure 1.23). At both low and high temperature, with $<r_A>$ decreasing, the system experiences rhombohedral to orthorhombic transition. In orthorhombic phase, with $<r_A>$ decrease, the local structure is more distorted. In $La_{0.75}Ca_{0.25}MnO_3$, with temperature increasing, during the FM to PM magnetic transition, both the coherent and incoherent distortion increases.

The local structure can even be changed by photons. In $La_{0.875}Sr_{0.128}MnO_3$, at low temperature, the CO state can be destroyed by x-ray irradiation, indicating a structure changing.[116] Hydrostatic pressure is another way to affect the structure, which will be discussed in chapter 2.

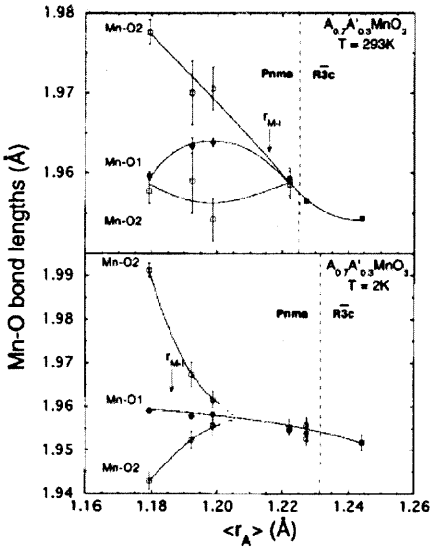

Figure 1.22 Static coherent distortion of MnO_6 octahedra as a function of $<r_A>$.

Note: for $A_{0.7}B_{0.3}MnO_3$ at 293 K and 2 K. The dashed lines separate the different structure phases.[115]

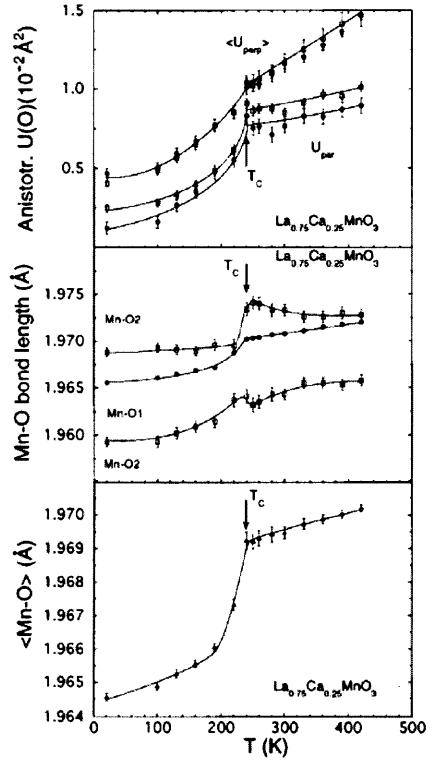

Figure 1.23 Coherent and incoherent distortions of MnO_6 octahedra *vs.* temperature.

Note: the sample is $La_{0.75}Ca_{0.25}MnO_3$. Average Mn-O bond length (lower panel), individual Mn-O bond lengths (center panel) and projections of the oxygen anisotropic Debye-Waller factors parallel (U_{par}) and perpendicular ($<U_{perp}>$) to the direction of Mn-O bond lengths for O1 (filled circles) and O2 (open squares) (upper panel).[115]

1.4 Electron Transport in CMR

Because of various complicated couplings, the electron transport of manganites shows interesting features, such as paramagnetic insulating, antiferromagnetic insulating, ferromagnetic metallic, etc. Different electron transport behaviors have been reported, e.g. polaronic, magnetic localization. Correspondingly, various mechanisms are also proposed. However, the resistivity is sensitive to grain size, grain boundary angles, pressure[117,118] and substrate and preparation conditions for thin films which may distort the lattice.[119,120] This leads it more difficult to understand the transport behavior in addition to other properties.

1.4.1 Double Exchange Transport

The earliest endeavor to understand the coupled ferromagnetic and metallic electronic transport behavior in manganites is Zener's DE theory. According to DE theory, Zener predicted the conductivity to be:[34]

$$\sigma \approx \frac{xe^2}{ah}\frac{T_C}{T} \tag{1.9}$$

where x is the Mn^{4+} concentration (doping level), e is the electron charge, a is the lattice parameter, h is the Planck constant, T_C is Curie temperature and T is temperature.

When the material is in ferromagnetic state, the conduction electrons hop between Mn^{3+} and Mn^{4+} sites without changing spin state. For AFM phases, because the Zener bandwidth is zero, the material is insulating. At Néel temperature, resistivity does not change greatly and the activated insulating behavior persists through the transition to AFM state. This qualitatively explained the coupled ferromagnetic and metallic behavior. Figure 1.24 is the resistivity calculated with DE model by Millis.[37] However, the resistivity is much smaller than that observed in experiments as indicated by Millis and other factors, such as electron-phonon coupling due to Jahn-Teller effect, should be considered.

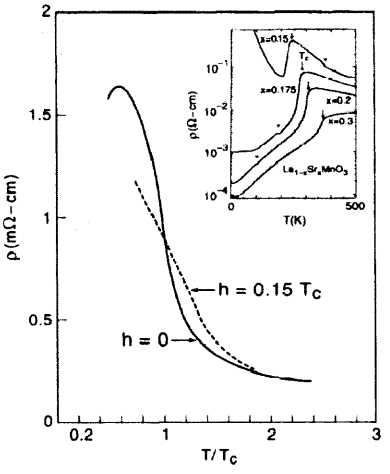

Figure 1.24 Resistivity calculated with double-exchange model.

Note: the solid line is the resistivity in zero field; the dashed line is the resistivity in a field of $0.15T_C$, corresponding to 200 T magnetic field. The inset displays data from Tokura *et al.*[37]

1.4.2 Transport in Low Temperature Ferromagnetic Metallic Phase

With more experiment results appearing, some empirical models were suggested. In the low temperature ferromagnetic metallic state, some authors[30,121,122,123] reported that the resistivity behavior is $\rho(T) = \rho(0) + AT^2$. But they suggested different mechanisms.

Urushibara *et al.*[30] suggested that the T^2 dependence and the reduction of A implies the important role of electron-electron scattering and reflects the strong electron correlation in the manganite system. Jaime *et al.*[122] attributed the dominant T^2 temperature dependence above 50 K in the single crystal $La_{2/3}(Pb, Ca)_{1/3}MnO_3$ to single magnon scattering but not the electron-electron mechanism. Okuda *et al.*'s[123] resistivity and specific heat results of $La_{1-x}Sr_xMnO_3$ indicate that the significant increase of the residual value, T^2 coefficient of resistivity as well as of T^3 term of specific heat with decrease of x results from the dynamically but collectively orbital-ordered or Jahn-Teller distorted background.

The low temperature behavior is also reported to be $T^{2.5}$. Schiffer *et al.*[28] fit the resistivity of $La_{1-x}Ca_xMnO_3$ (x = 0.20, 0.33, 0.45) at $T < 0.5T_C$ range with an empirical formula: $\rho(T) = \rho_0 + \rho_1 T^{2.5}$. In this expression, ρ_0 is the resistivity due to domain

boundaries and other temperature-independent scattering mechanisms; $\rho_1 T^{2.5}$ term is an empirical fit which represents a combination of electron-electron, electron-phonon, and electron-magnon scattering, all of which are expected to be significant in this system. Teresa *et al.*[100] reported that the low temperature resistivity of $La_{2/3}Ca_{1/3}MnO_3$ in magnetic field (up to 12 T) and under pressure (up to 7.7 kbar) still maintain the behavior. Magnetic field and pressure have different effects on the temperature-independent scattering term ρ_0 (due to domain and grain boundaries, defects etc.) and the temperature-dependent term $\rho_1 T^{2.5}$ (due to the electron, electron-phonon and electron-magnon scattering). A field of 1 T strongly affects the temperature-independent term ρ_0, whereas it has less influence on the temperature-dependent term $\rho_1 T^{2.5}$. It is likely that low magnetic fields increase the size of the magnetic domains so that the scattering of the electrons due to domain boundaries decreases and the magnetization becomes larger. Magnetic fields >1 T seem to affect both mechanisms in similar degree. Pressure affects ρ_1 more than ρ_0 by decreasing the temperature-dependent mechanisms of scattering: electron-electron, electron-magnon, and electron-phonon scattering. As sample being polycrystalline, pressure is supposed to affect the connections between the grains just mechanically. The size of the magnetic domains can also be increased with pressure.

1.4.3 Transport in High Temperature Paramagnetic Phase

Different models for the mechanism in high temperature paramagnetic insulating phase have been developed. In general, these modes fit into two categories: polaron hoping and variable range hoping. Small grain polycrystalline samples, very thin and unannealed films, were reported to show variable range hoping type localization while high quality epitaxial films and crystals were reported to be polaron hoping type. Ziese *et al.*[95] found that the resistivity of high-quality epitaxial manganite thin films shows small polaron behavior; whereas the resistivity in polycrystalline films follows a variable range hopping

manor. The small activation energies imply polaron hopping. The polaron mobility can be drastically enhanced by the ferromagnetic ordering. Coey *et al.*'s[124] polycrystalline samples show the VRH behavior. Localization phenomena are thought to be important since the conduction band is relatively narrow with a bandwidth about 1 eV. In Coey *et al.*'s[124] model of carrier localization by random fluctuations in Hund's-rule coupling, localization might lead to the formation of a mobility edge or to variable-range hopping between the localized states.

It is regarded that when temperature is high enough, magnetic correlation can be neglected because of the very strong charge-lattice and charge-charge interactions.[125] In this case, the system can be considered small polaronic.

1.4.3.1 Polaron Model. Because of strong electron-lattice interaction, different kinds of polaron, such as small polaron, Jahn-Teller type polaron, magnetic polaron and large polaron are suggested to exist in paramagnetic phase in manganites. Lattice polaron formation and local structure distortion have important implications on electron transport. The transport of the polarons above T_C displays an insulating behavior.

Park *et al.*'s[126] photoemission, XAS results on $La_{1-x}Ca_xMnO_3$ and $La_{1-x}Pb_xMnO_3$ suggest that strong small polaron effects, which contribute to a charge fluctuation energy of ~1.5 eV, are responsible for the insulating behavior above T_C.

The influence of magnetic field on resistivity above T_C indicates that polarons have magnetic character. Helmolt *et al.*[4] suggested that the transport mechanism in $La_{2/3}Ba_{1/3}MnO_3$ thin films is magnetic polaron hoping. Teresa *et al.*'s[100] results of $La_{2/3}Ca_{1/3}MnO_3$ also support the magnetic polaron formation above T_C. Above T_C, the transfer integral is increased by magnetic field and pressure, and hence, charge localization is reduced so that the FMM state is favored.

Based on observation to $La_{0.7}Ca_{0.3}MnO_3$ thin films, Hundley *et al.*[127] described the correlation between resistivity and magnetization M below T_C with a phenomenological expression:

$$\rho(H,T) = \rho_m \exp\left(\frac{-M(H,T)}{M_0}\right) \tag{1.10}$$

where ρ_m and M_0 are fitting parameters. For temperatures above T_C where FM fluctuations are not observed (at T > 280 K, the film is purely paramagnetic, i.e., M ∝ H) ρ and *M* are no longer related by the equation. They suggested that polaronic hopping is the prevalent conduction mechanism below T_C and that the nature of polaron be both H and T dependent. The characteristic polaron size could evolve from ''small'' at high-T/low-H to ''large'' at low-T/high-H. Small polarons are highly localized while large polarons are delocalized and can have resistivity comparable to poor metals ~100 μΩ.cm.

Lee and Min[128] incorporated the strong electron-phonon interaction to double-exchange model. They investigated transport and magnetic properties of the manganese oxides $R_{1-x}A_xMnO_3$. They found that the semiconducting behavior above T_C is attributed to the effect of self-trapped lattice small polarons transporting by tunneling. The rapid falloff of resistivity below T_C is attributed to the combined effects of coherent lattice polaron hoping and increased bandwidth.

Palstra *et al.*[129] think that above the metal-insulator transition, the transport mechanism is not dominated by spin disorder, but by small polaron formation that involves the MnO_6 octahedra distortion. Synder *et al.*[121] indicated that high temperature resistivity of $La_{0.67}Ca_{0.33}MnO_3$ clearly follows the small polaron hopping manor both in thermally activated regime and at higher temperature where scattering becomes important. Teresa *et al.*[102] showed that polaron in single crystalline $La_{0.7}Ca_{0.3}MnO_{3-\delta}$ thin films is Jahn-Teller-type. The polaron binding energy plays key role in determining the transport and magnetic properties of these manganites. The conducting mechanism above T_C follows the Holstein's small polaron hoping model:

$$\rho = AT\exp(\frac{E_{hop}}{k_B T}) \tag{1.11}$$

where E_{hop} is the polaron hopping energy. E_{hop} can be expressed as $E_{hop} = W_H + \varepsilon_0$,[93]

where ε_0 is the activation energy necessary to produce a stationary number of carriers, the number of carriers in equilibrium, which can be obtained from the temperature dependence of thermopower.

Jakob *et al.*'s[130] study on resistivity of $La_{0.67}Ca_{0.33}MnO_3$ films suggests that the resistivity is non-adiabatic small polaronic and has magnetic character. They developed a phenomenological model to describe the temperature and magnetic field dependence of resistivity:

$$\rho(T,B) = \rho_0 T^{\alpha} \exp\left(\frac{E_A^0}{k_B T}[1 - B_J(N_I)B_J(N_P)\right) \tag{1.12}$$

where α = 1 and 1.5 are the adiabatic and non-adiabatic limit respectively, $B_J(N_I)$ and $B_J(N_P)$ are the Brillouin functions; N_I is the unclustered ion number, N_P is the clustered ion number. It is found that polarons have a magnetic contribution to the activation energy. It depends on the variation of spin order with increasing temperature and can be modified by magnetic field. The average magnetic clusters (magnetic polaron) contain 4–6 ions, i.e., only nearest neighbors are spin polarized.

Jaime *et al.*[93] indicated that the field dependence of the characteristic energies and relatively small mass of polarons in $La_{1/3}Ca_{1/2}MnO_3$ thin films suggest that they have both lattice and magnetic character. In polaronic state, because of some energetically equivalent crystal lattice site, a narrow energy band of localized states forms. At different temperatures, the conducting mechanism is different. At very low temperatures of $k_BT \leq$ 0.1 meV, the only possible mechanism is quantum tunneling between neighboring distortions; in range of $T < \theta_D/2$, where θ_D is the Debye temperature, phonon-assisted hopping dominates, resulting a conductivity $\ln(\sigma) \propto -T^{-1/4}$, which is not associated with variable range hopping; in high temperatures range the thermally activated hopping of carriers dominates, the activated mobility can be described as:

$$\mu_P = \frac{x(x-1)ea^2}{\hbar}\left(\frac{T_0}{T}\right)^S \exp\left(-\frac{W_H - J^{3-2S}}{k_B T}\right) \tag{1.13}$$

where a is the hopping distance, J the transfer integral, x the polaron concentration, and W_H one-half of the polaron formation energy E_p. In nonadiabatic limit, s = 3/2 and $k_BT_0 = (\pi J^4/4W_H)^{1/3}$; in adiabatic limit, s = 1 and $k_BT_0 = \hbar\omega_0$, where ω_0 is the optical phonon frequency. In manganites, the optical phonon energy is similar to k_BT_0, so it can be considered adiabatic. The conductivity is expressed as

$$\sigma = \frac{x(x-1)e}{\hbar a}\frac{T_0}{T}\exp\left(-\frac{\varepsilon_0 + W_H - J}{k_BT}\right) = \sigma_0\frac{T_0}{T}\exp\left(-\frac{E_\sigma}{k_BT}\right) \tag{1.14}$$

1.4.3.2 VRH Model. Another view about the electron transport mechanism of manganites in high temperature paramagnetic phase is the variable range hoping. Localization might lead to a mobility edge or variable-range hopping between localized states. If the carriers are localized by random potential fluctuations, the resistivity can be expressed by Mott's VRH model:

$$\rho = \rho_\infty \exp\left[\left(\frac{T_0}{T}\right)^{1/4}\right] \tag{1.15}$$

the temperature scale T_0 is related to the localization length ξ by

$$kT_0 = \frac{24}{\pi N(E_F)\xi^3} \tag{1.16}$$

where $N(E_F)$ is the density of states at Fermi level.

In mixed valence manganites, the random distribution of A^{3+} and A^{2+} ions in lattice can induce magnetic disorder above T_C and fluctuation of Coulomb potential. This leads to a mobility edge.[131] At high temperatures, carriers are excited from Fermi level E_F to the mobility edge E_μ, leading to the activated behavior; at low temperatures, because the phonon energy is low, it is possible for carriers to hop with a low activation energy in the manor $\ln(\rho) \propto T^{-1/4}$. Sheng *et al.*[132] showed that the magnetotransport phenomena in Mn oxides can be understood systematically by considering the electronic localization effect due to DE spin disorder and nonmagnetic randomness, including local potential fluctuation induced by substitution of R^{3+} with A^{2+} and the lattice distortion around R^{3+}

and A^{2+} due to the ionic size mismatch. To acquire largest MR, there is an optimum nonmagnetic disorder, which can be tuned so that the metal-insulator transition being close to T_C.

Varma[133] suggested that Jahn-Teller effects are not very important. By considering carrier localization due to the slow magnetic disordering and electron-electron interactions, he concluded that the primary effect of magnetic field on transport is to alter the localization length. Localized carrier tends to form a spin polaron whose motion is governed by the slow spin fluctuations. External magnetic field decreases the magnetic disordering and hence, increases localization length and thereby decreases the resistivity. The conductivity takes the variable range hoping form:

$$\sigma \sim \exp\left(-\left(\frac{T_0}{T}\right)^{1/2}\right) \tag{1.17}$$

where $T_0 \approx \frac{e^2}{\kappa\xi}$ for $T << T_0$, ξ is the localization length for states near the chemical potential. As the effect disorder is decreased by magnetic field, ξ increases, leading resistivity to decrease. In the PM regime, $\xi(H) = \xi_0[1+\chi(T)H^2/\bar{t}]$, where ξ_0 depends the electron density, $\bar{t}$ is O(t) and t is the transfer integral.

For the x ~ 0.3 manganites, Viret *et al.*[134,135] and Coey *et al.*[124] developed the model of carrier localization induced by magnetic disorder to explain the transport properties in the whole temperature range and in magnetic field. The metal-insulator transition is ascribed to a modification of the spin-dependent exchange potential $J_H s \cdot S$ associated with the onset of magnetic order at T_C. Here J_H is the on-site Hund's rule exchange coupling of an e_g electron (s = 1/2) to the t_{2g} ion core (S = 3/2). Above T_C, the e_g electrons are localized by the random spin-dependent potential. The conduction is by VRH. When a magnetic field is applied or when there is an internal molecular field, the random distribution of spin directions is narrowed, and the average magnetic potential decreases. Over the whole temperature range, the resistivity is expected to varies as:

$$\ln(\frac{\rho}{\rho_\infty}) = \left(\frac{T_0}{T} \left(1 - \left(\frac{M}{M_S} \right)^2 \right) \right)^{1/4} \tag{1.18}$$

where there is:

$$k_B T_0 = f \frac{\alpha^3}{N(E_F)} \tag{1.19}$$

α is the inverse localization length which characterizes the spatial extension of the localized states, $N(E_F)$ is the density of states at Fermi energy (9×10^{26}/eV.m^3), f is a prefactor which varies in different derivations.

1.4.3.3 Between Polaron and VRH. Despite the difference in polaron model and VRH model, the gap between them may be reconcilable.

The polaron models neglect carrier localization by random charge fluctuations or random fluctuations in magnetic potential due to the doping atoms while the VRH model does not consider the existence of polarons. It was reported that the VRH of small polarons can also leads to $\ln(\rho) \propto T^{-1/4}$ behavior.[136] In $(La, Y)_{0.67}Ca_{0.33}MnO_3$ system, it was reported that nano magnetic clusters of a few to several tens of Mn ions exist above T_C.[137]

By considering the magnetic characteristic of polarons and the magnetic disordering and the Coulomb potential disordering induced by the divalent elements doping in the manganites, this picture seems reasonable:

The magnetic clusters are large scale and disordered. Polarons exist in the clusters and can hop inside them. On the boundary of clusters, polarons hoping between these clusters show a VRH behavior. Inside the cluster because of the FM coupling, it only shows a polaron behavior. An external magnetic field reduces the disorder of clusters and induces a larger mean free path for the polaron hoping. Certainly, magnetic field can also reduce spin disordering due to the tilting of the MnO_6 octahedra inside the cluster. If the local distortion is reduced, such as by hydrostatic pressure and larger divalent atom doping, both the moment of the cluster and the size (the hoping distance) can be increased. This will lead to a lower resistivity.

CHAPTER 2

CMR MATERIALS UNDER HIGH PRESSURE

2.1 Introduction

Pressure is one of the most important thermodynamic variables. However, although with the same importance as temperature and other variables, pressure had not play a role in probing condensed matter due to the technical difficulty to acquire high enough pressure to induce detectable changes in condensed state. With the developments of high pressure techniques, especially the diamond anvil cell (DAC) techniques, condensed matter physics has been broadly extended.

Generally, pressure affects the properties through driving atoms closer to each other. In this way, the electronic structure of atoms may become much different from that at ambient pressure to induce brand new electronic and magnetic bulk properties, such as insulator to metal transition, even transitions to superconductor.

For solid state matter, pressure can make atoms more compact and may induce structure changes to either ordered or disordered states. The local atomic structure, such as the atom distances (the chemical bond) and the bond angles, and the crystal structure can be changed in a continuously tunable way. Not only the static structure, but also the dynamic effects, such as the electron-phonon interaction, can be modified as well.

In high pressure related fields, the superconductivity search is one of the most noticeable examples. Pressure has been being used to look for superconductive properties of various single elements, such as S, Nb, Se, and Te.[138] Silicon, a semiconductor with diamond structure at ambient pressure, is a typical. Under high pressure, it transforms in the order β-Sn to Sh to SiVi to hcp structure at pressures of 11.5, 14, 30 and 40 GPa respectively.[139] Except the low pressure phase, all others are superconductive. The Superconductivity in the simple hexagonal phase of silicon was predicted by electron-

phonon-coupling calculation and was measured experimentally (Figure 2.1).[140]

In searching for high temperature superconductivity, pressure also played a prominent role. It was reported that in the mercury-bearing cuprates $HgBa_2Ca_2Cu_3O_{8+\delta}$, with the application of pressure, T_C increases from the ambient 135 K to 164 K at 30 GPa, the highest T_C reported at present.[141]

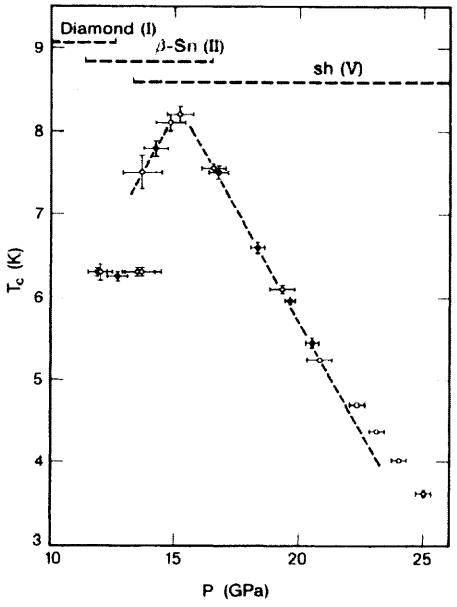

Figure 2.1 Pressure dependence of superconducting transition and structure of Si.[140]

2.2 High Pressure Effects

In manganites, there are complicated interactions among spin, charge, orbital and lattice degrees of freedom. This leads to subtle balance between different electronic and magnetic states. The balance can be easily broken down by other factors, such as chemical doping, magnetic field, electromagnetism wave etc., to lead to different electronic and/or magnetic phases. Compared with chemical, pressure is a "clean" method to affect the CMR properties through structure modification.

The pressure effects on CMR are through the modification of both long range symmetry and local atomic structure (static/dynamic). The structure can become less or

more distorted under pressure. With structure modification, bandwidth, electron-phonon interaction and spin state are correspondingly modified, resulting in metal-insulator transition, higher Curie temperature, low resistivity, etc.

2.2.1 On Bandwidth

The bandwidth W characterizes the hybridization of Mn e_g orbital and O^{2-} 2p orbital. It is determined by the Mn-O bond length and the Mn-O-Mn bond angle. In double exchange theory, the bandwidth is characterized with the transfer integral (or the electron hoping) [equation (1.3)]. With tight band approximation, W can be described empirically as:[142]

$$W \propto \frac{\cos(\frac{1}{2}(\pi - < \beta >)}{d_{Mn-O}^{3.5}} \qquad (2.1)$$

where β is Mn-O-Mn bond angle, d_{Mn-O} is Mn-O bond length.

Bandwidth can be modified by chemical doping with different divalent elements through the bond angle and bond length. The different bond angle and bond length due to dopant and concentration induce intriguing electronic and magnetic phases as described in chapter one.

With the pressure studies on manganites in the range below ~2 GPa, pressure was found to have similar effect to chemical doping. In low range, pressure increases Mn-O-Mn bond angle while possibly compressing bond length simultaneously. As a function of W, Curie and/or metal-insulator transition temperature has been found always increased at low pressures, due to the pressure induced stabilization of FMM state.[29,143]

With W being increased by pressure, carrier mobility increases, the narrow band CO state can be suppressed and correspondingly FMM state is induced.[144] In a large body of high pressure work on CMR materials, T_C was found to linearly increase with pressure.[29,118,145,146,147,148,149] In the low pressure range, magnetic field has similar effect on T_C.[100,143] This can be explained with DE model: pressure affects t_0 part and magnetic

field affects $\cos(\theta_{ij}/2)$ part by aligning spins ferromagnetically. However, according to DE, the magnetic field effect saturates with increasing field. In the meantime, it was reported that in the low doping $La_{1-x}Sr_xMnO_3$ ($x = 0.12$-0.18) pressure affects T_{MI} by destabilizes the ordered JT polarons to enhance electron hoping and extend the FM metallic state to lower temperature while magnetic field has negligible effect, implying that spin plays minor role.[150]

Generally, pressure increases T_C by increasing W. For different system and doping concentration, the sensitivity of T_C to pressure, dT_C/dP, is doping level and dopant, or $\langle r_A \rangle$ dependent. The manganites with small $\langle r_A \rangle$, correspondingly low T_C, have larger local disorder, and therefore have higher pressure sensitivity, which results from the pressure suppression of the local disorder.[151] In $La_{1-x}Ca_xMnO_3$, with x increasing, dT_C/dP for $x = 0.21$ is 36.7K/GPa, for $x = 0.33$, 15.7 K/GPa and for $x = 0.40$, 16.0 K/GPa.[143] Moritomo *et al.*[29] studied the low pressure effects (up to 0.8 GPa) on $La_{1-x}Sr_xMnO_3$($0.15 \leq x \leq 0.5$) crystals. They found that the pressure coefficient of T_C is significantly x dependent and steeply decreases from $d\ln T_C/dP \sim 0.065\ GPa^{-1}$ at $x = 0.15$ to a small value ($\sim 0.005\ GPa^{-1}$) at $x = 0.4$–0.5 (Figure 1.22). This suggests an asymptotic change of the electronic nature from the strong- to weak-coupling region with increasing hole-doping level.

By studying a series of manganites $L_{2/3}A_{1/3}MnO_3$ (L = Pr, Sm, Nd, Y, La; A = Ca, Sr), Laukhin *et al.*[145] found that under pressure while T_C shifts to higher temperature thus stabilize the metallic phase, $d\ln T_C/dP$ increases pronouncedly when the relevant bandwidth becomes narrower. They ascribed this to the dependence of bandwidth on Mn-O-Mn bond angle and its compressibility under pressure and the reduction of electron-phonon coupling under pressure, which is more prominent as bandwidth is reduced. By substituting part of the Ca with Sr in $La_{0.7}Ca_{0.3-x}Sr_xMnO_3$ ($0 \leq x \leq 0.3$), Maksimov *et al.*[152] found that dT_C/dP and dT_{MI}/dP are higher for $x < 0.15$ and $x > 0.15$ than for $x = 0.15$. T_{MI} at $x < 0.15$ and $x > 0.15$ has different pressure dependence, which is due to the

structural phase transition from orthorhombic phase ($x < 0.15$) to rhombohedral one ($x > 0.15$). In another system $La_{0.7-x}Cs_xCa_{0.3}MnO_3$ ($x = 0$-0.1), the trivalent La is substituted by the single valence Cs with smaller size, up to 1.2 GPa, the dT_C/dP is constant, in the range of $x = 0.01$-0.03, dT_C/dP increases with x and reaches maximum at $x = 0.03$ and in the $x > 0.03$ range, dT_C/dP only change slightly with x.[153]

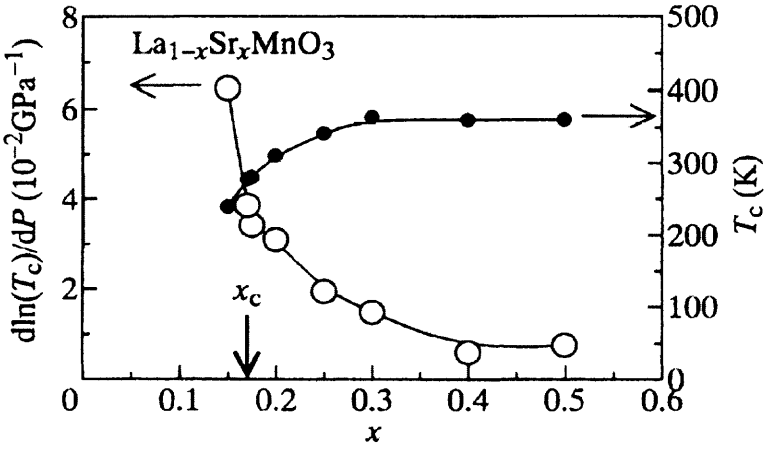

Figure 2.2 Doping dependence of T_C and pressure coefficient of $La_{1-x}Sr_xMnO_3$.

Note: T_C: solid circles; pressure coefficient: open circles. The downward arrow indicates the critical concentration for the insulator-metal transition.[29]

The doping dependence of dT_C/dP can be understood by considering the local structure distortion induced by substitution. The $\langle r_A \rangle$ reduction by doping induces larger local distortion, e.g. smaller bond angle and more local disorder. This leads to a smaller W and hence, lower T_C. With the local distortion being suppressed by pressure, T_C is greatly increased, resulting in a large dT_C/dP. On the other hand, with large $\langle r_A \rangle$, the small distortion leads to a relatively small dT_C/dP. This is comparable to that in thin films, in which the relative weight of distortion decreases with the thickness increasing. dT_C/dP is expected to be small in thick film. This has been demonstrated with the $La_{2/3}Ca_{1/3}MnO_3$ thin films by Jacob *et al.*[154] In pressure range up to 8 kbar, with thickness increasing, dT_C/dP reduces linearly and for higher T_C, $d\ln T_C/dP$ is less pressure sensitive.

2.2.2 On Structure

Pressure affects the CMR material structures in two aspects: the crystal symmetry (long range order) - pressure induced crystal structure transition, and local atomic structures.

At present, most of high pressure studies on manganites are limited in a relatively low range, very rare pressure induced structure transitions have been reported.

The most salient effect of pressure is on the local atomic structure. While compressing the lattice unit cell, the atom positions, especially the oxygen positions, may be shifted so that the local atom structure is distorted. In manganites, the most important local structure is the MnO_6 octahedra. Under pressure, because of the oxygen atom position moving, the Mn-O bond lengths and their correlations, the Mn-O-Mn bond angles may be changed. This affects the bandwidth due to the change of overlap of the Mn^{3+} e_g orbital and O^{2-} 2p orbital.

Another pressure effect is on the dynamic effect, - the phonon modes and frequencies that are correlated with the electron-phonon interaction.

In lightly doped $La_{1-x}Sr_xMnO_3$ compound, upon cooling, the structure transforms from rhombohedral phase to orthorhombic phase at transition temperature T_s. Itoh *et al.*[155] observed that T_s of single crystal $La_{0.85}Sr_{0.15}MnO_3$ decreases with increasing pressure. Pressure extends the rhombohedral structure phase to lower temperature and T_C simultaneously increases. This suggests that the lattice distortion is relaxed and the double exchange interaction is enhanced by pressure. Moritomo *et al.*[150] reported the pressure effects on structure transition of a similar compound $La_{0.83}Sr_{0.17}MnO_3$ (Figure 2.3). It was found that under pressure the orthorhombic-rhombohedral structural transition (T_s) and T_C only slightly change with pressure below 0.1 GPa, then T_s abruptly drops from ~280 K to 230 K.

Similarly in another doped manganite $La_{0.8}Ba_{0.2}MnO_3$, it was found that up to 10 kbar pressure shifts rhombohedral to orthorhombic structural phase transition temperature T_s down, and $T_C \sim 255$ K is shifted concomitantly to higher temperatures.[156]

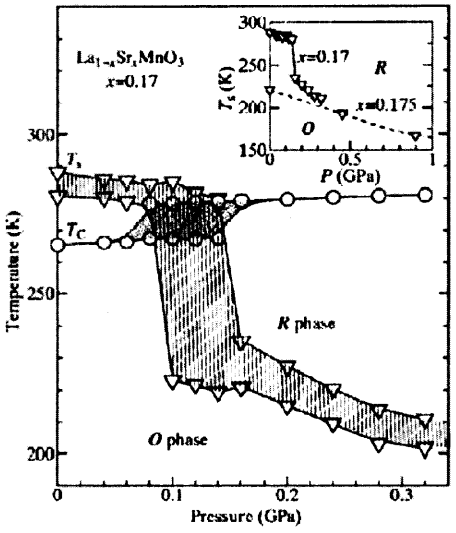

Figure 2.3 Pressure-temperature phase diagram for $La_{0.83}Sr_{0.17}MnO_3$.

Note: triangles and circles represent T_s and T_C, respectively. The hatching regions represent the thermal hysteresis. Inset shows comparison of the structural phase boundaries (in the warming run) for x = 0.17 and 0.175. Note that the horizontal axis is the calibrated pressure.[150]

Generally, in the low pressure range, pressure reduces the local distortion of MnO_6 octahedra and induces larger W. This has been proved by the T_C increasing with pressure in various doping systems. In addition, the stiffness of phonon can also change with pressure. The static and dynamic Jahn-Teller distortion and their state are under the influence of pressure as well. Under pressure up to 80 kbar, in the undoped parent compound $LaMnO_3$, it was reported that pressure decreases the global orthorhombic distortion almost isotropically, while the Jahn-Teller distortion keeps stable in this pressure range.[157]

In the low doping $La_{1-x}Sr_xMnO_3$ system,[150] pressure extends the FMM phase by totally suppressing the FMI phase at ~1.4GPa. This is ascribed to that pressure destroys the JT polaron ordering to enhance the e_g electron hopping. That magnetic field has little effects on MIT suggests that electron-lattice coupling plays important role in the transport properties of $La_{1-x}Sr_xMnO_3$ with maximal bandwidth.

In manganites, because of electron-phonon coupling, resistivity is much higher than

that predicted by theories. Under pressure, the electron-phonon coupling can be reduced, resulting a lower resistivity and higher T_C. In $La_{0.65}Ca_{0.35}MnO_3$, the oxygen isotope effects on metal-insulator transition and electronic properties were investigated with pressure up to 1.7 GPa.[158] It was found that samples with ^{16}O and ^{18}O almost have the same pressure dependence of dT_C/dP and that of conductivity activation energy of the adiabatic hopping of Jahn-Teller polarons. Laukhin *et al.*[145] suggested that the significant reducing of $d\ln T_C/dP$ with T_C dropping, which comes primarily from the Mn-O-Mn bond stretching, is much larger than that bandwidth theory expects, implying that electron-phonon coupling is reduced.

In crystal $La_{0.9}Sr_{0.1}MnO_3$, Senis *et al.*[159] found that both magnetic field and pressure stabilize the low temperature charge ordering state (T_{CO} increases with pressure and magnetic field increasing). This is different from the case that pressure suppresses CO state because of the carrier localization due to local distortions.

When the unit cell is compressed, JTD modes can be changed. Wang *et al.*'s[160] high pressure x-ray diffraction studies on $La_{0.5-x}Bi_xCa_{0.5}MnO_3$ (x = 0.1, 0.15, 0.2) display an abnormal change of the 202-040 d-spacing at 1.2, 1.4, and 1.6 GPa, respectively. They ascribed it to the disappearance of distortion mode Q2 of MnO_6 octahedra, which results in a reduction of Jahn-Teller distortion. Due to the modification to local structure, such as the Mn-O bond distance and Mn-O-Mn bond angle, with pressure increasing, mode Q3 becomes dominant while mode Q2 within the ab basal plane disappears at ~1.8 GPa.

In the low pressure range (< 2 GPa), pressure may enhance the rhombohedral phase and suppress the local distortion and electron-phonon coupling. All of these only enhance or suppress some electronic and/or magnetic state without inducing transition. These changes under pressure can also be reached by selecting proper doping elements and doping levels. So pressure is considered equivalent to chemical doping. However, there have been some indirect indications that the behavior of CMR oxides may be different from that observed in the low pressure measurements for pressures above 2 GPa.

Raman scattering results by Congeduti *et al.*[161] on $La_{0.75}Ca_{0.25}MnO_3$ indicated that above 7.5 GPa, high pressure induces a new phase other than the predicated metallic phase. The abrupt phonon frequency change and strong phonon broadening suggest a charge-lattice interaction strengthening by the lattice compression. Meneghini *et al.*'s[162] results reveal that in addition to the general unit cell contraction, pressure above 6-7GPa causes the Jahn-Teller distortion of MnO_6 octahedra. The octahedra become more distorted by splitting the two almost identical in-plane Mn-O bond lengths and produces a longer range static/dynamic JT distortion.

2.2.3 On Electron Transport and Magnetic Properties

In manganites, the local structure distortions (static or dynamic) lead to strong electron-lattice interactions. The electronic transport properties are sensitive to these local distortions. So chemical doping, strain induced by substrate in thin films, material preparation condition, hydrostatic pressure, etc., affect the electronic transport greatly. The change of distortion state leads electron to be localized or delocalized and may lead magnetic transition as well due to the coupling between electronic and magnetic states.

The ferromagnetism and electronic state are strongly coupled to lattice distortion which can be relaxed by external pressure and annealing at high temperature.[155] Due to pressure induced transfer integral increase, the ferromagnetic metallic state is enhanced. With pressure increasing, conductivity and T_C increase. In paramagnetic insulating phase, due to the suppression of local distortion and electron-lattice interaction, resistivity was observed to decrease. In the $La_{1-x}A_xMnO_3$ system (A = Na, K, Rb, Sr) with a rhombohedral structure, below T_C, pressure up to 1.1GPa reduces resistivity by more than 60%, the effect is less pronounced above T_C.[163]

In the two typical electron transport models, the polaron mechanism emphasizes polaron transport. The so-called polaron may involve several lattice sites which is called

a large polaron. Experiments indicated that large polaron has magnetic characteristic. For the VRH mechanism, electron transport is the result of electron hoping in a disordered lattice. In manganites, this disorder is magnetic.

Despite the difference between these two models, they do share some similar characteristics: the hoping distance estimated with VRH model is in the same scale as polaronic cluster size. In addition, both polaron and disorder are the result of local structure distortion and electron-lattice interaction. The distortion of the MnO_6 octahedra and its tilting are the key to the formation of both polaron and disorder.

The pressure effects on resistivity reflect the changes of Mn-O bond, the Mn-O-Mn bond angle, and the electron-phonon coupling.[145] In addition, because of electronic state changes, magnetic state is also under the affect of pressure. Pressure directly affects the structure, so it may increase electron hoping in the whole temperature range, while magnetic field may only take effects at some temperatures.[118]

For the polaron model: pressure effect is to destabilize the ordered JT polarons to enhance electron hoping and extend the FM metallic state.[150] In $Nd_{0.62}Pb_{0.30}MnO_{3-\delta}$, up to 12 kbar, pressure shifts T_{MI} linearly to higher temperature at rate 2.6 K/kbar, while magnetic field shifts T_C up, but does not affect dT_{MI}/dP. Magnetic field only affects electron hoping near T_{MI} while pressure increases hoping at all temperatures.[118] Teresa *et al.*'s[100] work on $La_{2/3}Ca_{1/3}MnO_3$ also shows that magnetic polarons exist above T_C, magnetic field and pressure favor electrical conduction by enhancing the double-exchange interaction. Neumeier *et al.*'s[143] results on $La_{1-x}Ca_xMnO_3$ ($x = 0.21, 0.33, 0.4$) under pressure up to ~1.7 GPa indicate that the effects of pressure is analogy to magnetic field. The resistivity above T_C can be considered as arising from the propagation of magnetic polarons. Lorenz *et al.*[158] measured the oxygen isotope effect on metal-insulator transition and the electronic properties of $La_{0.65}Ca_{0.35}MnO_3$ under hydrostatic pressure up to 1.7 GPa. They accounted the linear behavior of conduction activation energy in the insulating phase under pressure and isotope effects in terms of double exchange model

and the adiabatic hopping of Jahn-Teller polarons.

For variable range hoping, the role of pressure is to increase localization length. For example, in $(La_{1-x}R_x)_{0.67}Ca_{0.33}MnO_3$ (R = Y, Tb), resistivity in paramagnetic phase is considered to be represented by Mott localization law. Under pressure, the characteristic temperature T_0 decreases with pressure increasing.[164]

Dynamic lattice distortion is also important to the electronic transport. Zhou *et al.*'s[165] resistivity and thermopower measurements at high pressure indicate that in $Ln_{1-x}A_xMnO_3$, below T_C, strong interactions between electrons and dynamic local lattice distortions associated with Mn sites is important. Below T_C, conduction electrons lose their localized character and condense into extended electronic states that exhibit no energy dispersion. The authors attribute the formation of this new state to strong coupling of the conduction electrons to cooperative oxygen vibrations along Mn-O bond axes.

For magnetic states, in DE model, pressure enhances FM and metallic state. However, it was also found that in low doping $La_{1-x}Sr_xMnO_3$ (x = 0.1-0.14), which has a FMM to FMI transition upon cooling, pressure extends the insulating state (Figure 2.4).[147] This is ascribed to the FM superexchange enhancement by pressure through the orbital ordering enhancement.

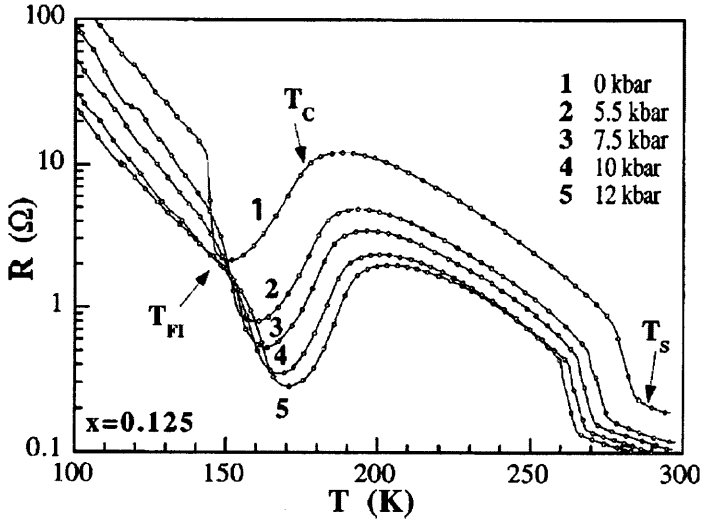

Figure 2.4 Temperature and pressure dependence of resistance of $La_{0.875}Sr_{0.125}MnO_3$.[147]

Tissen *et al.*[148] showed that in $La_{0.9}Sr_{0.1}MnO_3$ single crystal, pressure below 20 kbar stabilizes the low-temperature charge ordered state and FM state, but at higher pressure, a new magnetic transition occurs at high temperature.

In $LaMnO_3$, pressure up to 70 kbar stabilizes the A-type AFM state with dT_N/dP of ~0.3-0.35 K/kbar. Above 70 kbar, possibly because of JT effect suppression, a new metallic-like phase is induced; at low temperature, pressure increases the transition temperature and suppresses magnetic ordering.[157] Sirota *et al.*[166] reported that pressure up to 4 kbar decreases the Néel temperature at 3 K/kbar and with the suppressing of AFM phase, FM component appears due to the Mn-Mn superexchange.

In $Nd_{0.5}Sr_{0.5}MnO_3$, at ambient environment, a coupled CO, AFM and insulating phase arises from the metallic FM state with temperature decreasing. But under pressure, this coupled state is spilt while magnetic field can recover it (Figure 2.5).[167]

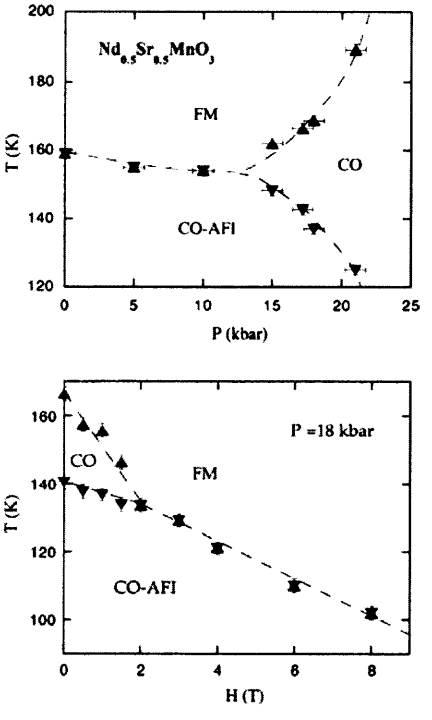

Figure 2.5 Phase diagrams in pressure and magnetic field of $Nd_{0.5}Sr_{0.5}MnO_3$.

Note: the data were taken on cooling. Pressure stabilizes charge order up to high temperature, while depressing antiferromagnetism. Magnetic field drives both transitions to lower T, but charge order more quickly, until they merge once again. FM: ferromagnetic metal; CO: charge order; AFI: antiferromagnetic insulator.[167]

2.2.4 Compared with Strain in Thin Films

In contrast to hydrostatic pressure, strain induced by lattice mismatch between substrate and thin films is anisotropic. The strain in thin film is thickness dependent and makes it more local distorted than in bulk.[168] This kind of distortion relevant to Jahn-Teller distortion is biaxial and can increase the JT splitting of the e_g orbital so that electrons become more localized.[169] So CMR thin films with high strain tend to be insulating.

Millis *et al.*[170] demonstrated with their experiments and theoretical model that substrate-induced volume-preserving even parity (Jahn-Teller) strain is crucial to the properties of thin films. Ahn's[171] calculation show that 2% tensile uniaxial strain, the order of magnitude of those induced in thin films by lattice mismatch with substrates, can change the orbital state and magnetic ground state significantly.

Prellier *et al.*[172] found that the highly strained 200 Å thin $Nd_{0.5}Sr_{0.5}MnO_3$ film is insulating while in the thick film of 2000 Å there is no CO transition as in bulk material but only a metal-insulator transition, and the mediate film 500 Å only has a slight CO transition. Qian *et al.*'s[173] work suggested that biaxial strain in thin film helps to stabilize JTD and enhance electron localization to induce CO, and there is an optimal strain that leads to metallic behavior with vanishing JTD in the films above 1000 Å.

It was also reported that in $La_{0.67}Ca_{0.33}MnO_3$ thin films, the biaxial strain can weakens the low-temperature ferromagnetic metallic state and produce small charge-ordered insulator clusters in high strain regions and lead to a FMM and COI phase coexistence at low temperature.[174,175,176] Song *et al.*[177] deposited $La_{0.7}Ca_{0.3}MnO_3$ thin films on different substrates, they found that the anisotropic strain induces different unit cell volume and symmetry, and with unit cell volume increasing, T_p change monotonically; but when symmetry changes from negative tetragonal ($a > c$) to nearly cubic ($a \approx c$) and then to positive tetragonal ($a < c$), T_p across a maximum.

Based on their results of $La_{0.88}Sr_{0.1}MnO_3$ thin films on (100) $SrTiO_3$, Wang *et al.*[178] suggested that the metallic behavior in thin films (100Å) with a higher T_C is due to the

suppressing of JTD by epitaxial strain and the insulating behavior in thick films (2500Å) is induced by the recovered JTD because of the strain relaxation.

In $La_{1-x}Ba_xMnO_3$ (x = 0.05, 0.1, 0.2, 0.3, 0.33) thin films, Zhang *et al.*[179] and Kanki *et al.*[180] found the abnormality that tensile strain enhances FMM state and hence, T_C, while compressive strain reduces T_C. They suggested that the tensile (compressive) strain induces the in-plane bond length increasing (decreasing) and out-plane bond length decreasing (increasing). This leads to charge transfer from $d_{3z^2-r^2}$ orbital to $d_{x^2-y^2}$ orbital with larger transfer intensity (or vice visa). But Yuan[181] argued that the so-called anomalous are due to the bond angle increasing/decreasing under tensile/compressive strain while the Mn-O bond length keep almost unchanged.

The strain in thin films decreases with film thickness increasing. It has been shown that the anisotropic strain can be suppressed by pressure. Moshnyaga *et al.*[182] found that in epitaxial $La_{0.7}Ca_{0.3}MnO_3$/MgO(100) thin films, pressure decreases the resistivity and increases T_{MI} as in the bulk materials which implies that at least part of the strain is suppressed.

2.2.5 Effects of Pressure and Chemical Doping

In the low pressure range (< 2 GPa), in most cases pressure was found to stablize the FMM state and increase the transition temperature T_C. In this range, pressure is analogy to the chemical doping with elements with larger ion size. In the bandwidth theory, the evolution of electronic bandwidth as a function of ''chemical'' and applied pressure can qualitatively explain the similar dependence of T_C on pressure and $\langle r_A \rangle$.[183] For example, in $(Nd_{1-y}Sm_y)_{0.5}Sr_{0.5}MnO_3$, it was found that with substituting Nd with Sm, the low temperature AFM state disappear at y > 0.8, but under a pressure 0.7 GPa the state is mostly recovered, indicating the same effect of pressure and chemical doping.[184]

By comparing the effects of chemical doping and pressure below ~2 GPa, it is

generally accepted that the effects of hydrostatic pressure is equivalent to that of chemical doping. Generally, the chemical doping effect, sometimes referred as internal chemical pressure, is described with the average A-site atom size $<r_A>$ [or equivalently the tolerance factor t (equation (1.8))]. Hwang *et al.*[185] systemically studied the effects of external hydrostatic pressure and internal chemical pressure on properties of CMR and found that the pressure and chemical doping effects can be correlated with a conversion factor of 3.75×10^{-4} Å/kbar in the relation $\delta < r_A > (\text{Å}) = 3.75\times10^{-4}$ P(kbar). With this conversion factor, the effect of hydrostatic pressure can be mapped to the phase diagram of average radius of the A site atoms (Figure 2.6).

According to this, because most of the metal-insulator transition temperature of manganite is below room temperature, pressure high enough should be able to induce metallic state at room temperature, but recent results have shown that pressure can possibly either suppress or induce structure distortion and/or the electron-phonon interaction.[161,162] With the development of high pressure technique, now with diamond anvil cells, it is possible to study the CMR properties under pressure much higher than before. From several other authors' and our work, it is found that effects of pressure are far more complicated than in the low pressure range explored previously.

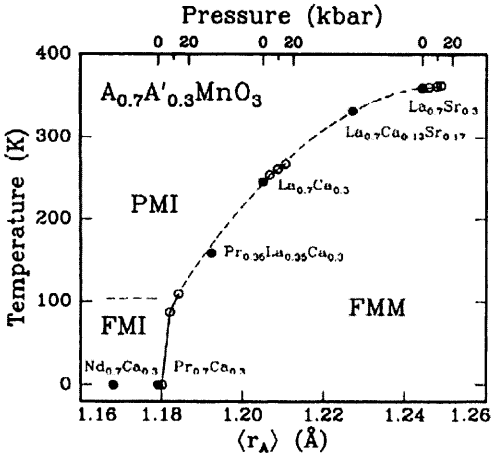

Figure 2.6 Phase diagram of $A_{0.7}A'_{0.3}MnO_3$ as a function of transfer integral.

Note: the transfer integral was varied by both chemical doping and external pressure.[185]

CHAPTER 3

HIGH PRESSURE EXPERIMENTAL TECHNIQUES AND SAMPLES

3.1 Introduction

Of all the physical variables, pressure spans the largest range of over 60 orders of magnitude in the universe, from the non-equilibrium "pressure" of hydrogen gas in intergalactic space (10^{-31} atm) to the pressure at the center of neutron star (10^{28} atm). However, the high pressure study in solid-state physics had kept untouched until the Bridgeman era (roughly from 1910 to 1950). With diamond anvil cell, pressure achieved in laboratory has been extended to ~560 GPa, higher than that at the center of the earth.[186] Since the beginnings of high pressure techniques, many different pressure devices have been developed. Due to its various advantages, DAC is the most extensively used one. In addition, pressures above several tens of GPa are uniquely achieved with DACs.

As the hardest material, diamond is ideal for high pressure generation. The highest thermoconductivity and being transparent over wide electro-magnetic radiation spectrum spanning IR, VIS, UV and x-ray range also make it ideal for high pressure spectroscopic experiments and cryogenic related research.

DAC is relatively simple and is the only instrument attaining megabar static pressures. The simplicity of DAC makes it possible for any laboratory to have the opportunity to use pressure as a tool to investigate material behavior up to at least 100 GPa. In addition, the size of DAC is quite small, even as small as a quarter dollar coin, so that it can be fit into experimental equipment with limited working space, such as small cryostat, magnet bores with very high magnetic field. Due to their versatility, DACs have been used in many experiments: optical absorption, reflectivity, Raman scattering, x-ray diffraction,[187] electron and nuclear resonance spectroscopy,[188] infrared spectroscopy, magnetic susceptibility measurements, etc.

3.2 Principle of Diamond Anvil Cell

The basic principle of the DAC is quite simple. A typical one is shown in Figure 3.1. It contains two identically cut diamonds of gem quality, with tips being flattened to culets of the size from several tens of μm to 1 mm, depending on required pressure limit. The back surface of the anvils, the "table", has a surface 25 to 1000 times larger. Each diamond is mounted onto a metallic part, the back plate, with a much larger cross-section than the diamond tables with the table side seated on the back plate. The two culets face each other. When they are pressed against each other with moderate force acting on the back plates, high pressures can be achieved at the culet surfaces. If a sample is placed between the culets, the sample will be pressed. However, this direct contact will break the diamonds very easily and the pressure on the sample is highly non-hydrostatic. To protect diamonds and get hydrostatic pressure on the sample, two more things are important: the gasket and the pressure medium. Generally, a metal gasket is placed between the two culets. On the gasket, there is a small hole used as sample chamber. The sample and ruby chips for pressure calibration are placed in the hole. Some pressure medium is filled in the hole. When the gasket is squeezed by the two opposing diamond culets, due to the contraction of gasket hole, pressure in it is increased.

Different DACs have been designed for various purposes and pressure ranges. According to the mechanism of force-generation and anvil-alignment, there are five basic types: NBS cell, Bassett cell, Mao-Bell cell, Syassen-Holzapfel cell and Merrill-Bassett cell.[187] The Merrill-Bassett cell is the simplest one in which the force for pushing anvils together is provided by three screws (Figure 3.2). This cell is quite compact and can fit into small spaces. Although originally designed for single crystal x-ray diffraction, it can be used for many other purposes, such as resistivity measurements, optical measurements, etc., with additional accessories. The cells we used for x-ray diffraction and resistivity measurements have a similar configuration to the Merrill-Bassett cell.

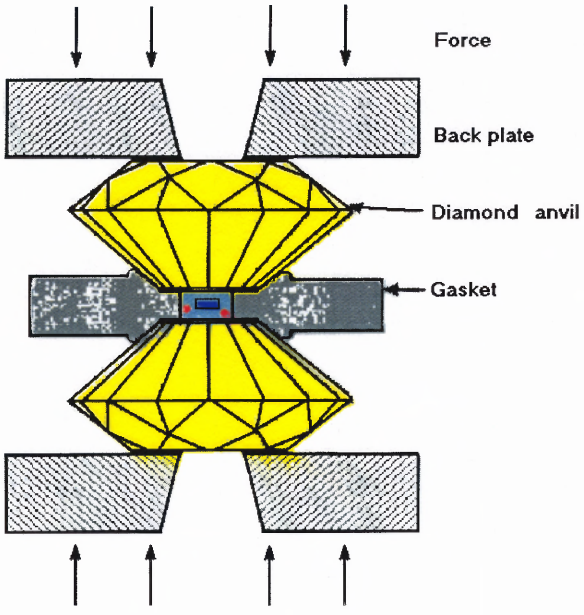

Figure 3.1 Basic diamond anvil cell configuration.

Note: the rectangular in the gasket hole represents the sample; the spots around sample are ruby chips, and the liquid pressure medium is filled in the hole.

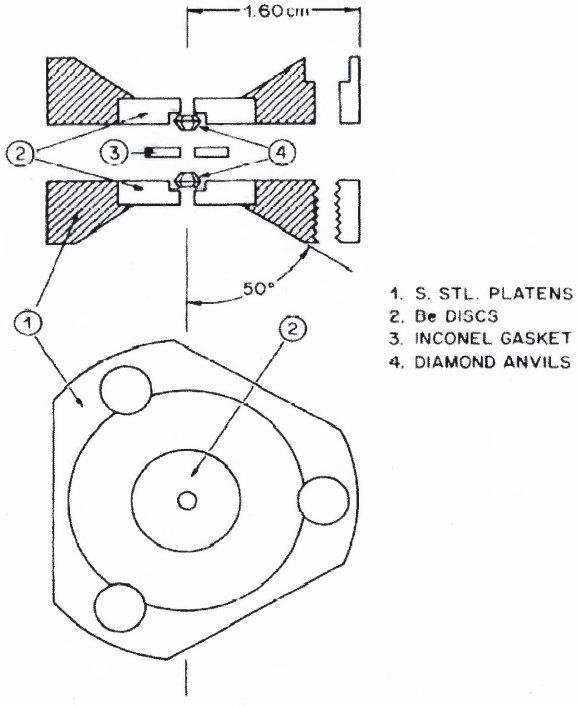

Figure 3.2 Merrill-Bassett diamond anvil cell.

Note: the diamonds are set in beryllium backing plates and the force is applied by tightening the three symmetrically located screws.[187]

Although it is still difficult to acquire pressure of hundreds of GPa, it is a routine to acquire pressures below 100 GPa. A variety of DACs is commercially available for different research purposes.

Because there have been several good reviews and publications, except the special details in our experiments, the general information will not be reviewed here. The work of Jayaraman[187,189], Eremets[188] and Dunstant[190]are good references for various DAC designs, theories, and applications. For the DAC operation, Spain[191] described many details such as diamond mounting and alignment, gasket preparation, and sample preparation and handling, so that it can be used as a manual for DAC operation.

3.3 Pressure Calibration

Measuring pressure at sample had been a major problem in high pressure studies. Different calibration techniques have been developed. The most direct one may be that of measuring the force applied on diamond anvils and then dividing the force with the culet area to acquire the pressure. This only works with hydrostatic pressure and in most pressure cell designs is not practical. In x-ray diffraction, the pressure can be calibrated by placing materials with well-known pressure dependence of lattice parameters, such as NaBr, Ge, NaCl, Cu, Ag, into the cell together with sample. By measuring the lattice parameter changes of the pressure markers, pressure can be determined. Other methods such as by measuring the resistance of standard markers, Mn, InSb, etc. and the superconduction or magnetic transition temperatures of Pb, In, $HoCo_2$, $ErCo_2$ etc. are also used in different cases.

Of all the methods, ruby fluorescence method is the most convenient one working with DAC. Ruby has a doublet R fluorescence line of 694.34 nm at 300 K and ambient pressure. When loading samples into DAC, several tiny ruby chips of 5-10 μm in dimension are placed into the gasket hole along with sample and pressure medium. The

fluorescence of ruby can be excited with laser or strong light with shorter wavelength than the fluorescence line. With pressure increase, the doublet R lines of R_1 and R_2 shift to longer wavelength. The shift is almost a linear function of pressure. The pressure can be calibrated up to 200 GPa with an empirical formula:[192]

$$P(GPa) = 248.4[(\lambda_p / \lambda_0)^{7.665} - 1] \tag{3.1}$$

where λ_0 is the wavelength of ruby R_1 line at ambient pressure and fixed temperature (694.2 nm at 300K), λ_p is the wavelength at pressure P and same temperature. The accuracy of absolute pressure measurement is believed to be within 15-20% at ~200 GPa.[193] Figure 3.3 is the ruby pressure scale.

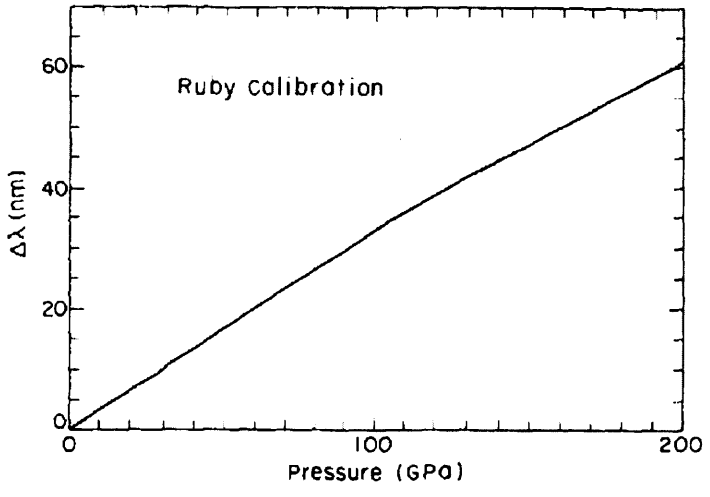

Figure 3.3 Ruby scale calibration based on the equation of state (EOS) of Au.[189]

Because the wavelength of the R line also depends on temperature,[194,195] to do *in situ* pressure measurements at different temperatures, it is necessary to correct it. The wavelength of the R_1 line at given pressure and temperature is:

$$\lambda_{R1}(P,T) = \lambda_{R1}(P,T_0) + \Delta\lambda_{R1}(T) \tag{3.2}$$

where T_0 is the reference temperature. The correction term $\Delta\lambda_{R1}(T)$ is:

$$\Delta\lambda_{R1}(T) = C_1(T - T_0) + C_2(T - T_0)^2 + C_3(T - T_0)^3 \tag{3.3}$$

The ruby scale has been calibrated at different temperature and pressure ranges by several

groups. Different sets of C_i (i = 1, 2, 3) coefficients were acquired (Table 3.1). All these different calibrations consistent to each other well in the high temperature range from 270 K up to 400 K. There are some differences between them in low temperature range. Besides the cubic polynomial correction, several other empirical formulas are also used.[196,197,198,199,200]

Table 3.1 Correction Coefficients of Ruby R_1 Line Wavelength Shift with Temperature

	C1	C2	C3	Temperature Range
1	6.5910E-02	7.6240E-05	-1.7330E-07	150-400 K
2	6.9200E-03	7.1406E-06	-1.7779E-08	0-600 K
3	6.9600E-02	7.6771E-06	-1.6970E-08	unknown
4	6.8581E-03	4.9137E-06	-3.3064E-08	> 80 K

Note: 1 from ref. 201; 2 from ref. 202, the original correction is in cm^{-1}, the data in this table has been recalculated to nm; 3 from ref. 203; 4 from ref. 204.

The ruby fluorescence technique becomes ineffective when high pressures and high-temperature conditions coexist. So the other pressure scale of the Sm:YAG fluorescence, which is independent of temperature,[205] is developed. The Sm:YAG scale has been investigated by several groups.[206,207] The disadvantage is the much weaker intensity than ruby at low pressures.[208]

Because of the resistivity measurements of this work require *in situ* pressure measurements at different temperatures. A system as that in Figure 3.4 is used. All the parts before the optical fiber, including a laser diode, are mounted on a XYZ stage so that it can be conveniently moved around. The focal length of the objective len is ~35 mm. So it can detect the ruby fluorescence in a cryostat though an optical window. The collected fluorescence is feed into the spectrograph through optical fiber. Then the shift is measured and pressure is calculated.

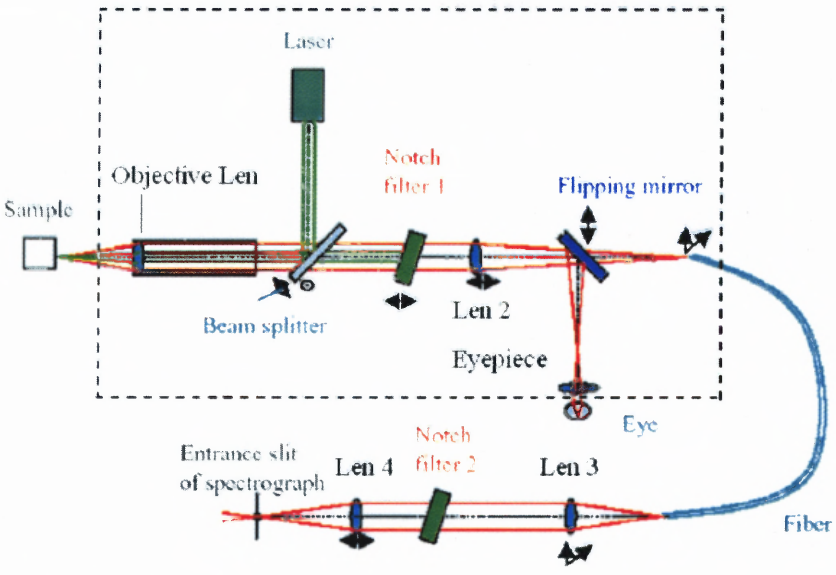

Figure 3.4 Ruby fluorescence pressure calibration system.

Note: the arrows designate possible adjustment; the parts in the dashed line rectangle are mounted on a 3D XYZ stage.

3.4 High Pressure Techniques

3.4.1 Gasket Preparation

Gasket is crucial to hydrostatic pressure measurements. In addition to providing a chamber for sample and pressure medium for hydrostatic pressure generation, while being compressed, gasket extrudes around diamond tips as a supporting ring to protect anvils from breaking. The theories about gasket can be found in ref. 188, 190, 191, 209.

3.4.1.1 Materials. Several materials have been used for gasket, such as hardened stainless steel T301,[210] Inconel X750 and Waspalloy,[187] rhenium, etc. For some special requirements, such as in sapphire anvil cells and in magnetic measurements, CuBe alloy is used as gasket material. In the low energy high pressure x-ray absorption and diffraction, beryllium is used for its low absorption to x-rays – certainly, much more attention should be paid when preparing it, due to the beryllium oxide which may cause the chronic beryllium disease that affects the lungs.

3.4.1.2 Thickness. As some theories indicated,[188,190,191,209] thickness is an important

factor affecting the upper pressure limit. But for general users who do not need very high pressure, thickness seems not very critical. The commercially available metal sheet with thickness ~100-500 μm can satisfy most requirements.

3.4.1.3 Preindent, Guiding Hole and Gasket Hole. As Spain and Dunstan[191] reviewed, the preindent has several advantages: a) to acquire any required gasket thickness; b) to provide a thick belt of metal supporting for the material between culets and flanks of diamonds; c) to center sample and ruby on the diamond culet and center sample hole easily; d) to allow automatic selection of correct gasket thickness, by applying the same load to preindent as will later be used in pressure run.

Moreover, together with the guiding holes, preindent also makes loading the gasket back to diamond anvil much easier. For the diamond anvil cells with position pins, drilling holes fitting to the pins helps to seat gasket back.

The procedure is: before loading gasket to DAC to make the preindent, first drill a guiding hole. This can be done as suggested in the Figure 2. of ref. 191 by making a template at first. But sometimes just drilling a hole the size of position pin also helps much. After the guiding hole being drilled, seat the gasket on the base diamond anvil, then close the cell and tight it to make the indent. The depth of the indent or the final thickness of the gasket can be monitored and controlled with a micrometer. For the Merrill-Bassett type DAC, the thickness of the cell is only about a quarter inch. So the gasket thickness can be monitored by measuring the thickness of the whole cell at different places with the micrometer.

The next step is to drill the gasket hole. To get very high pressure, the hole size should be as small as possible to avoid failure. But it is more convenient to work with a large sample chamber in the case of sample amount important and all the high pressure resistance measurements. Different hole sizes have been used from ~tens to ~hundreds of μm in diameter. The hole size used is of ~350 μm in diameter with the original gasket thickness of 250 μm and the DAC culets 800 μm in the resistance measurement. The

pressure ~ 9 GPa was reached without much difficulty.

To drill the gasket hole, several methods and equipments can be used, such as the micro drill machine, laser and electrical discharge machining (EDM). Most of these equipments are over $10000. So these equipments are not financially efficient if no other use is made of it. The alternative homemade EDM is attractive. It was reported to be able to drill holes as small as 10 μm.[188] This machine is simple and effective. Most parts can be found in a general lab. Besides a microscope and a XYZ stage, only a DC power source, several resistors and capacitors, and an electronic breadboard are needed.

A similar circuit to that of Lorenzana *et al.*[211] is used in this work (Figure 3.5). The DC power supply is a variable DC source in 0-50 V; the resistor R1 is 100 Ω, used for limiting the current; R2 is a high power resistor, 4 Ω; C1 is an electrolytic capacitor. Capacitors of different value can be used, depending on the hole size, quality and cutting speed, generally in several to several tens of μF. The cutting wire is tungsten wire with the tip sharpened. The wire thickness is also variable depending on hole size. The wire is fixed to a XYZ stage so that it can be accurately centered in the gasket hole. The preindented gasket is fixed to a holder and placed under a microscope with the cutting wire. Details about operation can be found in ref. 211.

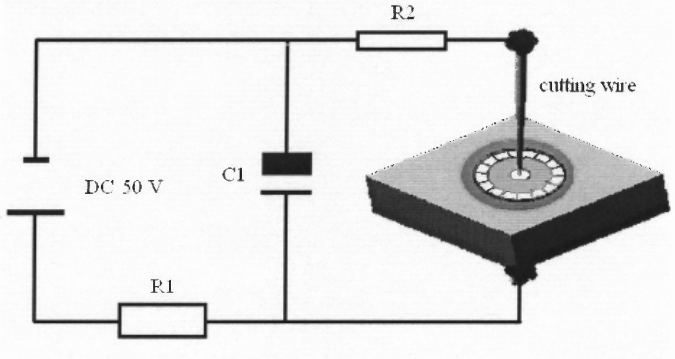

Figure 3.5 Electrical discharge machine.

To acquire high quality holes, the power, capacitor values and cutting wire thickness need to be optimized according to different gasket materials. Besides, the

dielectric fluid (coolant) is another factor important for the drilling speed and quality. The dielectric fluid is commercially available. But as suggested in ref. 211, other fluids such as vacuum pump oil, machine oil, kerosene, vegetable cooking oil, and other common organic solvents (e.g. methanol and ethanol) can also be used. Different gasket materials match different fluids. Generally, for hard materials, thinner fluid should be used while for soft materials, thick fluids should be used. After testing several fluids, we found that vacuum pump oil is too thick and has a smell and may produce poisonous smoke while operating; the cooking corn oil is also too thick; the pure organic solvents are too thin for stainless steel and the quality is very bad.

For stainless steel, we found water work pretty well. To speed up the drilling, several drops of ethanol is added to a beaker of water of ~40 ml. The other interesting finding is that the edible olive oil works very well with beryllium gasket making, while the corn oil and sesame oil do not work at all.

For the hole drilling, several other tricks may be helpful. First, because the gasket hole is so small, the quantity of fluid needed is also very small. While operating, it is better first to adjust the stage for the tip of cutting wire to be very near to the center of indent without sparks being excited, then use an eyedropper to put a very tiny drop of fluid in the indent. When adjusting the wire tip closer to the surface of indent, the fluid will start to flow with very high speed because of the heating created by electrical discharge. If the fluid is thick, while adding it to the indent, using a needle to immerse in the fluid, the amount on the tip is enough. While drilling the hole, the distance of cutting wire to hole should be adjusted to get good shape and quality.

After drilling the hole, for most experiments the gasket is ready to be loaded to DAC. But for electrical measurements, this is only the first step.

3.4.1.4 Gasket for Electrical Measurements. Of all the high pressure experiments, the electrical measurement is the most difficult one, especially in the case of hydrostatic pressure. Although it has been over twenty years since the beginning of such

experiments, not many good results have been reported. The difficulties come from two aspects:

The diamond anvils are small and correspondingly so are the samples. Except for the metal samples which can be made as thin wires, generally, the sample size is in ~100-250 μm dimension. To measure resistivity, on such small sample it is almost impossible to do standard four-point measurement. The Van der Pauw method is a little easier. To do this, four wires should be attached around the sample. The wires should be strong enough to avoid being broken and torn away from the sample while applying pressure.

The other problem is insulating the wires and sample from the metal gasket. For insulating gaskets, this is not a problem. Unfortunately, there is no insulating materials can yield as metal to be a satisfying gasket.

To do high pressure resistance measurements, three kinds of techniques were developed.

The first kind uses soft solid powder, such as NaCl and MgO, as pressure medium.[212,213,214,215,216] In this method, some soft powder is filled in the gasket hole and pre-pressed lightly, then sample and rubies are placed on the surface of the pre-pressed powder, wires are placed on the sample. In this way, the wires and sample are insulated by the powder. This method is suitable to wire samples, especially when the lead wires are the sample itself. One of its disadvantages is that when pressure is high, it may be highly non-hydrostatic for the solid medium.

The second method involves specially prepared anvils, such as depositing metal probes on the surface of diamond anvils[217] or making other special leads[218,219] or gaskets.[220] These methods involve complicated procedure to make leads or gaskets.

The other way is the so-called composite gasket. A ceramic thin layer is deposited[221,222] or coated with a mixture with epoxy[223] on the gasket. Generally, Al_2O_3 is used as the insulating material. This is a relatively simple way which only needs to coat a layer of Al_2O_3 or its mixture with epoxy on the gasket surface and the inside wall of

gasket hole. The pressure acquired with this kind of gasket is reported to be up to 23 GPa.[223] Based on this method, a procedure to prepare gaskets for high pressure resistance measurement was developed.

As in ref. 223, the mixture of 1:1 epoxy and Al_2O_3 in weight is used in the gasket making. The particle size of Al_2O_3 used is 37 nm. It is available from ALFA AESAR company. The epoxy used is Stycast 1266, which has optical clarity so that it can be used in optical elements. The low viscosity makes it easy to be mixed with large ratio Al_2O_3. Its superior mechanical properties at cryogenic temperature[224,225] make it ideal for low temperature applications. The procedure of preparing the gasket for resistivity measurement is:

1) Drill the gasket hole as described in section 3.4.1.3;
2) Boil the gasket in acetone for several minutes to clean it;
3) Fix four wires for electrical connection on one side of the gasket. For good and safe insulation of the wires, a thin layer of epoxy can be coated around the gasket hole (the blue area in Figure 3.6). The Stycast 2850 epoxy is the best for fixing the wires and be as the insulating layer due to its excellent thermo-expansion properties;
4) Waiting several hours for the epoxy to cure. The gasket can also be annealed at ~100 °C for fast cure of the epoxy;
5) Mix Al_2O_3 powder and Stycast 1266 A part according to the amounts calculated, then stir the mixture in one direction until it is uniform. Because only very tiny amount is used for each gasket making, the mixture can be made in large amount and kept properly for later use;
6) Take a small amount of mixture of Al_2O_3 powder and Stycast 1266 A part and weight it, then add the proper amount of catalyst (1266 B part). Mix it as in 5);
7) Coat a thin layer in the non-blue area in Figure 3.6, including the inside wall of the gasket hole. This needs to be done carefully and quickly. If a batch of

gaskets are made in one time, attention needs to be paid that the working time of the mixture is about 20 minutes;

8) After coating the mixture of Al_2O_3 powder and Stycast 1266, the gasket can be annealed at ~80 °C for several hours for the epoxy to cure.

With gasket prepared in this way and used with unbeveled diamond anvils, the highest pressure reached in our resistivity measurements is ~9 GPa. If the diamond anvils are beveled and the gasket material is harder, the upper limit will certainly be pushed up.

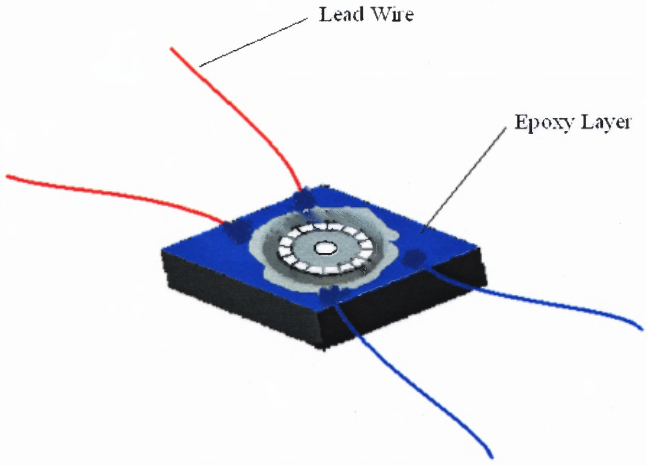

Figure 3.6 Gasket preparation for electrical measurement.
Note: the epoxy and Al_2O_3 mixture layer is coated in the non-blue area.

3.4.2 Pressure Medium

At room temperature, with the mixture of 4:1 methanol/ethanol, pressure was found to be hydrostatic up to ~10 GPa.[226] At low temperature, because of the mixture freezing, stress produces pressure difference between sample and ruby. So this medium is not suitable to low temperature applications. The solid gases, such as He, Ne, Ar, etc., may be the best medium to acquire hydrostatic pressure. Jayaraman[187] reviewed several different mediums in detail. Burnett *et al.*[227] compared Ar, Xe, He and 4:1 methanol/ethanol as cryogenic pressure medium. They found that Xe is severely non-hydrostatic, Ar is much

less non-hydrostatic and is a little improvement over the methanol/ethanol, helium is the best one and hydrostatic. At present, in the gas pressure mediums, helium is extensively used. The condensed gas mediums require special filling techniques and equipments.

For low temperature applications, the condensed gases are ideal. But sometimes, the 3M Fluorinert electronic liquids can also be used. The FC-77 is used for heat transfer due to its high thermal conductivity. In range from -110°C to 97°C, it is liquid. It also has high dielectric strength. Due to its good thermal property, it is used as pressure medium in high pressure studies on high temperature superconductors.[228,229,230,231]

Besides, some other pressure mediums used are the silicon oil, mineral oil, MgO and NaCl powder etc.

For its convenience and thermal property, FC-77 was used as pressure medium in the high pressure electrical measurements. Because the x-ray measurements are only performed at room temperature, 4:1 methanol/ethanol was used as pressure medium.

3.4.3 Sample Preparation

The samples used are made as pellets. Generally, it is not difficult to prepare samples for most high pressure measurements. However, for resistance measurements and powder x-ray diffraction, some points need to be paid attention to.

3.4.3.1 For Four-Point Resistance Measurement. A piece of sample is cut from a pellet. Then it is thinned and polished to a sheet of ~40-80 μm in thickness. The sample sheet is cut to small pieces of 150-200 μm square.

The difficult part is to make four leads on the sample. To do this, gold wires of 12.5 μm in diameter are cut to ~2 mm long. Then one end of the wire is flatten with the tip of tweezers. After the wires are ready, use micro-tweezers to pick up one and immerse the flatten end in a drop of silver paste. When taken out from the paste, there will be some silver paste on the head of the wire. Then stick it to one corner of the sample. This

procedure is repeated until four leads are all made.

Due to the very small sample size, all are done under a microscope. The working time of the silver paste is about 30 minutes, so the work needs to be done as quickly as possible.

After all the four wires are glued, the sample is put on a slide to be heat treated for one to several hours in an environment of ~80 °C for the silver paste to cure.

The wired sample needs to be mounted to the gasket prepared as in section 3.4.1.4. Before the sample is mounted, the four gold wires need to be trimmed to the length which can fit the whole sample in the range of the indent of gasket. Then the sample is placed in the gasket hole with the four wires extending in the indent. The wires are fixed in the indent with a little silver paste first. Then some more paste can be spread in the area from the gold wires to the out regular wires (Figure 3.7).

After the sample set is heat treated for the silver paste to cure, it can be loaded into the DAC for experiments.

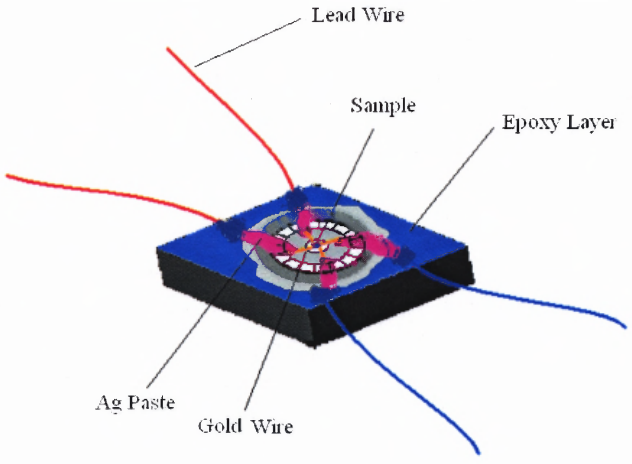

Figure 3.7 Sample mounted on gasket for high pressure resistivity measurement.

3.4.3.2 For Powder X-ray Diffraction. The powder x-ray diffraction requires the sample to be fine powder and the particles are randomly oriented. For conventional x-ray diffraction, this is not a problem. But for high pressure diffraction, the sample is very

small. The x-ray beam is also focused and/or cut with slit to the size of at most ~tens μm size. So the sample needs to be ground so that the particle size is much smaller than normal. Otherwise, the sample is prefer-oriented in the range of the beam size. The diffraction pattern is not uniform continuous circles (Figure 3.8), which induces large error in the later parameter extraction. Figure 3.9 is the result from sample well ground.

To do high pressure x-ray diffraction, after the sample is well ground to fine powder and then sift with a 400 mesh sieve, put some on the culet of a large diamond anvil without gasket, press the sample to a sheet, then cut the sheet to proper size. Now the sample is ready for loading.

3.4.4 Loading Samples

Eremets,[188] Dunstan and Spain[190,191] have described the sample loading procedure in detail. After making the sample-gasket set, the sample loading for resistivity measurements is easier than other experiments because the sample is fixed to the gasket. For the sample load, one problem may be from the ruby chips. Due to the small size, the ruby chips may float away when filling in liquid pressure medium. In most cases, this can be solved by first put a little silicon oil on the surface of the diamond anvil with needle tip and then place the ruby chips on the silicon oil layer.

3.4.5 Necessary Small Tools for High Pressure

For high pressure works, besides large and costly equipments, some small tools are very helpful. First, high precision tweezers with fine tips are necessary for handling small samples and fine wires. DUMOSTAR Biology and DUMOSTAR high precision micro tweezers work fine with samples of ~tens μm. Some micro needles with tips bended by 45° and 90° are useful too. Other needles can be made from sewing needles. The high precision carving knives and blades help to cut samples.

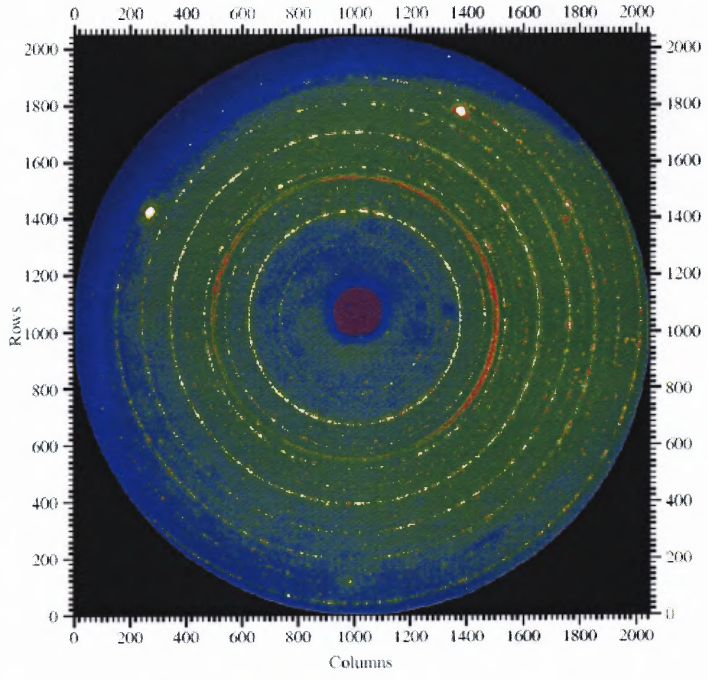

Figure 3.8 X-ray diffraction pattern from sample not randomly oriented.

Note: the pattern was taken with a CCD. The two big bright spots are the diffraction from diamond anvils.

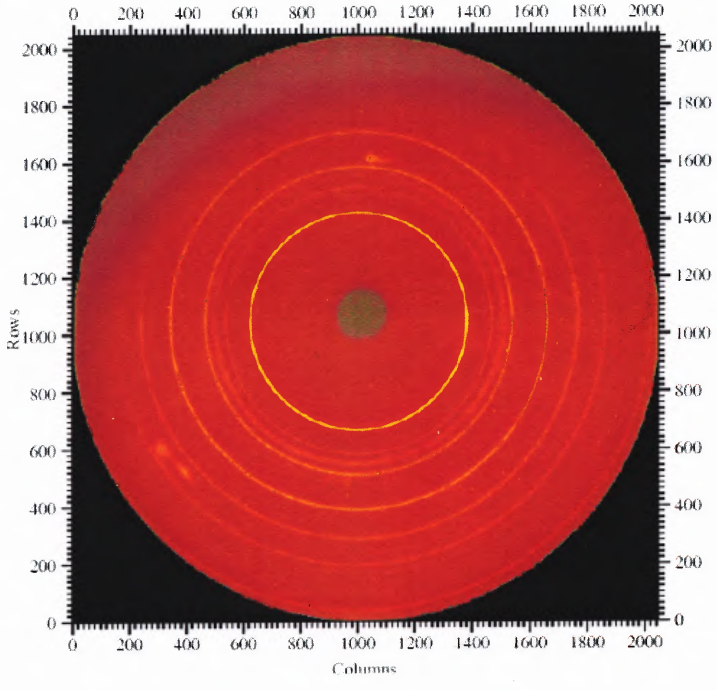

Figure 3.9 X-ray diffraction pattern from randomly oriented sample.

Note: the pattern was taken with a CCD. The big bright spots are the diffractions from diamond anvils.

3.5 High Pressure Experimental Methods and Instruments

3.5.1 High Pressure Resistance Measurements

3.5.1.1 Method. To measure the absolute resistivity of samples, generally, standard four-point method is used. However, under pressure in DAC, it is very difficult to do with samples of ~150 μm and usually with irregular shape. In this case, Van der Pauw four-point technique is feasible because sample dimension and spacing of contacts are not important. So the Van der Pauw four-point method with constant current was used to measure the sample resistivity. The details of the method can be found in ref. 232.

To measure resistivity accurately, the four contacts should be evenly distributed around the edges of sheet sample. The error of sample thickness should be as small as possible.

For the temperature dependence of resistivity under high pressure, at each pressure point, only the resistivity at one fixed temperature is measured, then a geometry factor is extracted. While scanning temperature, only the resistance between two contacts is measured. The resistivity at each temperature is calibrated by multiplying the resistance with the geometry factor. Certainly, this is under the hypothesis that geometry factor does not change with pressure and temperature. Actually, by considering the pressure and temperature effect on geometry factor and high pressure structure measurement results, it is found that the error is smaller than 5%.

The measurements of CMR resistivity involve both low and high resistance measurements at different pressures and temperatures (from room to liquid helium temperature). In the measurements, some errors need to be considered.

The first is contact resistance. The input impedance of the voltage meter used is $>10^9$ Ω, at least 100 times higher than sample resistance. Because four-point method was used, the contact resistance error can be eliminated.

The second error source is the thermoelectric EMFs. The thermoelectric voltages can seriously affect the low resistance measurement accuracy. Because the polarity of

thermoelectric voltage does not change with applied current at given temperature, it can be cancelled by reversing the current source. This is done by making two measurements with currents of opposite polarity, then dividing the difference of the two readings by 2:

$$V = \frac{|V_+ - V_-|}{2} \tag{3.4}$$

where V_+ and V_- are the voltage readings at positive and negative currents respectively.

To improve the accuracy, while sweeping temperature at a given pressure, at each point, 5 pairs of data were taken with both positive and negative bias currents while 20 readings of voltage were taken and averaged. Then the final readings are acquired by averaging the voltages from which the thermoelectric voltage has been eliminated. The method is summarized as the formula:

$$V = \frac{1}{5}\sum_{j=1}^{5}\left(\frac{1}{20}\sum_{i=1}^{20}V_+^{ij} - \frac{1}{20}\sum_{i=1}^{20}V_-^{ij}\right) \tag{3.5}$$

Because the resistivity is measured under pressure, there may be two error sources from pressure effect: pressure induced contact resistance change and piezoelectric effect. The pressure induced contact resistance change can be eliminated by the four-point resistivity measurement. To date, there is no report about the piezoelectric effect in CMR manganites. The temperature dependence of voltage between a pair of leads without applying current was measured at several pressures (Figure 3.10). In the pressure range measured, there seems no obvious piezoelectric effect. The non-zero reading in the figure is the background of instrument. The minimum signal is an order higher than the background. The differences between curves at different pressures were noticed. Nevertheless, it cannot be told if it is due to the piezoelectric effect. Moreover, because at every point, the voltage is measured by averaging the readings with reversed current, the voltage change with pressure is cancelled. The other reason that the piezoelectric effect is not considered is that the samples are polycrystalline.

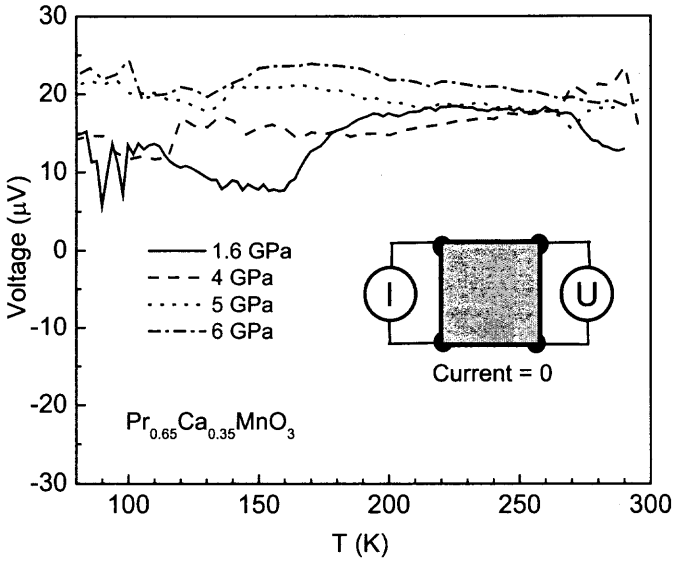

Figure 3.10 Piezoelectric effect of CMR.

3.5.1.2 Resistivity Measurement System. To do high pressure resistivity measurement with DAC, a system was built. It can be operated in temperature range from liquid helium to 325 K. The system includes a Janis cryostat in the temperature range from Liquid Helium to 325K, a Keithley 2400 source-meter, LakeShore 330 temperature controller. The temperature controlling and data logging are implemented with a software programmed in LabView. On the cryostat there are four optical windows. The diamond anvil cell is mounted on a holder and positioned so that laser can shine on the ruby chips through the windows to do in situ pressure measurements. The pressure at sample is acquired by measuring the ruby R1 line shifts at different temperatures and places around sample in DAC and then averaging the pressure calculated. The pressure accuracy, non-hydrostaticity and change with temperature are characterized by the variance.

3.5.2 High Pressure X-ray Diffraction Measurements

In high pressure x-ray diffraction (XRD), the x-ray beam must travel through the two diamond anvils about 0.5 cm. This cuts off x-rays below about 12–15 keV. For the conventional rotating anode x-ray generators, because of the heavy absorption of

diamonds, signal is extremely low. The x-ray energy that can be used is the Mo K-edge. But to get small beam, slit induces more intensity loss. So to get good data is difficult with a conventional source. The other problem with the conventional source is that the small exit aperture limits the angle range.

The problem with conventional source can be solved with synchrotron radiation source. The synchrotron radiation has continuous spectrum from IR to very hard x-ray region, is naturally collimated, polarized and has high brightness. In addition, the beam can be focused to ~μm or sub micrometer size that can be used to do micro beam x-ray diffraction to characterize the local information of materials. These outstanding properties make SR ideal for high pressure x-ray diffraction.

The simplest way for high pressure diffraction is that the focused x-ray beam goes through the diamond anvils and sample (Figure 3.11). The diffraction patterns are collected with a CCD or imagine plate.

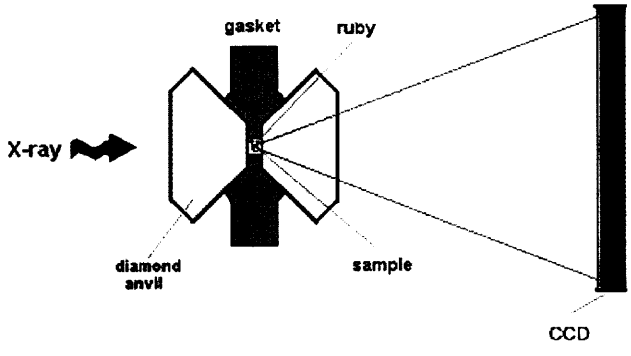

Figure 3.11 High pressure x-ray diffraction with DAC.

The pattern recorded with a CCD or an imagine plate can be converted to the 2θ *vs.* intensity format for post-processing. Data were fitted with Rietveld refinement method to get the atom positions, bond length and bond angle, in addition to lattice parameters. There is a whole bunch of softwares doing the Rietveld refinement with various powder diffraction data. The most popularly used one is GSAS, which can be acquired free from internet.

3.6 Samples

To systematically study the pressure effects on electronic, magnetic properties and structures of CMR material and the relations between pressure effects and doping system and doping concentration, several typical systems with different doping concentration and hence, different $<r_A>$ and local distortion were selected.

The first sample is $La_{0.60}Y_{0.07}Ca_{0.33}MnO_3$. It has a coincident metal-insulator and ferromagnetic-paramagnetic transition upon warming. The transition temperature is ~150 K that enables the observation of the magnetic and electronic properties changing as a function of pressure and temperature over a broad range.

The second set of samples is the $Pr_{1-x}Ca_xMnO_3$ (x = 0.25, 0.30, 0.35) doping system (Figure 1.7). The sample of x = 0.25 is insulating in the whole temperature range, there is a FM to PM transition at ~130 K. The x = 0.30 sample is at the boundary of transition from the FMI-PMI phase to the CAFI-AFI (CE-type)-COI-PMI phase with x increasing. It is insulating in the whole temperature range with T_{CO} ~220 K, T_N ~140 K, CE-type AFI to CAFI transition at ~110 K. The x = 0.35 sample is similar to the x = 0.30 sample with higher CO and CE-type AFI and lower CAFI transition temperature.

Another system studied is $Nd_{1-x}Sr_xMnO_3$ (x=0.45, 0.50) (Figure 1.7). The x = 0.45 sample is a double exchange sample. Because of its relative large $<r_A>$, the FMM to PMI transition temperature is ~280 K, much higher than that of $La_{0.60}Y_{0.07}Ca_{0.33}MnO_3$. In x = 0.50 sample, with temperature increasing, three phases appear: below ~155 K is charge order phase; between ~155 K and ~255 K is the FMM phase; above ~255 K is the PMI phase.

In the samples selected, most of the physics in the CMR materials, such as the PMI, FMM, FMI, FI, COI, AFI, CAFI, are included so that we can observe the pressure effects on various magnetic and electronic states and their correlations changing with pressure. In addition, $<r_A>$ of samples distributes in the range of currently studied CMR materials (Table 3.2). Because the bandwidth and distortion is correlated to $<r_A>$, the strength of

various electronic and magnetic states under pressure with different bandwidth and distortion can simultaneously be investigated.

Resistivity is very sensitivity to various phase transitions and electron-lattice interactions. Due to the electron, spin, and lattice interactions in manganites, the magnetic state changes are also reflected in resistivity. Therefore, the study will be performed primarily on high pressure resistivity measurements. High pressure x-ray diffraction will be performed to detect the structure evolution with pressure.

Table 3.2 Average A-Site Atom Size $\langle r_A \rangle$ of Samples

$Pr_{0.75}Ca_{0.25}MnO_3$	1.17925	$La_{0.60}Y_{0.07}Ca_{0.33}MnO_3$	1.20230
$Pr_{0.70}Ca_{0.30}MnO_3$	1.17930	$Nd_{0.55}Sr_{0.45}MnO_3$	1.22915
$Pr_{0.65}Ca_{0.35}MnO_3$	1.17935	$Nd_{0.50}Sr_{0.50}MnO_3$	1.23650

Note: the unit is in Å; $\langle r_A \rangle$ is calculated with the 9-coordinates data from ref. 107.

All samples were prepared by solid reaction method. The procedure is: first, related compounds are weighted according to stoichiometry of each sample. The powders are mixed and ground for one half to one hour. Then the powder is calcined in a furnace. After the first calcination, the powder is reground for another one half to one hour and then re-calcined. Generally, the powder is ground and calcined two or three times. Then the powder is pressed into pellets. The pellets are sintered. After this, the pellets are annealed and cooled to room temperature at the rate of 1°C/min. Then the samples can be cut, thinned, and polished for resistivity measurements or ground to a powder for x-ray measurements. These are the general steps of preparing samples. The details will be described later for each sample.

CHAPTER 4

ELECTRON TRANSPORT AND STRUCTURE OF $La_{0.60}Y_{0.07}Ca_{0.33}MnO_3$ UNDER PRESSURE

4.1 Introduction

In the $La_{1-x}Ca_xMnO_3$ system, when x is in the range of 0.2~0.5, there is a metal-insulator transition with increasing temperature, and the Curie temperature T_C coincides with the MIT temperature T_{MI}.[6,15,16,18,125,233,234] $La_{2/3}Ca_{1/3}MnO_3$ is a typical double exchange manganite. The transition is ~270 K. When substituting La^{3+} with smaller size Y^{3+} ion, T_C is greatly reduced to ~150 K with the Y fraction being 0.07, partly due to more induced distortion. With T_C decreasing, the magnetoresistance is increased to ~10000% in a 6 T magnetic field.[13]

Its magnetotransport properties suggest strong electron-lattice and spin-lattice coupling.[91] Under pressure up to ~0.8 GPa, T_C, T_{MI} and the linear thermal expansion coefficient peak coincide and are linear functions of pressure.[146] Classical mean-field analysis of magnetization data indicated that magnetic clusters with size of a few unit cells exist. These magnetic nano-clusters develop ferromagnetic moments to form local ferromagnetic cluster above macroscopic ferromagnetic ordering temperature.[137] The electrical transport is possibly correlated to the conduction electrons scattering at boundaries of these clusters.

The FMM to PMI transition of $La_{0.60}Y_{0.07}Ca_{0.33}MnO_3$ is sharp. The transition temperature lies in the middle range from liquid helium to room temperature. This enables the observation of shifts in T_{MI} over a broad range of pressures. Although this sample has been extensively studied, its properties under high pressure above 2 GPa were still unexplored.

In experiments covering pressure range 1 atm to ~7 GPa, We found that below P*~ 3.8 GPa, high pressure increases T_{MI} and suppresses resistivity. But above P*, T_{MI}

decreases and resistivity increases quickly with pressure. The resistivity in measured temperature range of liquid nitrogen to room temperature follows the same manner. This possibly suggests that high pressure causes a change in the crystal structure (local or long range). Hence, high-pressure x-ray diffraction measurements were performed to determine the structural evolution under high pressure. We found that at P* pressure induces a structural transformation within the MnO_6 octahedra to a highly Jahn-Teller distorted state. Above P*, with increasing pressure the MnO_6 octahedra continue to tilt.

4.2 Samples

The samples of $La_{0.60}Y_{0.07}Ca_{0.33}MnO_3$ were prepared by solid-state reaction. Stoichiometric amounts of La_2O_3, Y_2O_3, MnO_2, and $CaCO_3$ were mixed, ground and calcined. Multiple heating and grinding cycles were performed to ensure phase purity. Each grinding between heating cycles is approximately ~30 min. The detailed heating cycles are listed in Table 4.1. After the heating and grinding cycles, the powder is pressed into pellets and sintered at 900 °C for ~24 hours. The sintered pellets were broken, ground, pressed into pellets, sintered again and annealed in air at 1300 °C for 12 hrs.

The sample was characterized by x-ray diffraction, magnetization and resistivity measurements.

The x-ray diffraction pattern taken at room temperature showed that the samples are in a single crystallographic phase (Figure 4.1). The structure was refined to Pbnm symmetry using the Rietveld method. The refinement results, consistent to that published by other group,[91] are listed in Table 4.2.

The magnetization measurements are shown in Figure 4.2. The magnetic moment at 5 K in a 10 kOe magnetic field is $3.66\mu_B$ which compares well with the theoretical estimation of $3.67\mu_B$. The Curie temperature is defined as the edge, the maximum of the first order derivative of magnetization *vs.* temperature curve. The T_C extracted in this way

is 150 ± 2.5 K - consistent to the metal-insulator transition temperature T_{MI} (149.8 ± 1.0 K), the temperature at the resistivity peak. (We note also that magnetization measurements in a low field of 10 Oe yield a T_C value of 145 ± 2.5 K).

Table 4.1 Heating Cycles for Making $La_{0.60}Y_{0.07}Ca_{0.33}MnO_3$

Cycle	Heating Temperature	Heating Time
I	900 °C	21 hr
II	900 °C	24 hr
III	1000 °C	21 hr
	1100 °C	4.5 hr
IV	1000 °C	19 hr
	1100 °C	8.5 hr
V	1150 °C	22 hr

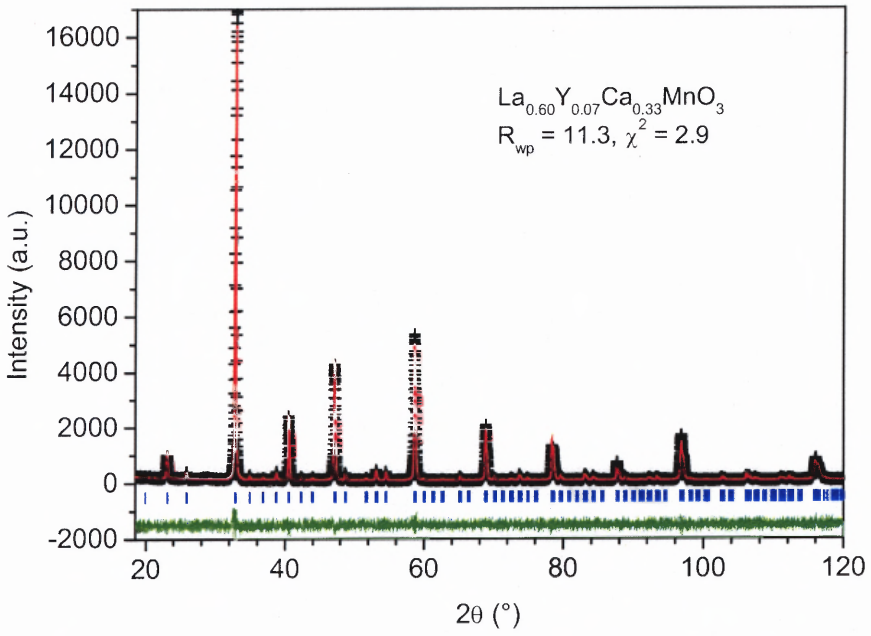

Figure 4.1 Refinement of XRD of $La_{0.60}Y_{0.07}Ca_{0.33}MnO_3$ at room temperature.

Table 4.2 Rietveld Refinement Results for $La_{0.60}Y_{0.07}Ca_{0.33}MnO_3$ at Room Temperature

La/Y/Ca	x	0.5034(4)	a	5.45810(6)
(0.6/0.07/0.33)	y	0.52181(9)	b	5.45149(7)
	x	0.4478(16)	c	7.69806(11)
O(1)	y	0.9872(10)	B_{av}	0.31(2)
	x	0.7282(22)	R_p	8.3
O(2)	y	0.2873(15)	R_{wp}	11.3
	z	0.0391(6)	χ^2	2.9

Note: x, y, z are fractional atomic positions; a, b, c are unit cell parameters; B_{av} is Debye-Waller factors; R_p and R_{wp} are unweighted and weighted reliability factors respectively; χ^2 is "goodness of fit". The fit errors are in the brackets following the numbers. The atoms are located at the Wyckoff positions: La/Y/Ca at 4c: (x, y, 1/4), Mn at 4b: (1/2, 0, 0), O(1) at 4c: (x, y, ¼), O(2) at 8d: (x, y, z).

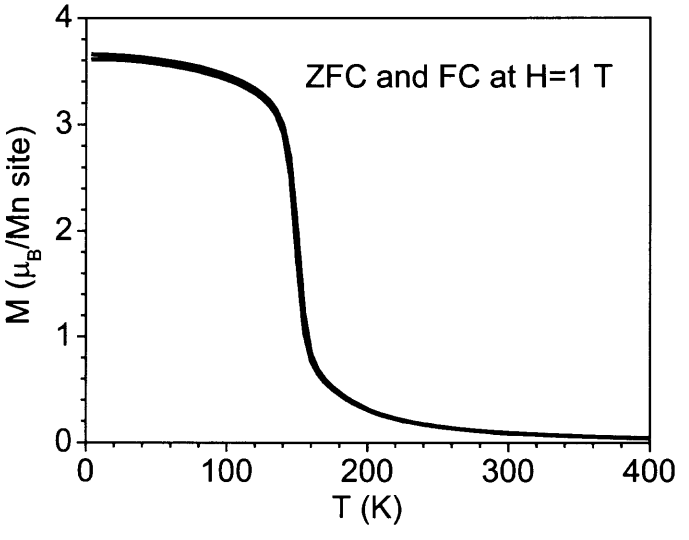

Figure 4.2 Magnetization measurements of $La_{0.60}Y_{0.07}Ca_{0.33}MnO_3$ at 1 T.

4.3 High Pressure Transport Measurements

The resistance of sample as a function of temperature, under pressures up to ~7 GPa is shown in Figure 4.3. Figure 4.4 (a) is the pressure dependence of T_{MI}. It is apparent that T_{MI} increases first, saturates and then quickly drops with increasing pressure. At ambient pressure, T_C and T_{MI} coincide. In the same material, it was reported that T_C and T_{MI} still coincide under pressure up to ~0.8 GPa.[146] In the parent compound $La_{0.67}Ca_{0.33}MnO_3$, T_C and T_{MI} coincide up to at least 1.6 GPa.[143] Results on the coincidence of T_C and T_{MI} beyond this pressure range was unawared of. However, it has been reported that the substitution of La atom with Gd and Y leads to a separation between T_C and T_{MI}.[235,236] Hence, in the higher pressure range this question is still open. Here, only shifts in T_{MI} will be discussed and the question of shifts in T_C at pressure above 1.6 GPa is left open for future work.

In Figure 4.4 (a), the data of T_{MI} *vs.* P is fitted with a third order polynomial. The dT_C/dP (or dT_{MI}/dP) near ambient pressure determined with it is 22 ± 4 K/GPa. It is consistent with the 26 ± 2 K/GPa value reported on the same material by Arnold *et al.*[146]

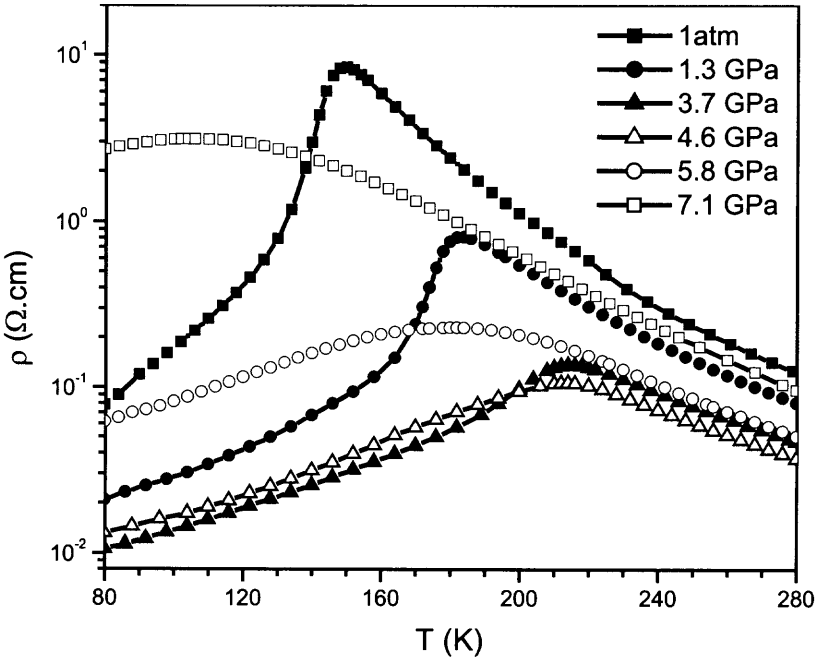

Figure 4.3 Temperature and pressure dependence of resistivity of $La_{0.60}Y_{0.07}Ca_{0.33}MnO_3$.

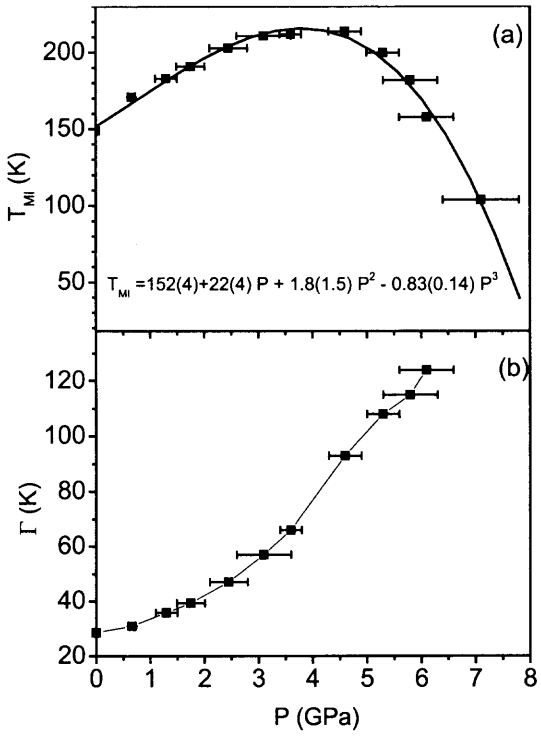

Figure 4.4 Pressure dependence of T_{MI} and peak width of $La_{0.60}Y_{0.07}Ca_{0.33}MnO_3$.

Note: (a) Pressure dependence of T_{MI}. The solid line is a 3rd order polynomial fit with the coefficient errors in brackets; (b) Pressure dependence of the peak width of the metal-insulator transition. The solid line is a guide to eyes.

Another noticeable feature about the resistivity data at different pressures is the peak width. The peak width is defined as full width at half maximum (FWHM). With pressure increase, the peak is dramatically broadened [Figure 4.4 (b)]. This may originate from non-hydrostatic pressure conditions. By placing multiple ruby chips in the DAC cell, we found that the pressure difference around sample increases with pressure which may imply that the pressure medium freezes more easily at higher pressure. Because the size of ruby chips is quite small (< 10 μm), the fluorescence doublet still separate very well except that the peaks are only slightly broadened. The observed largest difference of pressure around sample is ~0.5. The pressure was also found to decrease with temperature increase. The higher pressure, the larger this pressure changing is. The overall variations in pressure in sample space are indicated as error bars in the related figures. The variation of pressure around sample and with temperature does not explain

the peak broadening. Apparently, the main reason for peak broadening may be that the material is becoming insulating with pressure increase so that the peak is suppressed and disappears.

The conductivity in the measured temperature range changes in the same behavior as T_{MI}. The only difference is that resistivity in the metallic region changes faster than in paramagnetic insulating region (Figure 4.5). The T_C (and T_{MI}) of the parent compound $La_{0.7}Ca_{0.3}MnO_3$ is ~270 K. Under high pressure, the T_{MI} of $La_{0.60}Y_{0.07}Ca_{0.33}MnO_3$ does not reach 270 K but saturates far below at ~215 K and then quickly decreases with increasing pressure.

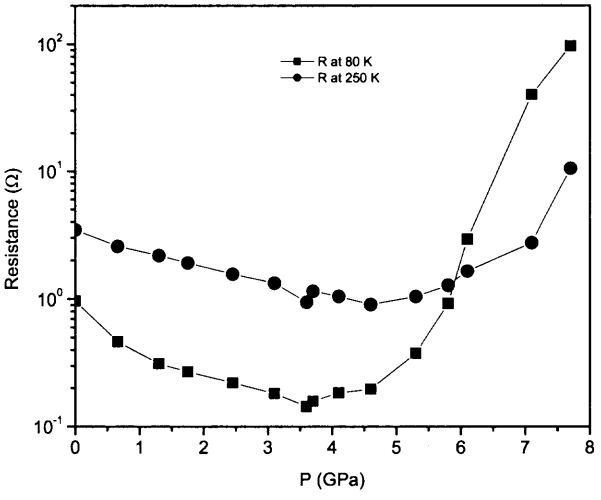

Figure 4.5 Pressure dependence of resistance in FMM phase (at 80 K) and in PMI phase (at 250 K).

It was reported that in a similar compound $La_{0.6}Y_{0.1}Ca_{0.3}MnO_3$ the resistivity in paramagnetic phase follows a variable range hopping model in which the resistivity behaves as in equation (1.15). With the resistivity at different pressures, the Arrhenius, adiabatic and nonadiabatic polaron models are compared in the paramagnetic phase (Figure 4.6). It is obvious that the measurements here are consistent with the VRH behavior. So the resistivity data under pressure were fitted with this model. It can be seen that pressure does not change this behavior (Figure 4.7).

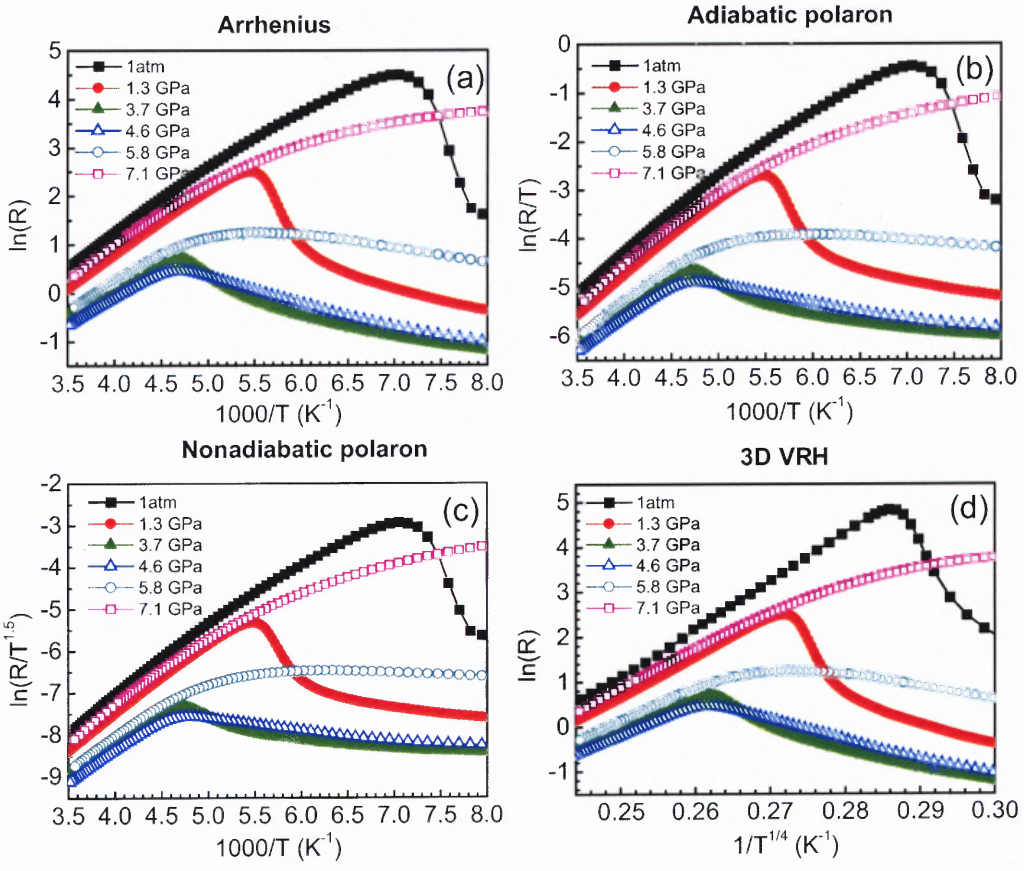

Figure 4.6 Resistivity fitting in Arrhenius (a); adiabatic polaron (b); nonadiabatic polaron (c); and 3D variable range hoping (d) models.

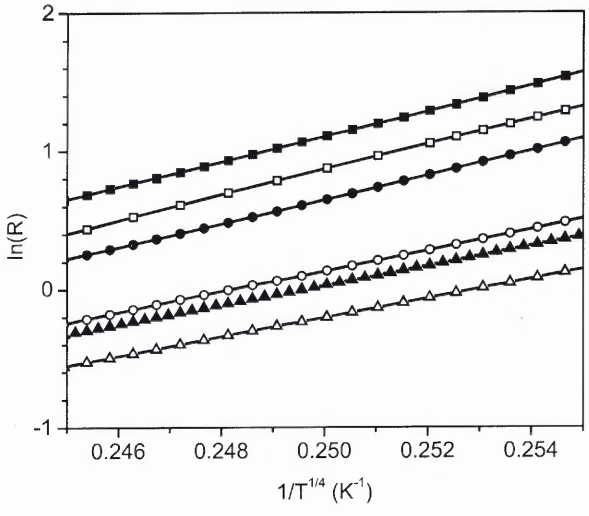

Figure 4.7 Fitting of resistance data with VRH magnetic localization model.

Note: the plots of data are in the paramagnetic insulating range far from the transition temperature.

Viret and co-workers[124,134,135] developed the magnetic localization theory from the VRH model to explain the resistivity dependence on temperature of CMR at x = 0.3 and suggest that the mechanism of MIT is localization associated with magnetic disorder. The magnetic localization length can be evaluated with equation (1.19). With f = 18,[124,134,135] reasonable localization length values were acquired with our data.

Based on this theory, the localization length ξ can be expressed as:

$$\xi^3 = \frac{120U_m(1-<\cos\theta_{ij}>)v}{kT_0 g} \tag{4.1}$$

where U_m (= $3J_H/2$) is the Hund's rule coupling strength; θ_{ij} is the angle between the two neighbor spins; v is the lattice volume per manganese ion; g is the probability that an unoccupied manganese orbital can actually accept an electron, which reflects the dynamic JT effect, only when the receiving site is not distorted or properly distorted can electron hopping happen. In the above equation, the localization length is the function of both the Mn-O-Mn bond angle and the dynamical Jahn-Teller distortion.

The localization length extracted according to this model is shown in (Figure 4.8). The maximum of localization length at ~P* is ~0.21 nm. This is the order of the Mn-O bond length. The corresponding hopping distance is ~1.35 nm which is several unit cells. It is noticeable that this is also the size of the magnetic clusters Sun *et al.*[137] reported.

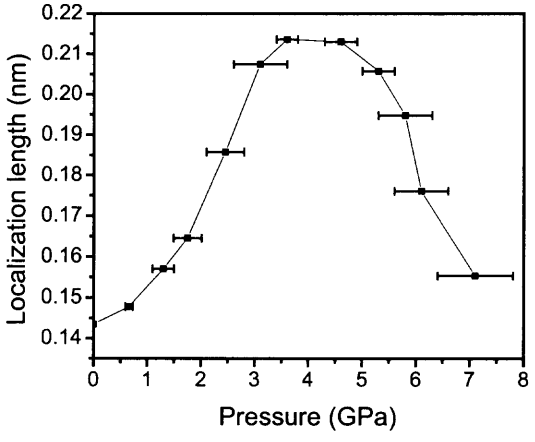

Figure 4.8 Localization length evaluated with the VRH model.

Note: the solid line is a guide to eye.

Polaron models are also extensively used to explain the transport behavior of manganites. It was reported that the variable range hopping of small polarons can also leads to $\ln(\rho) \propto T^{-1/4}$ behavior.[136] Kapusta *et al.*[237] suggested that the magnetic correlations in systems of $(La_{1-x}A_x)MnO_3$ (A = Ca, Sr) be possibly due to magnetic polarons. With temperature decrease there is a transition from small-polaron-dominated PMI regime to a large-polaron-dominated FMM regime.[106] Röder *et al.*[90] reported that above T_C, the small magnetopolaron due to the JT coupling, which involves about 4 lattice sites, comprises a localized charge surrounded by a spin cloud on nearest neighbors. Small angle neutron scattering measurements on $La_{2/3}Ca_{1/3}MnO_3$ found that the magnetic polarons have dimensions ~1.2 nm above T_C and that high magnetic fields enhance the correlation length significantly.[101]

Despite the difference between the models, magnetic localization and the polaron formation depend critically on the local structure. The distortion of local structure, such as static and dynamic Jahn-Teller distortion and/or rotation of MnO_6 octahedra, play an important role on the transport behavior.

4.4 High Pressure Structural Measurements

To understand the high-pressure resistivity results, high-pressure x-ray diffraction measurements were performed. The data were refined with Rietveld method based on the 1 atm Pbnm space group. The pressure dependence of unit cell volume is shown in Figure 4.9(a). In the measured pressure range, it is monotonically compressed. In Figure 4.9(b) and (c) are the Mn-O bond length and Mn-O-Mn bond angle pressure dependence, respectively. Below ~2 GPa, all three Mn-O bonds are compressed and the bond angles have no obvious change. This may explain why the T_{MI} and resistivity behave according to DE theory: pressure compresses the Mn-O bonds to increase the Mn^{3+} e_g band and O^{2-} 2p band overlap, enhancing the hoping integral. From ~2 to ~3 GPa, there is a local

structure transformation similar to that in $La_{0.75}Ca_{0.25}MnO_3$.[162] The splitting of the two in-plane Mn-O2 bonds increases. The Mn-O1-Mn bond angle increases by about ~20° while the Mn-O2-Mn bond angle seems only decrease slightly. In the meantime, the coherent Jahn-Teller distortion, defined as the deviation of Mn-O bonds from average

$$\delta_{JT}=\sqrt{\frac{1}{N}\sum(R_{Mn\text{-}O}-\langle R_{Mn\text{-}O}\rangle)^2} \tag{4.2}$$

increases abruptly [Figure 4.9(d)]. Meneghini *et al.*[162] suggested a transition to a coherent local and/or dynamical Jahn-Teller distortion. This can partly explain why the T_C increase and resistivity decrease are halted at high pressure. With enhanced JTD coherence, the charge carriers are more localized and this produces a resistivity increase.

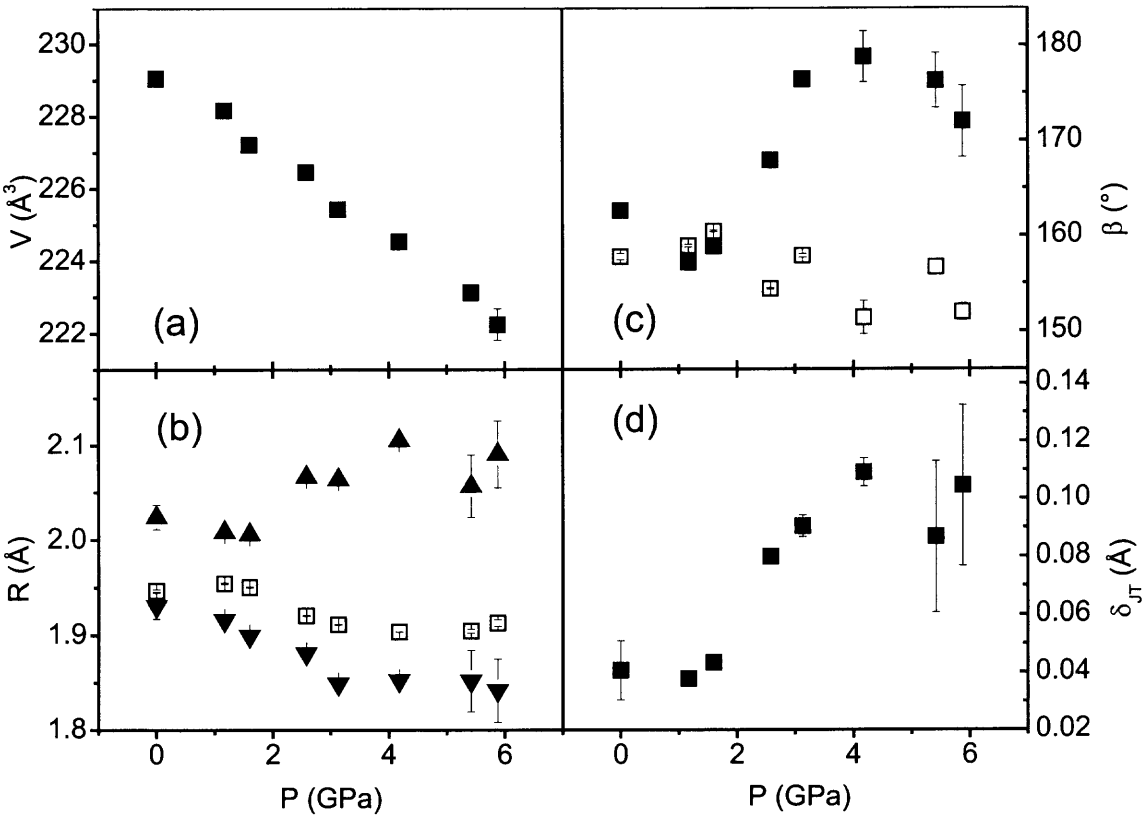

Figure 4.9 Pressure dependence of structure parameters at room temperature.

Note: (a) unit cell volume; (b) "ab-plane" Mn-O2 bond length (up and down solid triangles) and "c-axis" Mn-O1 bond length (empty squares); (c) "ab-plane" and "c-axis" Mn-O-Mn bond angles (empty and solid squares, respectively); (d) coherent Jahn-Teller parameter.

However, it is noticed that above P*, the coherence of the Jahn-Teller distortion and bond length only changes slightly with pressure. This is in contrast to the strong pressure dependence of T_{MI}, the resistivity and localization length at high pressures. From the structural parameters, it seems that only the Mn-O1-Mn bond angle, which characterizes the tilting of the MnO_6 octahedra, changes with pressure above P*. With the MnO_6 octahedra more tilted under pressure, the overlap of O^{2-} 2p orbital and e_g $d_{3z^2-r^2}$ orbital decreases, and hence, the charge carriers are more localized which can be observed in the localization length evolution as a function of pressure (Figure 4.8).

It is noticed that the pressure dependence of T_{MI} above P* is similar to that of the Yttrium doping $La_{1-x-y}Y_yCa_xMnO_3$ system, in which with Y concentration increase T_{MI} decreases and resistivity below T_{MI} increases monotonically.[238,239,240] This is ascribed to the MnO_6 octahedra buckling. In this system, ferromagnetically correlated clusters or magnetic polarons exist in the paramagnetic insulating phase and applied external magnetic field and spin exchange interaction can affect the localization or magnetic polaron size.[239] Resistance measurements under pressure in magnetic field may help to verify this picture. By comparing these measurements with the pressure dependence of localization length, one could conclude that with the local structure transformation, the spin state also is changed.

4.5 Summary

High-pressure effects on the resistivity and structure of the CMR material $La_{0.60}Y_{0.07}Ca_{0.33}MnO_3$ have been studied in the pressure range of 1 atm to ~7 GPa. It was found that pressure enhances the ferromagnetic metallic phase and suppresses the resistivity in the measured temperature range below ~3.8 GPa. Above ~3.8 GPa, the resistivity increases and the low temperature ferromagnetic metallic state is suppressed with pressure increase. Structural measurements at room temperature indicate that a

structural transformation occurs at ~3.8 GPa consisting of a distortion of the MnO_6 octahedra. Above ~3.8 GPa, the buckling of MnO_6 octahedra increases with pressure increase. Based on model fits, the author suggests that the structural changes under pressure leads to the localization length or the magnetic cluster (magnetic polaron) size increase at low pressure and decrease at pressures above ~3.8 GPa.

CHAPTER 5

ELECTRON TRANSPORT AND STRUCTURE OF $Pr_{1-x}Ca_xMnO_3$ UNDER PRESSURE

5.1 Introduction

In $Pr_{1-x}Ca_xMnO_3$ (PCMO), the tolerance factor is small. Hence, the transfer integral is rather small in the whole doping range. The e_g electrons are localized and the CO phase is stabilized in a large doping range.

In low doping range ($0.15 \leq x < 0.3$) and at low temperatures, $Pr_{1-x}Ca_xMnO_3$ is a ferromagnetic insulator. It is believed to exhibit an orbitally ordered ground state analogous to that observed in $LaMnO_3$. The Mn e_g electrons are hybridized with the oxygen 2p orbitals, and participate in a cooperative Jahn-Teller distortion of MnO_6 octahedra. This leads to $(3x^2 - r^2)/(3y^2 - r^2)$-type orbital order of the e_g electrons in ab-plane with the oxygen atoms displaced along the direction of e_g orbital extension. The excess Mn^{4+} ions are disordered and no charge ordering state is reported in this range.

In range of $0.3 \leq x \leq 0.7$, the compounds are antiferromagnetic insulating at low temperatures and the charges and orbitals are ordered. The charge ordering state is rather sensitive to external fields and radiation. Application of magnetic fields,[241] high electric fields,[242] irradiation with x-rays[243,244] or visible light[245]can all destroy the charge ordering and lead to a conducting state.

In magnetic field induced insulator-to-metal transition, the CO insulating state melts. Correspondingly, the magnetic state changes from PM or AFM to FM. The robustness of the charge ordering state correlates to doping concentration. [32,246,247,248]

In the photon induced COI state to metallic transition, the transition is accompanied by a dramatic change in magnetic properties and lattice structure: from canted AFM COI to FMM state.[249] The photocurrent is a highly nonlinear function of applied electric field and of light intensity.[245] Ogawa *et al.*[250] suggested that the photon induced metallic state

is maintained by the injected current while the role of photons is to overcome the potential barrier between COI state and metallic state to melt the COI state and cause transition. Fiebig *et al.*[251,252] showed that this transition contains two stages: in the first one, charge carriers are excited by photons, the local electronic structure is reorganized from COI to metallic phase so that the CO state melts and meta-stable domains form; in the second stage, the barrier between the metallic domains is overcome by electric field, resulting in a continuous conducting path that remains stable as long as the current is maintained.

In compounds with CO state, lattice is strongly coupled to spin and charge.[253] While charges are ordered, local distortion changes from dynamic Jahn-Teller distortion to a collective static distortion[253] and the MnO_6 octahedra buckle up.[254]

Under pressure, because of the bandwidth W increasing, CO state can be destroyed and metallic state is induced. Moritomo *et al.*[144] reported that pressure up to 0.8 GPa suppresses the CO of compound x = 0.35, 0.4, 0.5 and dT_{CO}/dP increases with x. In x = 0.3 compound, pressure above 0.5 GPa induces a metallic transition which is assigned to COI to FMM transition. Magnetic field was found almost equivalent to pressure up to 1.5 GPa and the effect of magnetic field can be scaled to pressure. The CO state is more robust when x is near to the commensurate value 0.5, so in x = 0.35 compound, the insulator-metal transition was not found under pressure up to 1.6 GPa.

By applying pressure to higher range, the magnetic, electronic, and structure of the PCMO system have been found greatly affected. In this range, pressure effects are far more complicated than in low pressure range (<~2 GPa). In this chapter, we will talk about these changes in the x = 0.25, 0.30, 0.35 compounds.

5.2 Samples

The samples were prepared by solid-state reaction. Stoichiometric amounts of Pr_6O_{11}, MnO_2, and $CaCO_3$ were mixed, ground and calcined at 1100 °C for 70 hours. Then the powder was reground and calcined at 1200 °C for 30 hours. The powder was pressed into pellets and the pellets were sintered at 1350 °C for 40 hours. Last, the pellets were annealed by increasing temperature to 1350 °C and holding for 10 hours and slowly cooling down to room temperature at 1 °C /min.

The x-ray diffraction pattern taken at room temperature showed that the samples are in a single crystallographic phase (Figure 5.1, Figure 5.2, Figure 5.3). The structure was refined to Pbnm symmetry using Rietveld method. The refinement results are listed in Table 5.1 and Table 5.2. All samples have O' -type orthorhombic structure with $(b > a > \frac{c}{\sqrt{2}})$.

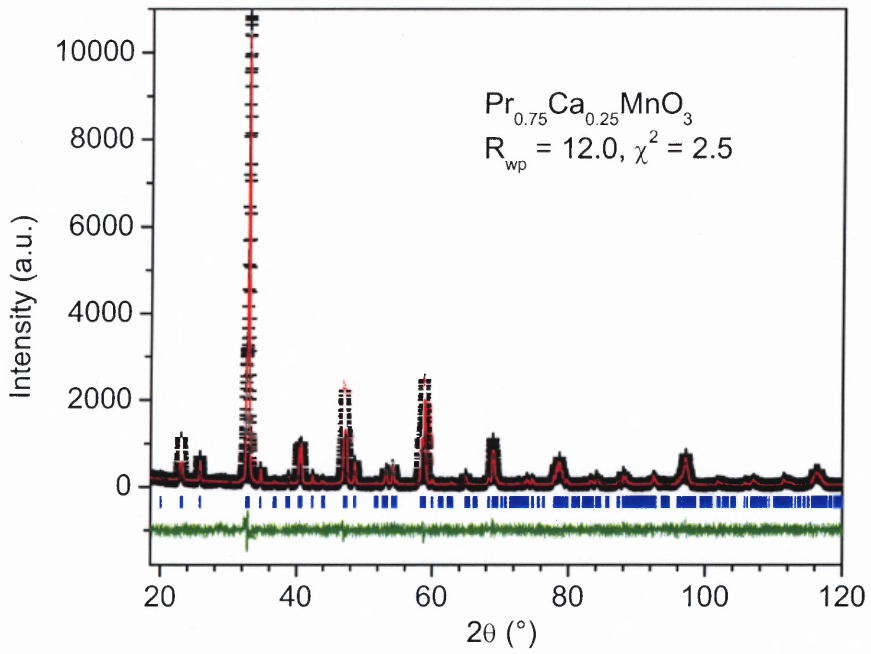

Figure 5.1 Rietveld refinement of XRD of $Pr_{0.75}Ca_{0.25}MnO_3$ at room temperature.

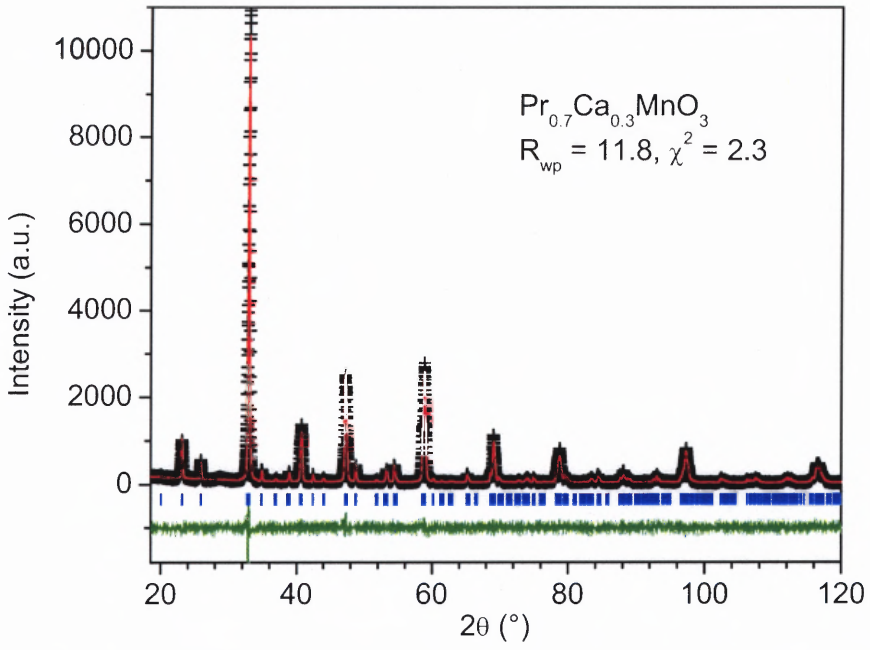

Figure 5.2 Rietveld refinement of XRD of $Pr_{0.7}Ca_{0.3}MnO_3$ at room temperature.

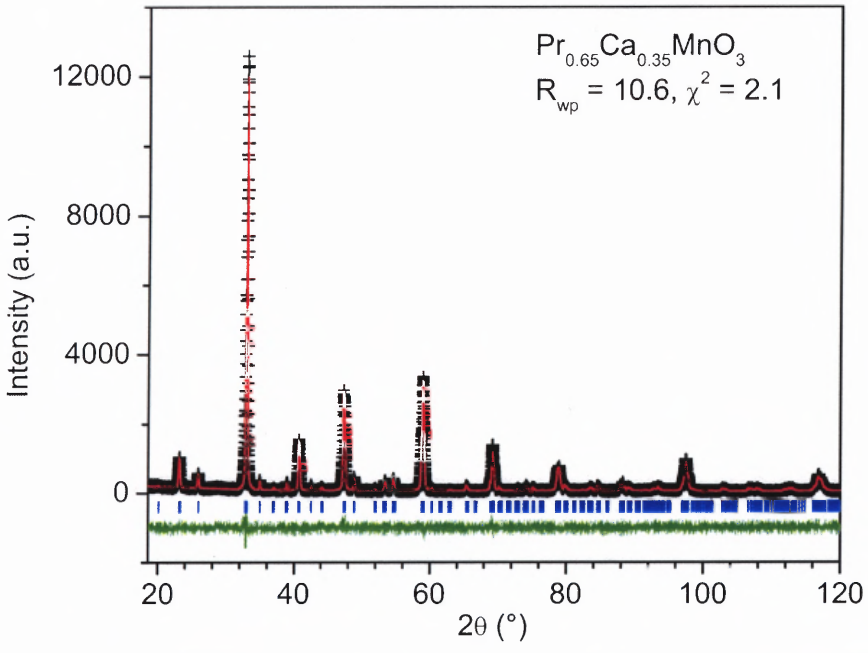

Figure 5.3 Rietveld refinement of XRD of $Pr_{0.65}Ca_{0.35}MnO_3$ at room temperature.

Table 5.1 Rietveld Refinement Results for $Pr_{1-x}Ca_xMnO_3$ at Room Temperature

Doping (x)		$Pr_{0.75}Ca_{0.25}MnO_3$	$Pr_{0.7}Ca_{0.3}MnO_3$	$Pr_{0.65}Ca_{0.35}MnO_3$
Unit Cell	a (Å)	5.43720(1)	5.43001(9)	5.42396(8)
	b (Å)	5.49561(1)	5.46757(7)	5.45147(7)
	c (Å)	7.68490(2)	7.67506(14)	7.66353(13)
Pr/Ca	x	0.99270(3)	0.9938(3)	0.9945(4)
	y	0.03591(1)	0.03349(9)	0.03175(9)
O(1)	x	0.4239(2)	0.4342(13)	0.440(1)
	y	0.9887(1)	0.9847(8)	0.9905(8)
O(2)	x	0.7164(1)	0.7149(10)	0.708(1)
	y	0.3014(1)	0.2954(9)	0.286(1)
	z	0.03776(7)	0.0380(6)	0.0350(6)

Note: x, y, z are the fractional atomic positions; a, b, c are the unit cell parameters; the fit errors are in the brackets following the numbers. The atoms are located at the Wyckoff positions: Pr/Ca at 4c: (x, y, 1/4), Mn at 4b: (1/2, 0, 0), O(1) at 4c: (x, y, 1/4), O(2) at 8d: (x, y, z).

Table 5.2 Local Atomic Structure of $Pr_{1-x}Ca_xMnO_3$ at Room Temperature

Doping (x)		$Pr_{0.75}Ca_{0.25}MnO_3$	$Pr_{0.7}Ca_{0.3}MnO_3$	$Pr_{0.65}Ca_{0.35}MnO_3$
Bond Length	Mn-O1 (Å)	1.957(2)	1.954(1)	1.944(1)
	Mn-O2 (Å)	2.0440(7)	2.014(6)	1.985(7)
	Mn-O2 (Å)	1.918(6)	1.932(6)	1.942(7)
Bond Angle	Mn-O1-Mn	157.9(5)	158.4(4)	160.4(4)
	Mn-O2-Mn	154.6(3)	155.1(3)	156.4(3)
Jahn-Teller distortion		0.053(2)	0.035(5)	0.020(5)

The magnetization measurements are shown in Figure 5.4. The moment of the x = 0.25 compound at 5 K in a 10 kOe magnetic field is 3.44μ_B (the Mn site theoretical value is 3.75μ_B), indicating a ferromagnetic state at low temperature. T_C (135 ± 2.5 K) is consistent to the results in Figure 1.7. For the x = 0.30 compound, moment at 5 K in a 1 T magnetic field is 2.1μ_B, consistent to the result published with single crystal.[254] For the x = 0.35 compound, the magnetic moment is consistent to other measurements.[255] T_{CO} is ~240 K, consistent to that in Figure 1.7. The magnetization is also similar to that reported in the compound with a similar doping concentration.[253]

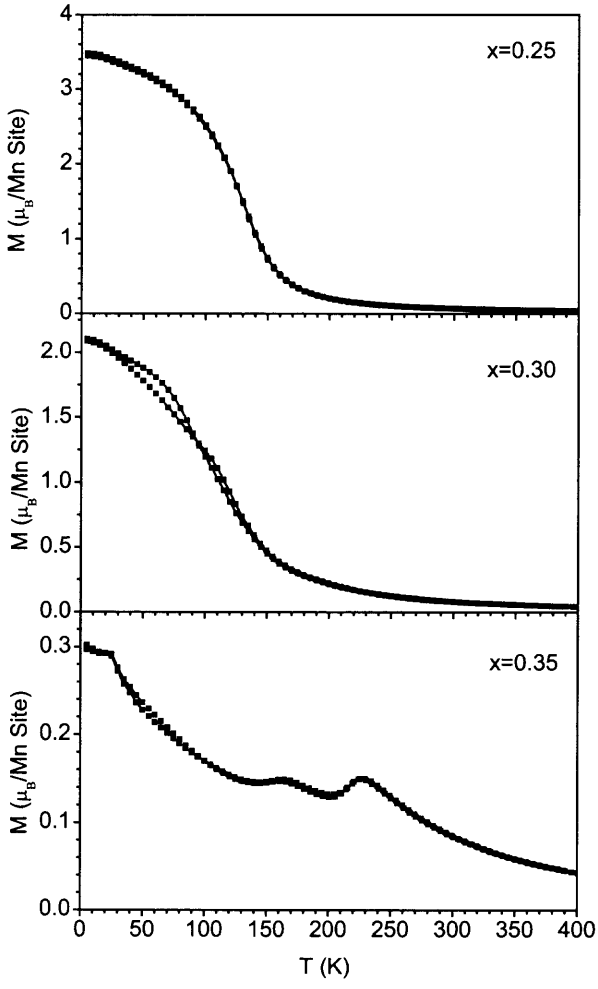

Figure 5.4 Magnetization measurements of $Pr_{1-x}Ca_xMnO_3$ (x = 0.25, 0.30, 0.35) in a magnetic field of 10 kOe.

Note: both ZFC and FC curve are shown.

5.3 Electron Transport and Structure of $Pr_{0.75}Ca_{0.25}MnO_3$ under Pressure

5.3.1 Electron Transport

Figure 5.5 is the resistivity at different pressures. With pressure increasing, the low temperature insulating state is suppressed and a metal-insulator transition is induced. The transition temperature increases with pressure. When pressure is higher than a certain point, the low temperature state does not become more metallic, but insulating. The transition temperature decreases simultaneously. The resistivity in the paramagnetic and ferromagnetic phase is shown in Figure 5.6. Apparently, the resistivity follows the same manor as the transition temperature.

In PCMO system, from x = 0.1 to 0.4, the resistivity displays p-type semiconducting behavior, $\rho = \rho_0 \exp(E_g / k_B T)$, with the activation energies (E_g) being slightly above 100 meV at room temperature.[256] The activation energy can be acquired by calculating $d\ln(\rho)/d(k_B T)^{-1}$ with resistivity as a function of temperature.

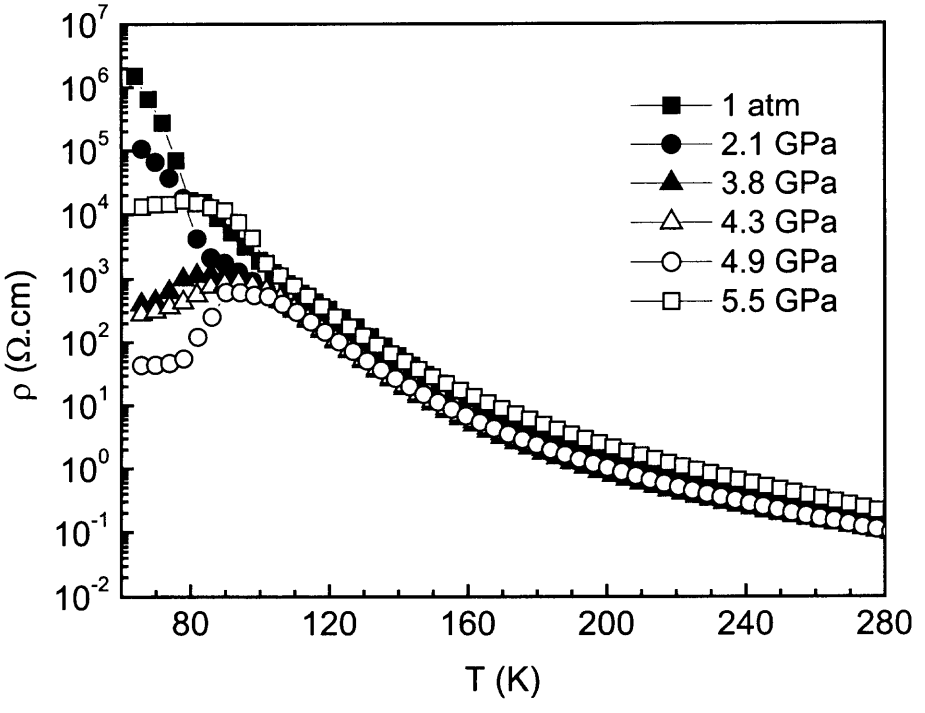

Figure 5.5 Resistivity of $Pr_{0.75}Ca_{0.25}MnO_3$ as a function of temperature under pressure.

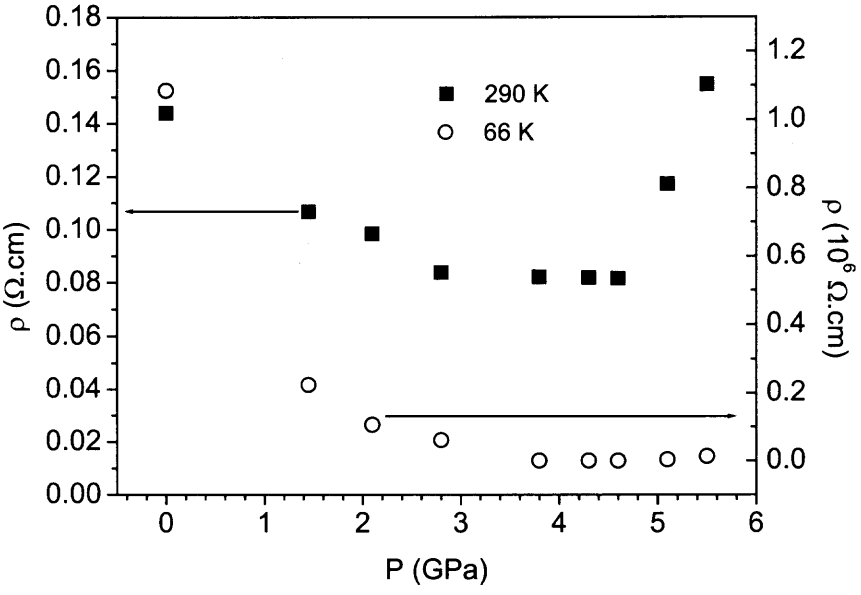

Figure 5.6 Resistivity of $Pr_{0.75}Ca_{0.25}MnO_3$ in low and high temperature phases as a function of pressure.

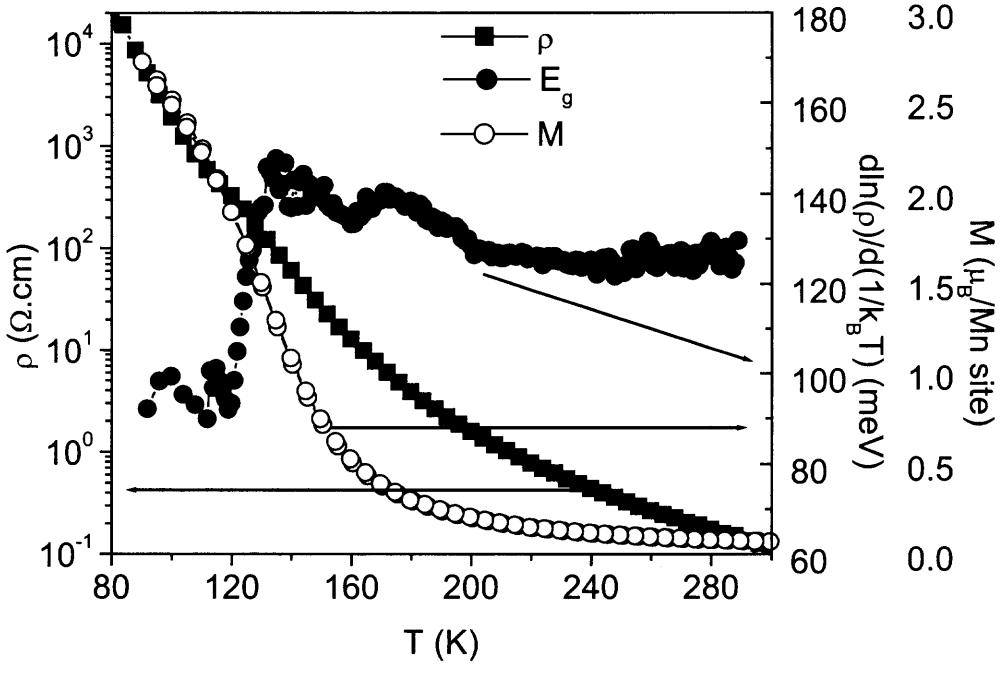

Figure 5.7 Resistivity, magnetization and activation energy of $Pr_{0.75}Ca_{0.25}MnO_3$ at ambient pressure.

Figure 5.7 is the resistivity, magnetization, and activation energy E_g at ambient pressure as a function of temperature. E_g in the paramagnetic phase is ~125 meV. At ~200 K, E_g increases upon cooling, indicating a new state. At present, there is no report about this state. Compared with the other two doping samples (x = 0.30, 0.35), it seems to correlate to CO. The CO state was not reported in this sample before. Considering the commensurate doping level 1/4, it is reasonable to ascribe this activation energy rising to charge ordering.

Another salient feature on the E_g *vs.* temperature curve is the fast decrease of E_g from ~140 meV to ~80 meV in the temperature range of 120~140 K. By comparison with the magnetization, this E_g change is correlated to the ferromagnetic transition. So in this compound, through resistivity measurement, magnetic transition can be observed simultaneously. Below the FM transition, because of the very narrow bandwidth, the material is still insulating but with a smaller energy gap than in paramagnetic phase.

By comparing the resistivity, magnetization, and activation energy plots in Figure 5.7, we can define the point where E_g changes fastest with temperature as the magnetic transition temperature T_C. The transition temperature extracted in this way is displayed in Figure 5.8 together with the MIT temperature T_{MI}. In this compound, the magnetic transition and electronic transition are decoupled. Below ~4 GPa, with pressure increasing, the magnetic transition temperature T_C decreases while the electronic transition temperature T_{MI} increases. This indicates that the conducting mechanism in the low temperature range is not DE and some competing mechanism takes effect.

In thin films, it was found that the MIT and the magnetic transition are decoupled,[257,258] which may be ascribed to the strong disorder at T_C. The disorder is overcome by magnetization increase while cooling, inducing a metallic state.[257] The T_{MI} and T_C decoupling also exists in bulk materials $Pr_{0.7}Ba_{0.3}MnO_3$,[55] in which it is ascribed to competition between DE and superexchange between neighboring Mn-Mn spins.

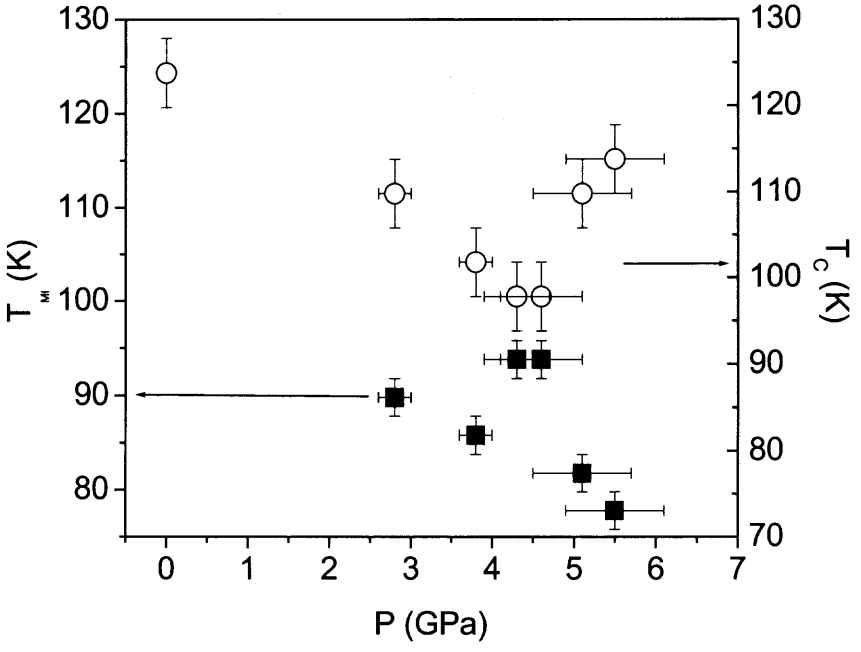

Figure 5.8 Metal-insulator transition and Curie temperature of $Pr_{0.7}Ca_{0.3}MnO_3$ *vs.* pressure.

The strength of superexchange is a function of bandwidth W. In low pressure range, because of the large lattice distortion, W is small, superexchange may dominate, hence, the material is insulating. With pressure increase, due to the local distortion suppression, W increases, correspondingly, the insulating state is suppressed, showing metallic state. The superexchange between two neighboring Mn^{3+} can either be ferromagnetic or antiferromagnetic depending on the Mn-Mn distance.[48] With pressure increase, the Mn-Mn distance monotonically decreases, the ferromagnetic superexchange interaction between the Mn^{3+} cations is weakened so that T_C decreases. On one hand, pressure suppresses the local disorder to enhance the metallic state; on the other hand, the Mn-Mn distance decrease leads to T_C decreasing. However, this is only the case below ~4 GPa, above this pressure, T_C increases with pressure. So there must be other factors dominating.

When pressure is above ~4.5 GPa, the trends of both the magnetic and electronic transition temperature changes with pressure are reversed.

E_g *vs.* T plots at several pressures are shown in Figure 5.9. With pressure increase, the E_g increase upon cooling is suppressed, indicating that the charge ordering state is suppressed. While the CO being suppressed, E_g becomes temperature dependent in the paramagnetic phase in high pressure range. At high pressures, upon warm up, E_g also increases. With pressure increase, this dependency becomes stronger. Because E_g characterizes the split of the two e_g orbitals which is due to the Jahn-Teller distortion, the pressure and temperature dependence of E_g may suggest that the Jahn-Teller distortion is enhanced in high pressure range.

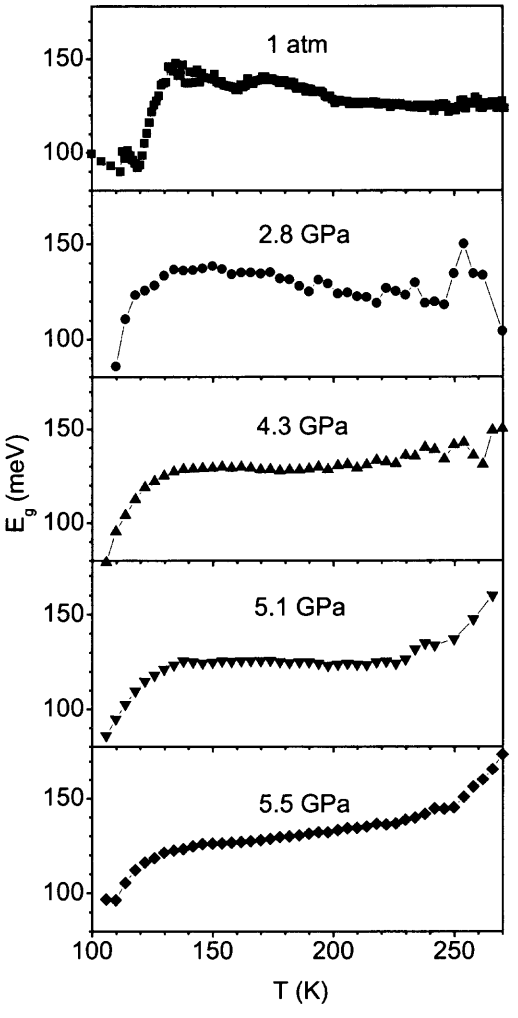

Figure 5.9 Activation energy of $Pr_{0.75}Ca_{0.25}MnO_3$ under pressure.

5.3.2 Structure at Room Temperature

The raw data were refined with the Rietveld method. The local atomic structure data calculated from the refined results are shown in Figure 5.10. In Figure 5.10(a) is the unit cell volume. Figure 5.10(b) is the bond length. In the measured pressure range, the difference of the Mn-O bond length at ~1.5-2 GPa is the largest, above that, the difference decreases with pressure increasing, indicating the Jahn-Teller distortion is reduced. It is evident that there is no abrupt change of the electronic properties: metal-insulator transition, resistivity and activation energy, at ~1.5-2 GPa. Figure 5.10(c) is the Mn-O-Mn bond angle. With pressure increasing, the in-plane bond angle Mn-O2-Mn seems to increase monotonically slightly; the bond angle along the c-axis, Mn-O1-Mn, decreases quickly above~1.5 GPa. The competition between in-plane and c-axis bond angles may lead to a maximum average bond angle at ~3-4 GPa. To describe the unit cell distortion from the cubic case, orthorhombic strains are defined,[162] in which strain in ab-plane is:

$$Os_{\parallel} = 2\frac{a-b}{a+b} \tag{5.1}$$

along c-axis is:

$$Os_{\perp} = 2\frac{a+b-c\sqrt{2}}{a+b+c\sqrt{2}} \tag{5.2}$$

$Os_{\parallel}$ and $Os_{\perp}$ describe the deviation of the structure from the ideal cubic structure, in which both $Os_{\parallel}$ and $Os_{\perp}$ are 0. Figure 5.10(d) is the orthorhombic strains in ab-plane and along c-axis. With the present data, both the ab-plane and c-axis orthorhombic strain decrease with pressure, indicating the structure becoming more cubic under pressure.

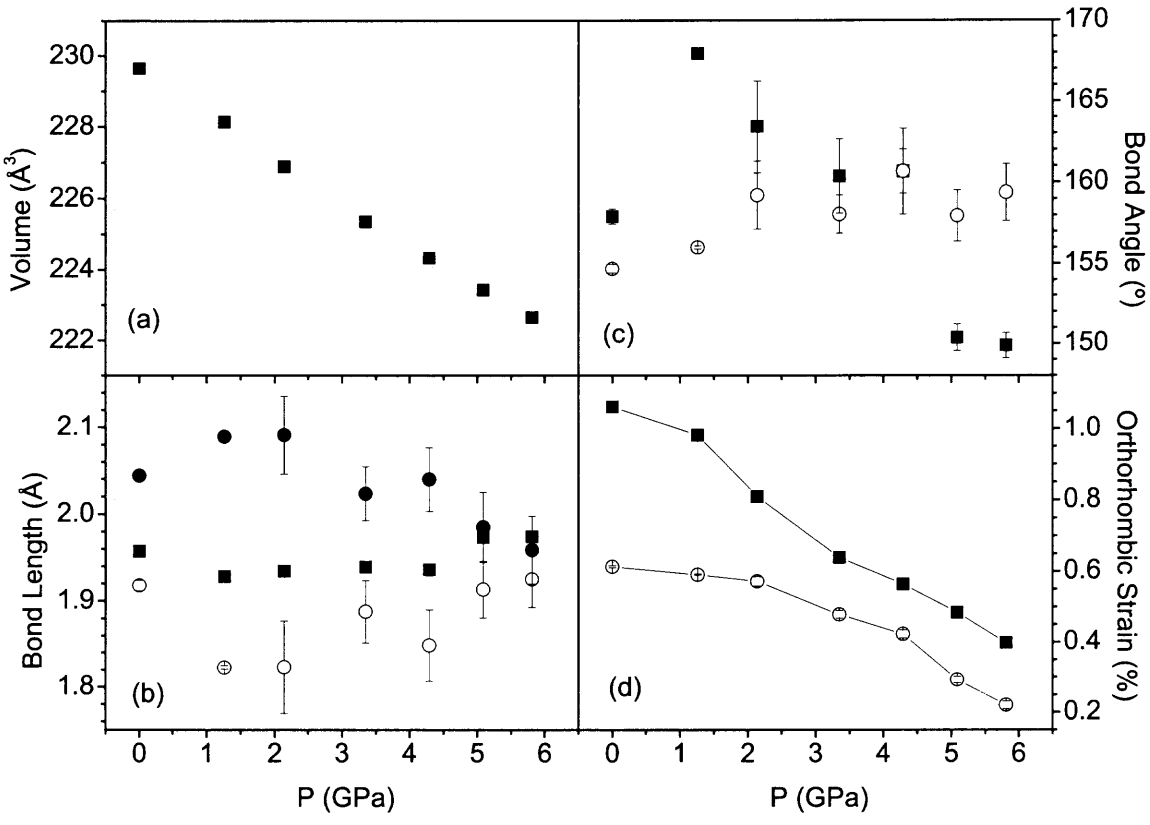

Figure 5.10 Structure of $Pr_{0.75}Ca_{0.25}MnO_3$ under pressure at room temperature.

Note: (a) unit cell volume; (b) Mn-O1 (solid square) and Mn-O2 (solid and open circles) bond lengths; (c) Mn-O1-Mn (solid square) and Mn-O2-Mn (open circle) bond angles; (d) ab-plane (solid square) and c-axis (open circle) orthorhombic strains

5.3.3 Discussion and Summary

Considering the structure data, it seems that the bond angle should to be responsible for the behavior of resistivity (Figure 5.6), the metal-insulator transition (Figure 5.8) and the activation energy (Figure 5.9) at room temperature. Below ~4 GPa, because of the average Mn-O-Mn bond angle increase, the bandwidth is increased so that the conductivity and T_{MI} increase correspondingly, while the activation energy is also decreased. Above ~4 GPa, because of the average bond angle decreasing, the behavior of resistivity, T_{MI} and activation energy is also reversed.

It should be noted that the Mn-O bond length behavior that the deviation decreases

on pressure increasing above ~1 GPa. This contradicts to the activation energy increasing in high pressure range which indicates a Jahn-Teller distortion enhancement. In addition, with pressure increase, the orthorhombic strains are also reduced. Upon the structure changes in high pressure range, it seems that the sample should become more metallic. However, in the high pressure range, the sample becomes insulating instead, the T_{MI} decreases and E_g increases. From the temperature dependence of E_g in high pressure range, it is reasonable to assume that the dynamic distortion dominate and pressure enhances the dynamic distortion. We note that the frequency of dynamic distortion is in the optical band while x-ray used for the diffraction is much higher so that the static and dynamic distortions cannot be resolved. Other kind of measurement, such as high pressure Raman scattering measurement, may settle this question.

It is reported that in another system $La_{1-x}Sr_xMnO_3$, ($0.1 \leq x \leq 0.15$) with a ground ferromagnetic insulating state, the magnetic transition from CAF phase to FMI phase upon cooling is strongly coupled to a structural transition from a Jahn-Teller distorted O' phase to a pseudocubic orthorhombic O^* phase.[56] This is ascribed to orbital ordering due to the interplay of superexchange interactions and Jahn-Teller distortions. The antiferromagnetic-type orbital ordering in the pseudocubic phase can induce an enhancement of the ferromagnetic superexchange interaction, so that magnetic field can lead to a phase transition from ferromagnetic metal phase to ferromagnetic insulator phase.[57]

In the $Pr_{0.75}Ca_{0.25}MnO_3$, with pressure increase, the lattice becoming more cubic, and simultaneously the JTD is reduced. This possibly enhances the orbital ordering and hence, the ferromagnetic insulating state as in $La_{1-x}Sr_xMnO_3$. This is what observed in Figure 5.8 that T_C and T_{MI} change reversely.

5.4 Electron Transport and Structure of $Pr_{0.7}Ca_{0.3}MnO_3$ under Pressure

5.4.1 Electron Transport

Figure 5.11 gives the temperature dependence of resistivity at different pressures. At ambient pressure, the material is insulating in the whole temperature range. As reported, at a pressure above 0.5 GPa, an insulator to metal transition is induced, which is ascribed to a charge ordering insulator to ferromagnetic metal transition.[27,144] With pressure increase, the transition temperature T_{MI} is continuously shifted to higher temperature and resistivity is suppressed. In the pressure range 3~4 GPa, this trend saturates. At higher pressure, T_{MI} decreases and the resistivity increases. At ~6.3 GPa, the material becomes insulating in the measured temperature range and the resistivity as a function of temperature almost reproduces the case at ambient pressure. The T_{MI} *vs.* pressure is plotted in Figure 5.12. The transition temperature of our sample at low pressure is consistent to the result of other authors' polycrystalline samples,[27] but is lower than that of single crystals[144] (inset of Figure 5.12).

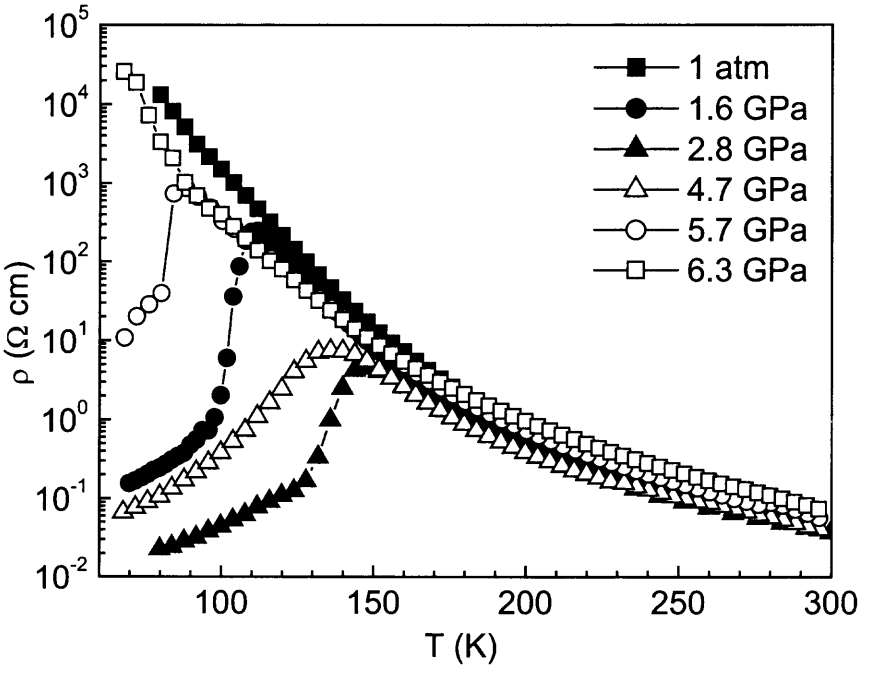

Figure 5.11 Temperature dependence of resistivity of $Pr_{0.7}Ca_{0.3}MnO_3$ under pressure.

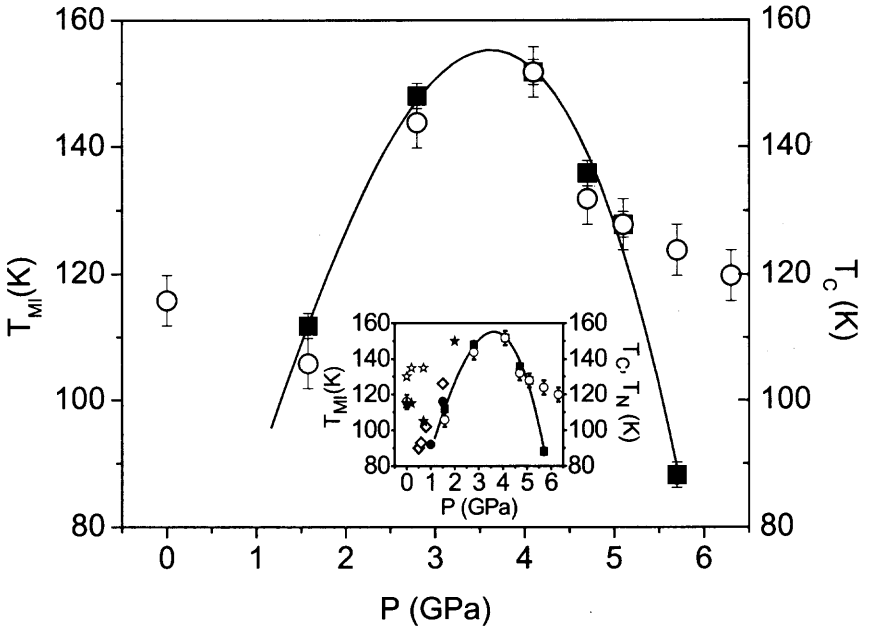

Figure 5.12 Pressure induced transition temperatures of $Pr_{0.7}Ca_{0.3}MnO_3$.

Note: the solid squares represent T_{MI}, the solid line is a fit to T_{MI} with a third order polynomial for eye-guiding; the open circles represent T_C extracted from the activation energy. (In the inset, the results of other authors are displayed for comparison with ours: the solid and open stars are T_C and T_N estimated from the neutron scattering result in Ref. 259; The open diamond symbols represent T_{MI} estimated from ref. 144, where the sample is single crystal; the solid circles represent T_{MI} estimated from ref. 27, where the sample is similar to ours.)

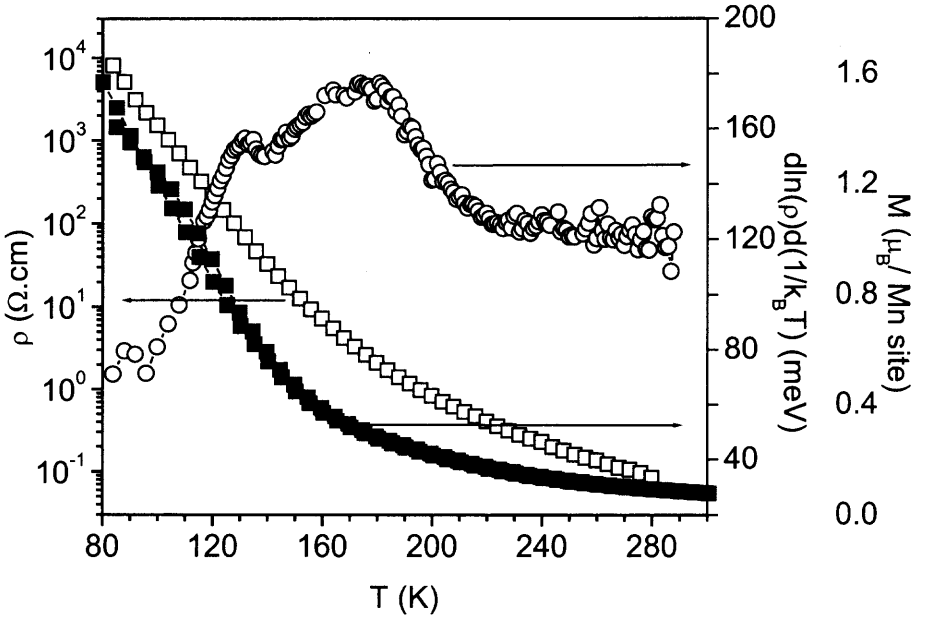

Figure 5.13 Temperature dependence of resistivity, magnetization and activation energy of $Pr_{0.7}Ca_{0.3}MnO_3$ at ambient pressure.

Note: magnetization (solid square) was measured from 4.2 K to 400 (field cooled and zero field cooled) at 10 kOe. Resistivity is represented by open squares and the open circles represent the activation energy.

According to Jirák *et al.*,[256] the low temperature magnetic state of this compound is ferromagnetic and antiferromagnetic phase-separated, in which the Curie and Néel temperatures are ~115 K and ~130 K respectively. By comparing the temperature dependence of resistivity, magnetization and E_g (Figure 5.13), the reduction of E_g can be correlated with the magnetic transition.

Yoshizawa *et al.*[259] reported that with pressure increasing up to 2 GPa, the charge ordering and antiferromagnetic components are gradually reduced and at 2 GPa only FM component presents. Below 0.7 GPa, the CO, AFM and FM transitions appear at different temperature upon cooling. From the E_g changes and comparison with the magnetization measurement as a function of temperature and Yoshizawa *et al.*'s[259] neutron diffraction result, this E_g drop is correlated to the ferromagnetic transition.

So we associate the point where E_g changes fastest with temperature as the ferromagnetic transition temperature T_C. The transition temperatures extracted at different pressures are plotted in Figure 5.12 together with T_{MI} [the T_{MI} estimated from ref. 144 (open diamonds) and ref. 27 (solid circles), the T_C (solid stars) and T_N (open stars) estimated from the neutron scattering results in ref. 259 are plotted in the inset together with our results for comparison]. It is clearly seen that in the measured pressure range of ~1.5-5GPa, T_C and T_{MI} coincide, indicating that pressure destroys the COI state and induces a FMM state at low temperature. But in the low pressure range and above ~5 GPa, the magnetic transition and MIT are decoupled and the material becomes insulating at pressures near to ambient pressure and above ~5 GPa.

The E_g as a function of temperature at different pressures are plotted in Figure 5.14. At ambient pressure, above ~220 K, E_g is ~125 meV, then increases upon cooling. Apparently, this energy changing corresponds to the charge ordering.

In the E_g *vs.* temperature plots (Figure 5.14), E_g rising on cooling disappears gradually with pressure increasing and at ~5.7 GPa, the CO state is completely suppressed so that the activation energy does not change with temperature and therefore,

the material displays a pure semiconductor behavior above the magnetic transition. Another trend noticeable is the E_g increase with pressure above ~2.8 GPa in the range near to room temperature. In the high pressure range, the activation energy becomes temperature dependent in the paramagnetic phase and decrease upon cooling. This behavior cannot be fit to the variable range and polaron hoping models. The origin is still not understood.

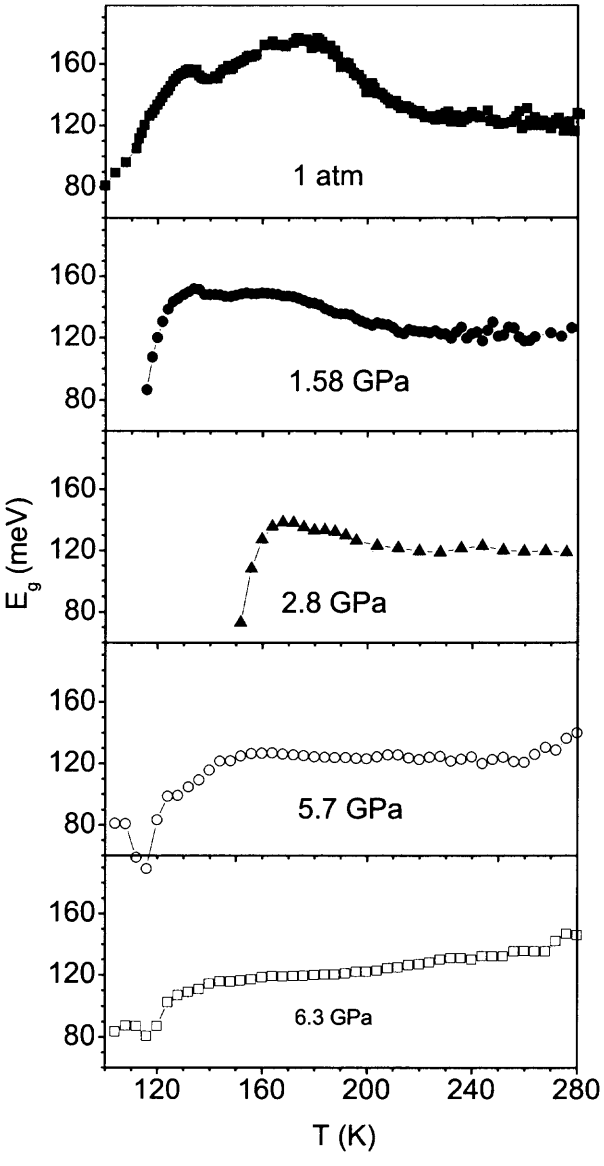

Figure 5.14 Activation energy of $Pr_{0.7}Ca_{0.3}MnO_3$ under pressure.

In the medium pressure range, at the optimum pressure, both the magnetic transition and metal-insulator transition temperature reach a maximum. This behavior is similar to that observed in the manganites with a larger bandwidth, in which it can be ascribed to the pressure induced Jahn-Teller distortion and Mn-O-Mn bond angle changes according to the double exchange theory.[161,162,260]

In the low (<~0.8 GPa) and high (>~5 GPa) pressure range, the material is more insulating and T_{MI} and T_C are decoupled. The neutron diffraction suggested that at low temperature this compound could be considered as FM and AFM phase-separated. The decoupling behavior may be similar to that in the x = 0.25 compound. The difference is that $Pr_{0.75}Ca_{0.25}MnO_3$ is more distorted and has a smaller bandwidth so that under high pressure T_{MI} and T_C never meet each other.

The charge ordering phase in the PCMO system is correlated to the lattice distortion, the buckling of the MnO_6 octahedra.[261] At T_{CO}, a transition from dynamic Jahn-Teller distortion to collective static distortion takes place.[262] So the CO state disappearing under pressure indicates that the octahedra buckling is compressed and only the dynamic distortion presents at pressure above the optimum pressure.

5.4.2 Structure at Room Temperature

Figure 5.15 is the refined local atomic structure data. In the measured pressure range, the Mn-O1 bond length only change slightly. The most obvious structure change under pressure is the Mn-O2 bond length splitting at ~3-4 GPa and therefore the coherent Jahn-Teller distortion. The Mn-O1-Mn bond angle increases ~10° and seems to keep unchanged above ~3 GPa, while the Mn-O2-Mn bond angle decreases in the measured pressure range.

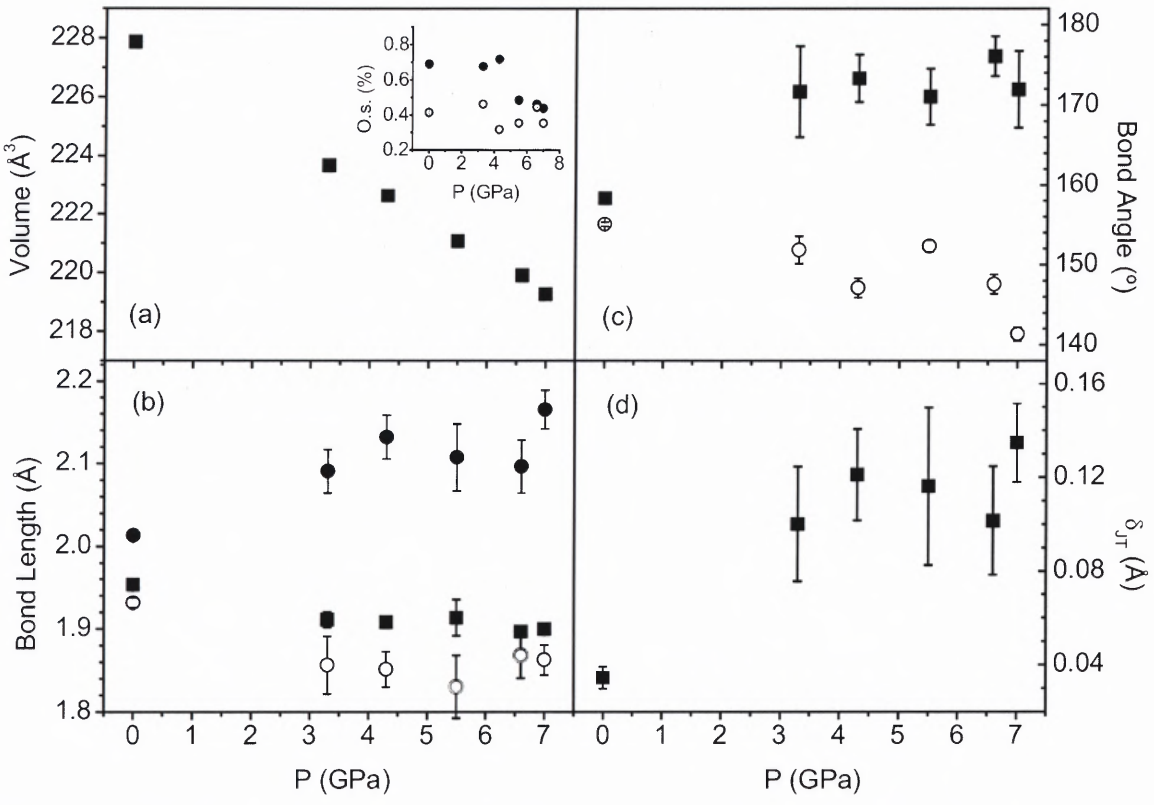

Figure 5.15 Structure of $Pr_{0.7}Ca_{0.3}MnO_3$ under pressure at room temperature.

Note: (a) unit cell volume; (b) Mn-O1 (solid square) and Mn-O2 (solid and open circles) bond lengths; (c) Mn-O1-Mn (solid square) and Mn-O2-Mn (open circle) bond angles; (d) amplitude of coherent Jahn-Teller distortion. The ab-plane (solid circle) and c-axis (open circle) orthorhombic strains are shown in the inset of (a).

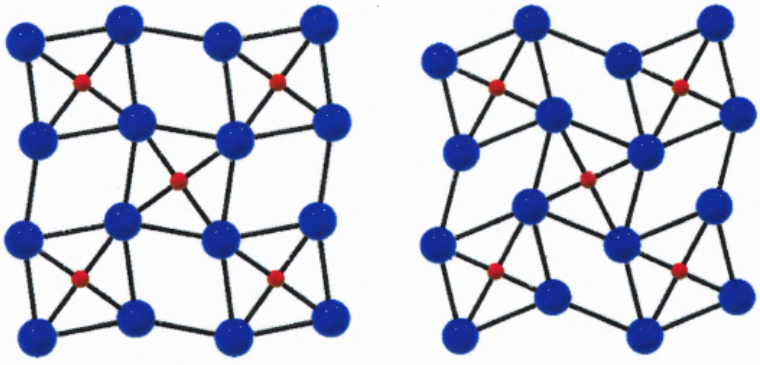

Figure 5.16 Projection of MnO_6 octahedron on ab-plane at ambient and 7 GPa.

Note: the small red ball is the manganese ion; the blue big ball is the O^{-2} ion.

In this small bandwidth manganite, pressure induces a local atomic structure transformation similar to that found in the large bandwidth manganites such as the $La_{0.75}Ca_{0.25}MnO_3$[162] and $La_{0.6}Y_{0.07}Ca_{0.33}MnO_3$ (chapter 4). This structure transformation lead to the MnO_6 octahedra to be aligned along c-axis or the tilting of the octahedra is reduced. But in the ab-plane the octahedra are squeezed to more distorted (Figure 5.16).

Above ~3 GPa, with pressure increase, the bond length and Mn-O1-Mn bond angle only change slightly, Mn-O2-Mn bond angle continuously decreasing.

Another feature is the dramatic changes of the orthorhombic strains when pressure across the critical point [inset of Figure 5.15(a)]. Above ~4 GPa, both the in-plane and c-axis strain are reduced, indicating a more cubic structure. However, this symmetry enhancement is accompanied by more local atomic structure distortion.

The Jahn-Teller distortion in this compound is different from that in the x = 0.25 compound. In $Pa_{0.75}Ca_{0.25}MnO_3$, with pressure increasing, JTD seems to be suppressed while in this compound JTD is enhanced.

5.4.3 Discussion and Summary

In both electronic properties and structure, upon pressure increasing, at ~3-4 GPa, there is a transition. Above this critical point, the static/dynamic Jahn-Teller distortion is enhanced. The increasing Mn-O1-Mn and decreasing Mn-O2-Mn bond angles may also lead to a maximum average bond angle. This explains the behavior of resistivity, the coupled T_C and T_{MI} in the range ~0.8-5 GPa according to the double exchange theory.

In the electronic and magnetic temperature *vs.* pressure phase diagram (Figure 5.12), in the high (>~5 GPa) and low (<~0.8 GPa) pressure range, the magnetic and electronic phase transitions are decoupled. The compound in the ambient and high pressure end is insulating. The decoupling of T_C and T_{MI} has some similarity to the x = 0.25 compound. Considering the decreasing of both the ab-plane and c-axis orthorhombic

strain, it is possible that in high range, pressure induces a ferromagnetic insulating state.

Above ~4 GPa, the ab-plane and c-axis orthorhombic strain reduction, Jahn-Teller distortion increase, charge ordering state disappearing, and the E_g temperature dependence in paramagnetic insulating phase may suggest a dynamic Jahn-Teller distortion instead of the static dynamic JTD.

5.5 Electron Transport and Structure of $Pr_{0.65}Ca_{0.35}MnO_3$ under Pressure

5.5.1 Electron Transport

In this compound, charge ordering occurs below ~230 K, with the magnetic state being antiferromagnetic. Between ~140 K and ~60 K, a CE-type AFI phase forms; below ~60 K, CAFI forms (Figure 1.7). In the whole temperature, the compound is insulating and in the paramagnetic phase displays semiconductor behavior.

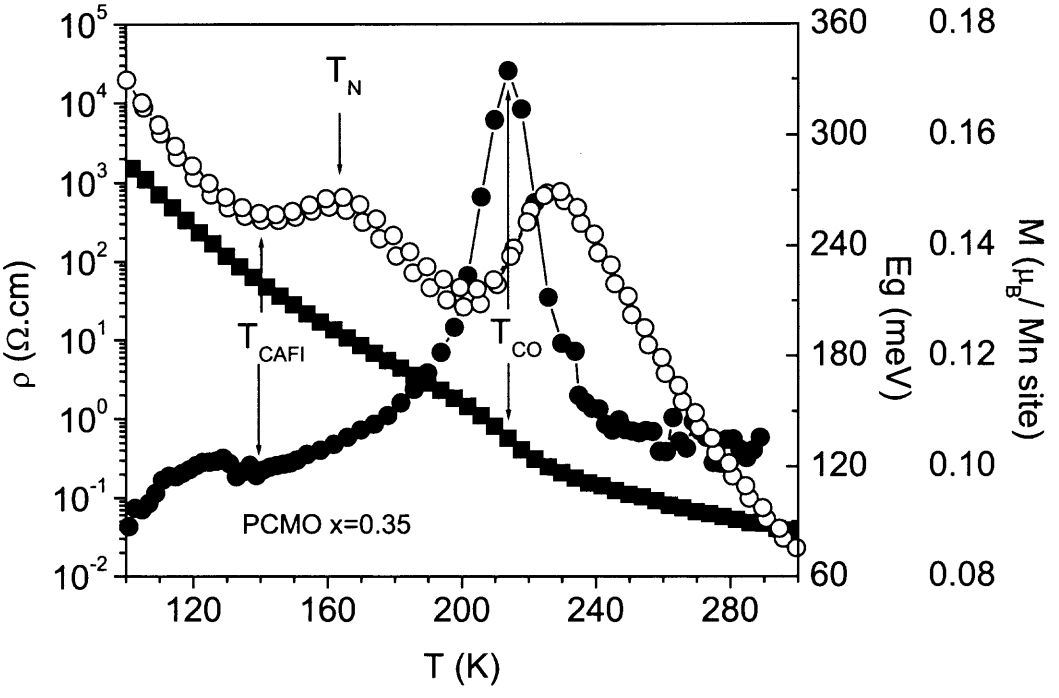

Figure 5.17 Temperature dependence of resistivity, magnetization and activation energy of $Pr_{0.65}Ca_{0.35}MnO_3$ at ambient pressure.

As in the other two samples studied, charge ordering, magnetic state can be observed through resistivity measurement. Figure 5.17 is the temperature dependence of resistivity, magnetization and activation energy at ambient pressure. On the E_g curve, corresponding to a sharp peak at ~215 K is the charge ordering, as in a compound with similar doping.[263] In the temperature range of ~130-140 K, there is a small bump, which may correspond to the CE-type AFI transition. In the measured temperature range, the low temperature magnetic state is antiferromagnetic, displaying in E_g as a slow change with temperature.

Under pressure, both the charge and spin states are changed. Figure 5.18 shows the resistivity under pressure. It seems that under pressure below ~2 GPa, a metallic state is induced in the medium temperature and the T_{MI} increases upon increasing pressure. But the low temperature state is still insulating. With pressure increasing, this low temperature insulating state is completely suppressed and the material becomes ferromagnetic metallic. This can be seen in the E_g *vs.* T curves (Figure 5.19). Above ~2 GPa, the E_g as a function of temperature is same as the other two samples with ferromagnetic phases. T_{MI} as a function of pressure is plotted in Figure 5.20. Apparently, it follows the same manor of other samples.

Another obvious effect is on the charge ordering. On pressure increase, charge ordering is suppressed and the transition temperature is shifted to low temperature and finally the charge ordering transition disappears (Figure 5.19). The charge ordering transition temperature as a function of pressure is plotted together with T_{MI} in Figure 5.20. Because the charge ordering transition temperature, corresponding to the E_g increases upon cooling, is hard to define in the E_g plots, the peak temperature of E_g is used to represent the charge ordering transition. In this way, T_{CO} is lower than it appears to be.

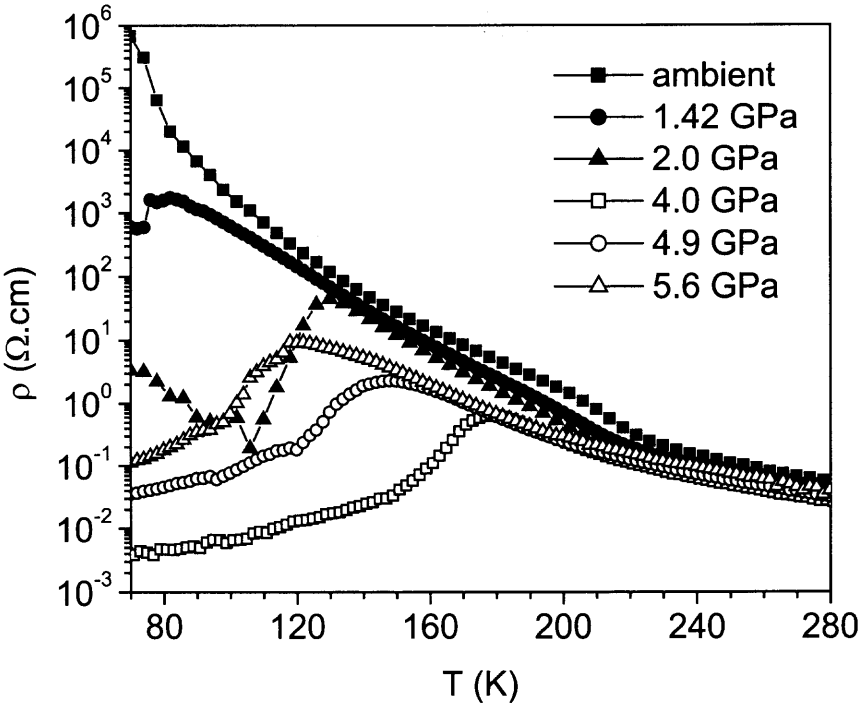

Figure 5.18 Resistivity of $Pr_{0.65}Ca_{0.35}MnO_3$ at different pressures.

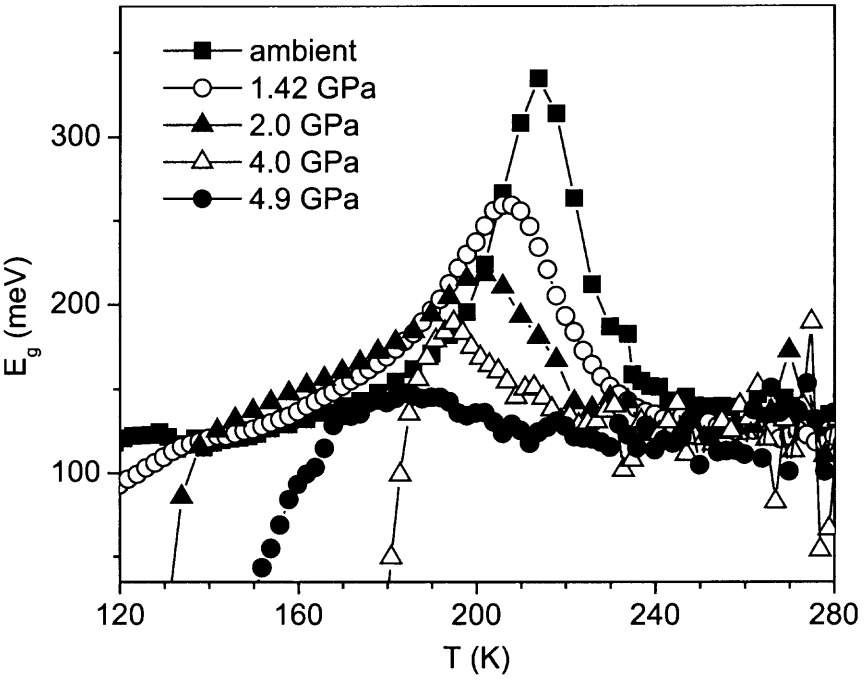

Figure 5.19 Activation energy E_g of $Pr_{0.65}Ca_{0.35}MnO_3$ under pressure.

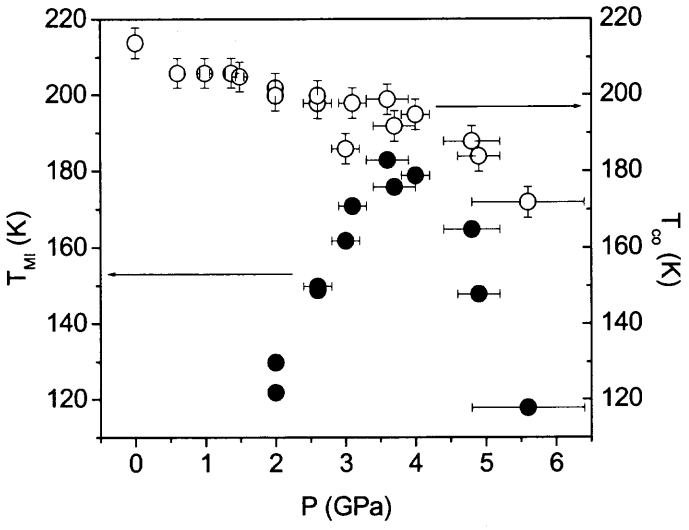

Figure 5.20 Pressure induced metal-insulator transition and charge order transition temperature shift in $Pr_{0.65}Ca_{0.35}MnO_3$.

5.5.2 Structure at Room Temperature

Because of the quality of the collected data, for this sample, only the lattice parameters can be extracted. The corresponding orthorhombic strain in the ab-plane and along c-axis is shown in Figure 5.21. It seems that the monotonic orthorhombic strain decreasing is partly responsible for the charge ordering disappearance under pressure.

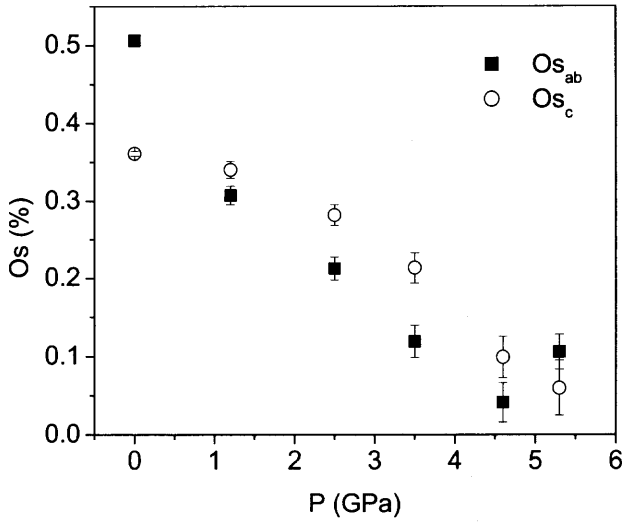

Figure 5.21 Ab-plane and c-axis orthorhombic strain of $Pr_{0.65}Ca_{0.35}MnO_3$.

5.4.3 Discussion and Summary

Similar to the other two samples, there is also a critical pressure for the MIT temperature, which could possibly be ascribed to local structure change. The orthorhombic strain decreasing with pressure partly explains the charge ordering suppressing under pressure. Due to the data quality, it cannot be determined if E_g is temperature dependent in paramagnetic phase in high pressure range.

5.6 Summary to $Pr_{1-x}Ca_xMnO_3$ Doping System

In this doping system, the size of Ca^{2+} is larger than that of Pr^{3+}. With x increase, the material is expected to have smaller distortion and hence, a larger bandwidth. Although all three samples are insulating at ambient pressure, it is shown that the sample with a larger bandwidth has a higher maximum T_{MI} at the critical pressure P* (Figure 5.22).

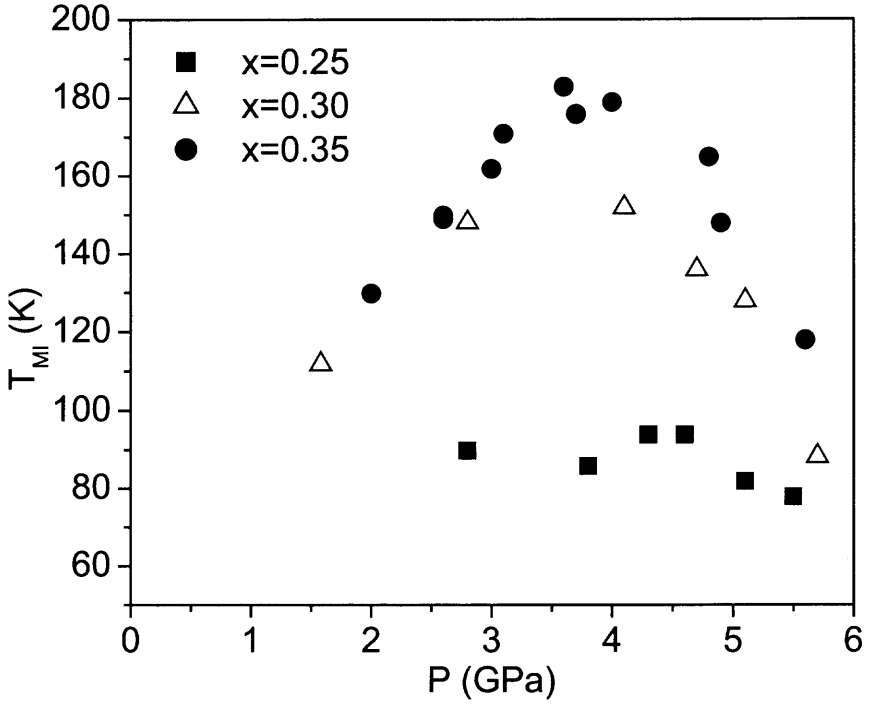

Figure 5.22 Comparison of pressure induced metal-insulator transition temperature of $Pr_{1-x}Ca_xMnO_3$ (x = 0.25, 0.30, 0.35).

The coupling of the magnetic and electronic transition under pressure is an interesting topic in this system. Because of the small bandwidth, sometimes the superexchange dominates, the material is insulating and T_{MI} and T_C may be decoupled due to the competition between double exchange and superexchange.

In the x = 0.25 compound, superexchange is so strong that even under pressure T_{MI} and T_C never coincide (Figure 5.8). With pressure increase, T_C decreases and T_{MI} increases, indicating that superexchange is suppressed due to the bandwidth increase. From the structure measurements at room temperature (Figure 5.10), it appears that the ab-plane Mn-O2-Mn bond angle and c-axis bond angle Mn-O1-Mn compete with each other that leads to an optimum in the range ~3-4 GPa. Above the critical pressure, because of the bandwidth decreasing and the orthorhombic strain decreasing induced orbital ordering, the ferromagnetic superexchange between Mn sites dominates again, and therefore T_C increases and T_{MI} decreases.

The x = 0.30 doping concentration is a critical point. It is at the boundary of the FI phase ($x < 0.30$) and the CO, AFI, CAFI phase ($x > 0.30$) in the chemical doping phase diagram (Figure 1.7). Under pressure, the coupling of T_{MI} and T_C displays critical behavior: in the low pressure near to ambient and high pressure above ~5 GPa where there is larger distortion and hence, smaller bandwidth, the compound is insulating and T_{MI} and T_C are decoupled. In the medium pressure, the bandwidth is large enough, superexchange is suppressed and the ferromagnetic state is coupled to the metallic state (Figure 5.12).

For the x = 0.35 sample, because of the data quality, more details about the coupling cannot be acquired.

Charge ordering is another interesting feature in the PCMO system. In the three samples studied, the x = 0.25 sample is not reported to have charge ordering state. But from the activation energy plots, in this sample there is also a charge ordering transition at ~200 K. The charge ordering state in x = 0.35 sample is the strongest one in the three

samples. Under pressure, charge ordering states in all the samples are suppressed below the critical pressure P*. Above P*, for the x = 0.25 and 0.30 compound, in paramagnetic phase, an insulating state with unknown conducting mechanism appears. In this state, E_g increases on warming. It is speculated that dynamic JTD exists in this phase.

In summary, bandwidth plays an essential role in the magnetic and electronic properties in this system. The bandwidth competes with superexchange between Mn sites, determining if there is a possibility for the metal-insulator transition and magnetic transition coupling, even under high pressure. When bandwidth is too small, even under pressure, the magnetic and electronic transition cannot be coupled. Larger bandwidth compounds have higher T_{MI} at P*. For the structure, it was found that the orthorhombic distortions (both in ab-plane and along c-axis) decrease with pressure (Figure 5.10, Figure 5.15, Figure 5.21). In the x = 0.25 compound, the JTD is reduced in high pressure range while in the x = 0.30 compound JTD is stabilized above P*. The bond angles also behave differently under pressure: for x = 0.25, Mn-O2-Mn increases slightly while Mn-O1-Mn decreases with pressure; for x = 0.30, Mn-O2-Mn decreases slightly while Mn-O1-Mn is stable above P*. To acquire more details about the structure evolution under pressure, more sophisticated structure measurements, such as high pressure Raman scattering and neutron scattering, especially measurements at low temperatures, are necessary.

CHAPTER 6

ELECTRON TRANSPORT AND STRUCTURE OF $Nd_{1-x}Sr_xMnO_3$ UNDER PRESSURE

6.1 Introduction

In $Nd_{1-x}Sr_xMnO_3$ manganite, the size difference between Nd^{3+} (1.163 Å) and Sr^{2+} (1.31 Å) is large (~0.15 Å). By changing Sr^{2+} concentration, interesting spin, charge and orbital phases are produced.[15] This doping system, especially near x~0.5 doping concentration, has been extensively investigated.

In the x = 0.5 compound, upon cooling from room temperature, there exist a transition from paramagnetic insulating phase to ferromagnetic metallic phase at ~255 K and a transition from FMM phase to charge ordering antiferromagnetic insulating phase at ~155 K. The magnetic structure in charge ordering antiferromagnetic insulating phase is CE-type.[264] When a magnetic field is applied, the FMM state is enhanced so that T_{CO} is lowered and T_C increased. Above 7 T, the charge ordering state melts.[31] The magnetic field induced collapse of charge ordering state is accompanied by a structural transition, at which the volume drastically increases, leading to large positive magnetovolume effect while giving rise to a large negative MR (Figure 1.9).[265]

In $Nd_{0.5}Sr_{0.5}MnO_3$, orbital ordering coincides to charge ordering. The orbital ordering is reported to be $d_{3x^2-r^2}$ / $d_{3y^2-r^2}$ -type OO (Figure 1.13),[87] or $d_{x^2-y^2}$ -type.[266]

$Nd_{0.45}Sr_{0.55}Mn_3$ is an A-type antiferromagnetic metal with coupled magnetic and structure transition at ~225 K.[264] Spins are ferromagnetically aligned in ab-plane in Pbnm symmetry. According to double exchange theory, charge carriers are confined within ab-plane and the transport along c-axis is quenched so that resistivity is highly anisotropic (ρ_c/ρ_{ab} ~10^4 at 35 mK).[267] It is reported that the antiferromagnetic transition is accompanied by $d_{x^2-y^2}$ -type orbital ordering, and that the orbital ordering and A-type antiferromagnetic spin ordering can be simultaneously destructed by a high magnetic

field, accompanied by a discontinuous decreasc of resistivity.[268]

Two space groups have been used in literatures to describe the symmetry: the Pbnm/Pnma and Imma/Ibmm. In Pbnm symmetry, the MnO_6 octahedra rotate around both b and c –axis. In Ibmm symmetry, the tilting of octahedra is restricted to c-axis, and thereby the x and y coordinates of in-plane oxygen O2 are fixed to 1/4. As a result, the two Mn–O bonds in the ab-plane are identical (Figure 6.1). Within Pbnm/Pnma symmetry, while crossing to the charge ordering state from high temperature, there is a transition in which the lattice parameters a and b-axis are elongated and c-axis is compressed (Figure 1.9).[264,269] But other authors[269,270,271,272] reported that the structure at room temperature is Imma/Ibmm. During the transition from FMM to antiferromagnetic COI state, a structural transition happens in which the crystal symmetry lowers to the monoclinic P21/m symmetry.[270,272] Ritter *et al.*[271] suggested that the low temperature antiferromagnetic COI phase is phase-segregated into two different crystallographic structural and three magnetic phases: orthorhombic (Imma) ferromagnetic, orthorhombic (Imma) A-type antiferromagnetic, and monoclinic (P21/m) charge-ordered CE-type antiferromagnetic phases. When a magnetic field is applied, the charge-ordered monoclinic phase collapses and completely transforms into FMM orthorhombic phase. Kajimoto *et al.*[269] reported that for the compounds of $x = 0.49 \sim 0.75$, the structure is fit by Ibmm/Imma in the PMI phase while in low temperature antiferromagnetic phase, the Pbnm and Ibnm structure cannot be distinguished.

For $Nd_{0.5}Sr_{0.5}MnO_3$, hydrostatic pressure and uniaxial pressure affect the charge ordering and FMM phases differently. Hydrostatic pressure up to 1 GPa was found to increase T_C at 6.8 K/GPa and decrease T_{CO} at –8.4 K/GPa,[273] while the uniaxial pressure along c-axis increases T_{CO} at 0.19 K/MPa and decreases T_C at -0.06 K/MPa.[274] For x = 0.55, by applying uniaxial pressure along c-axis, T_N can be increased at 0.066 K/MPa, which may imply the stabilization of the $d_{x^2-y^2}$ orbital.[274]

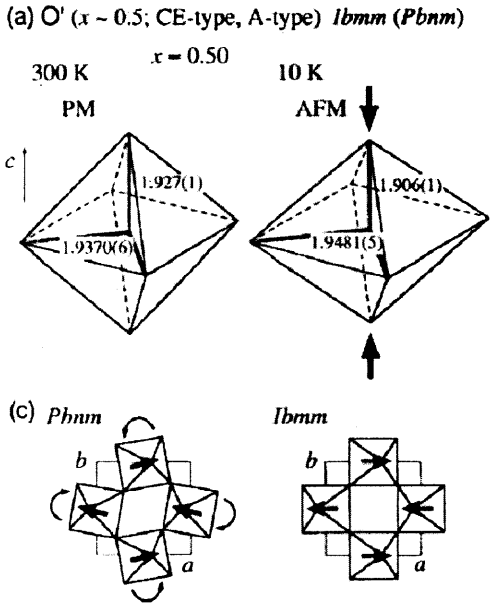

Figure 6.1 (a) Schematic picture of MnO_6 octahedra in *O'* phase for paramagnetic and low-temperature antiferromagnetic phases; (c) Rotation patterns in the basal plane for each of the designated structures.[269]

In this chapter, pressure effects on the charge ordering, FMM, antiferromagnetic states of the x = 0.45 and 0.5 compound will be observed through resistivity and structure measurements. The result will be compared with that in thin films.

6.2 Samples

The samples were prepared by solid-state reaction. Stoichiometric amount of Nd_2O_3, MnO_2, and $SrCO_3$ powder were mixed, ground and calcined at 900 °C for 15 hours; cooled down to room temperature, reground; calcined again at 1200 °C for 17 hours. The powder was pressed into pellets. Pellets were sintered at 1500 °C for 12 hours, cooled down to 800 °C at the rate 5 °C/min, then quickly cooled down to room temperature. The pellets were annealed at 1200 °C and cooled down slowly to room temperature at 1 °C /min.

The x-ray diffraction patterns taken at room temperature showed a single crystallographic phase (Figure 6.2, Figure 6.3). The structure was refined to Pbnm

symmetry using the Rietveld method. The results are listed in Table 6.1 and Table 6.2. Both have an orthorhombic O' structure with $a > b > \frac{c}{\sqrt{2}}$.

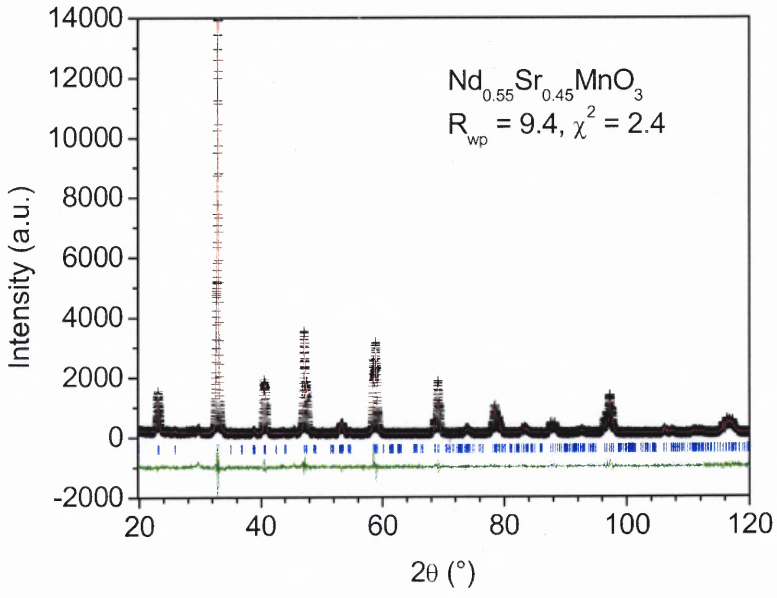

Figure 6.2 Rietveld fitting of $Nd_{0.55}Sr_{0.45}MnO_3$ x-ray diffraction pattern.

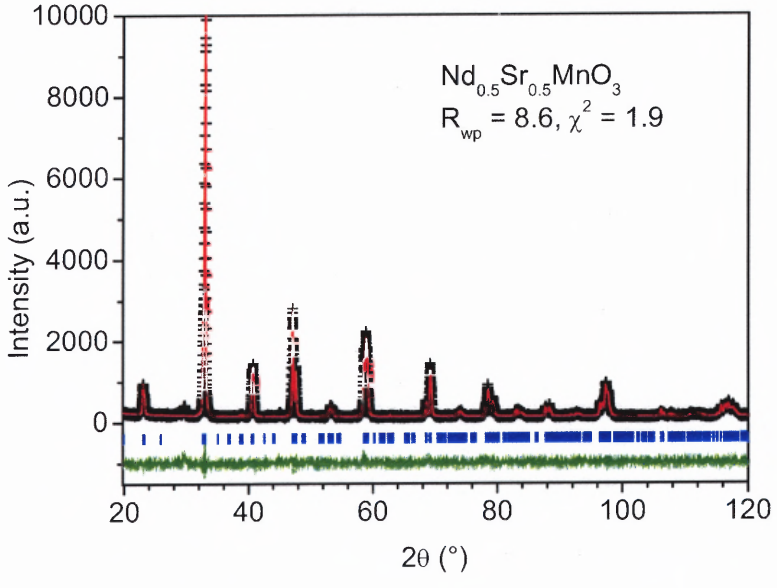

Figure 6.3 Rietveld fitting of $Nd_{0.5}Sr_{0.5}MnO_3$ x-ray diffraction pattern.

Table 6.1 Rietveld Refinement Results for $Nd_{1-x}Sr_xMnO_3$ at Room Temperature

Doping (x)		x = 0.45	x = 0.50
Unit Cell	a (Å)	5.47152(3)	5.47291(1)
	b (Å)	5.43154(3)	5.42940(1)
	c (Å)	7.65197(5)	7.63330(2)
Nr/Sr	x	0.5016(2)	0.00182(6)
	y	0.50935(9)	0.99993(8)
O(1)	x	0.4477(5)	0.9596(2)
	y	0.9970(9)	0.5189(2)
O(2)	x	0.734(1)	0.2579(4)
	y	0.2727(10)	0.7619(4)
	z	0.0253(3)	0.0275(1)

Note: x, y, z are the fractional atomic positions; a, b, c are the unit cell parameters; the fit errors are in the brackets following the numbers. The atoms are located at the Wyckoff positions of: Pr/Ca at 4c: (x, y, 1/4), Mn at 4b: (1/2, 0, 0), O(1) at 4c: (x, y, 1/4), O(2) at 8d: (x, y, z).

Table 6.2 Local Atomic Structure of $Nd_{1-x}Sr_xMnO_3$ at Room Temperature

Doping (x)		x = 0.45	x = 0.50
Bond Length	Mn-O1 (Å)	1.9343(4)	1.9238(1)
	Mn-O2 (Å)	1.968(6)	2.014(2)
	Mn-O2 (Å)	1.917(6)	1.863(2)
Bond Angle	Mn-O1-Mn	163.0(2)	165.5(5)
	Mn-O2-Mn	165.6(2)	167.5(5)
Jahn-Teller distortion		0.021(5)	0.062(2)

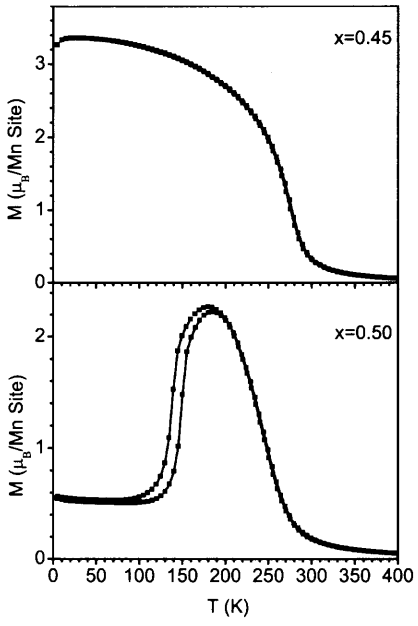

Figure 6.4 Magnetization measurements of $Nd_{1-x}Sr_xMnO_3$ (x = 0.45, 0.50) at 10 kOe (FC and ZFC).

The magnetization measurements are shown in Figure 6.4. The low temperature moment of the x = 0.45 compound in 1 T magnetic field is 2.4μ_B. T_C (274.4 ± 2.5 K) is approximate to the results published (Figure 1.7). For the x = 0.50 compound, T_{CO} and T_C extracted is 150 ± 2.5 K and 245 ± 2.5 K, respectively, consistent to that in Figure 1.7.

6.3 Electron Transport and Structure of $Nd_{0.55}Sr_{0.45}MnO_3$ under Pressure

6.3.1 Electron Transport

$Nd_{0.55}Sr_{0.45}MnO_3$ is a double exchange compound, with a FMM to PMI transition at ~280 K on warming up. Figure 6.5 is the resistivity evolution with temperature at different pressures. The most interesting feature is the insulating state arising in low temperature range under pressure (more clearly shown in Figure 6.6). With pressure increase, the insulating behavior dominates above ~6 GPa. Correspondingly, resistivity in the measured temperature changes with pressure (Figure 6.7). In the low pressure range, T_{MI} (T_C) increases with pressure. Because of the limit of instrument, T_{MI} above the upper

limit in the pressure range of ~2-4 GPa cannot be determined. Above ~4 GPa, the transition temperature decreases on pressure increasing. Above ~6 GPa, the insulating state dominates so that the transition temperature can not be determined, although there is still trace of metallic behavior. The transition temperature is plotted in Figure 6.8.

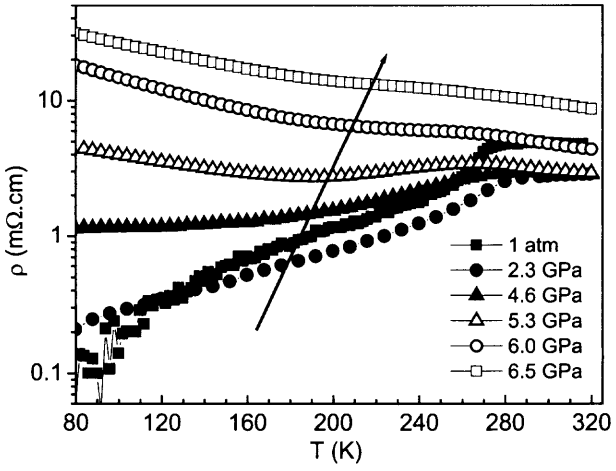

Figure 6.5 Resistivity of $Nd_{0.55}Sr_{0.45}MnO_3$ under pressure.

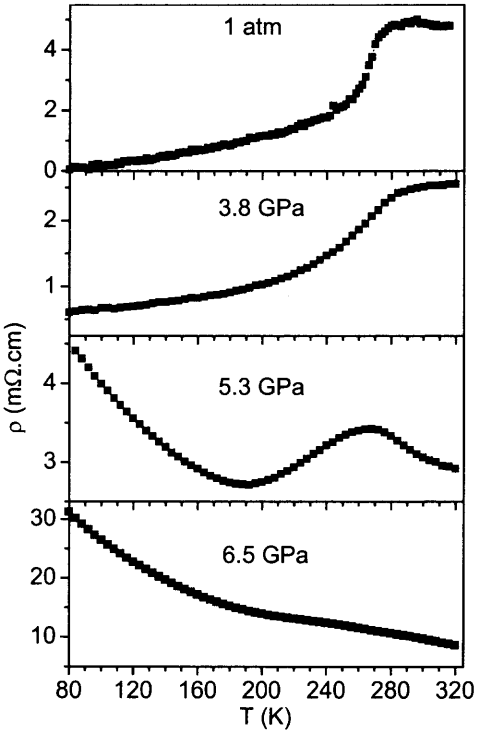

Figure 6.6 Better view of Figure 6.5.

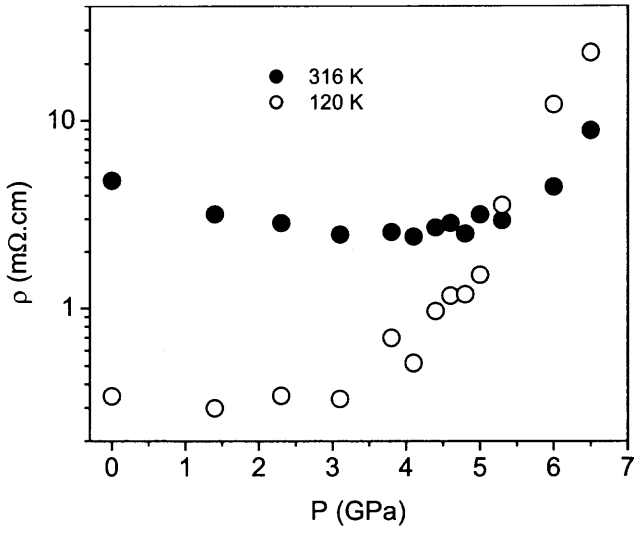

Figure 6.7 Resistivity evolution of $Nd_{0.55}Sr_{0.45}MnO_3$ at 316 K and 120 K under pressure.

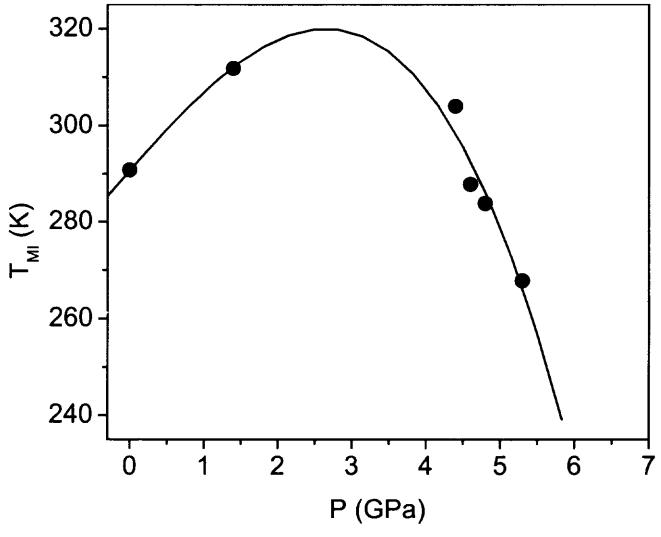

Figure 6.8 Metal-insulator transition temperature of $Nd_{0.55}Sr_{0.45}MnO_3$ under pressure.
Note: The solid line is a 3rd polynomial fitting.

In this compound, the behavior of T_{MI} is similar to that in LYCMO and PCMO systems. The resistivity behavior and the insulating state emergence in the pressure range above the critical point is more interesting. Below the critical pressure, resistivity in the low temperature FMM phase displays a saturation behavior, while in the paramagnetic insulating phase, resistivity is suppressed as in other compounds studied (Figure 6.7). This indicates that in the large bandwidth manganites the relative change caused by

pressure is small. Above the critical pressure, the insulating state arising can be ascribed to the universal structure change as in the LYCMO and PCMO compounds.

It is noted that the mechanism of becoming insulating under pressure in this compound is different from the LYCMO and PCMO compounds. In LYCMO and PCMO compounds, the material become insulating through the suppression of the FMM state displaying as the T_{MI} decreasing above the critical pressure. In $Nd_{0.55}Sr_{0.45}MnO_3$, the insulating state at high pressures comes from two aspects: the suppressing of FMM state and the expanding of a low temperature insulating phase, which appears with pressure increasing and finally dominates at high pressures. While the material becomes insulating under pressure, the enhancement of insulating component contributes most.

Abramovich *et al.*[275] proposed a magnetic two-phase state in low temperature in this compound, in which the AFI droplets lie in the conducting FM host. In the phase-separation model, the mechanism of the material becoming insulating can be understood as pressure induced percolation that the increasing pressure suppresses FMM component and enhances AFI component above P*. Under pressure below P*, the FMM component is enhanced and the insulating one is suppressed. With pressure increase, the insulating component grows up and finally dominates at high pressures, and consequently, the material becomes insulating.

At high pressures where the compound becomes insulating, the temperature dependence is very similar to that of $Nd_{0.45}Sr_{0.55}MnO_3$ (Figure 6.9). The x = 0.55 compound is reported to be an A-type antiferromagnetic metal that is insulating along c-axis and metallic in the ab-plane.[264] In a high magnetic field of 35 T, the resistivity of $Nd_{0.45}Sr_{0.55}MnO_3$ becomes similar to the x = 0.45 case. This is ascribed to the destruction of the A-type antiferromagnetic spin ordering and the $d_{x^2-y^2}$ orbital ordering.[268] The high pressure and high magnetic field have contrary effect on electron transport. Considering the resistivity of the x = 0.45 compound under pressure, it is reasonable to speculate that it has a similar spin and orbital structure to the x = 0.55 compound.

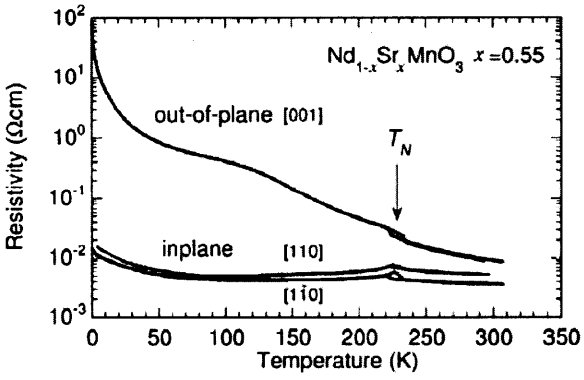

Figure 6.9 Resistivity of $Nd_{0.45}Sr_{0.55}MnO_3$.[76]

6.3.2 Structure at Room Temperature

The lattice parameters extracted by fitting the x-ray diffraction pattern with Rietveld method are shown in Figure 6.10. Under pressure, the three lattice parameters have different compressibility [Figure 6.10(d)]. Both the ab-plane and the c-axis orthorhombic strains increase with pressure [Figure 6.10(c)].

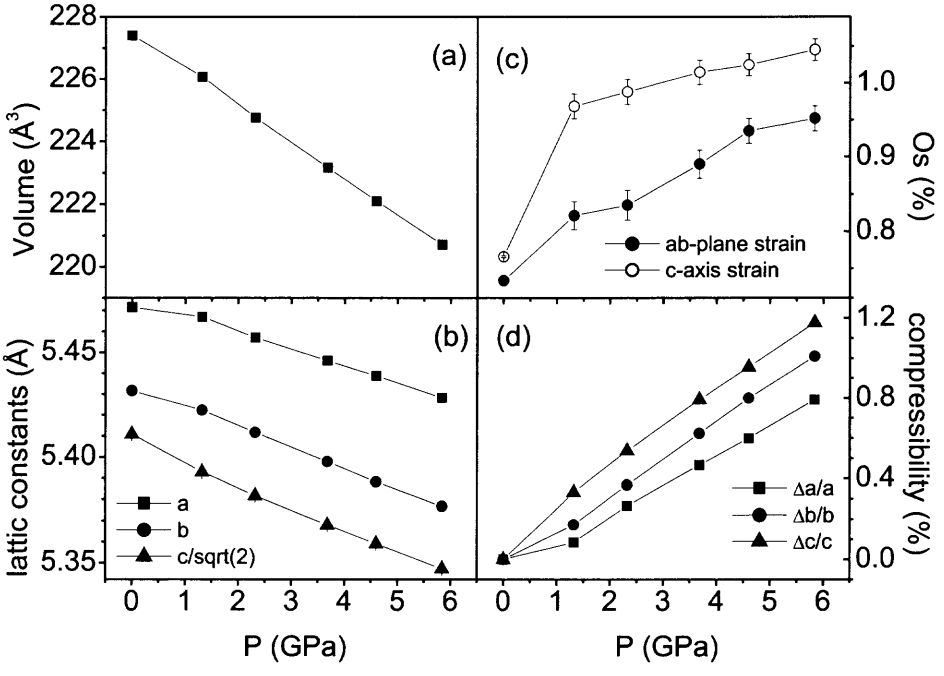

Figure 6.10 Lattice parameter evolution of $Nd_{0.55}Sr_{0.45}MnO_3$ under pressure.

Note: (a) unit cell volume; (b) lattice parameters a, b, c; (c) ab-plane and c-axis orthorhombic strain; (d) compressibility of lattice parameters

6.3.3 Discussion and Summary

Above it is speculated that the x = 0.45 compound may have a similar spin and orbital structure to the x = 0.55 compound at high pressures. But the structure of x = 0.55 compound is $O^{\dagger}$ in which $a \approx b < \frac{c}{\sqrt{2}}$. The corresponding orthorhombic strain in ab-plane is ~0, along c-axis is -2% (calculated with the data in ref. 269). This compound has a $d_{x^2-y^2}$ -type OO and is an A-type antiferromagnetic metal.

Under pressure, the orthorhombic strain in both c-axis and ab-plane is increased in the x = 0.45 compound, so the high pressure structure is more different from the x = 0.55 structure than at ambient pressure. This implies that at least the orbital state is different. However, the similarity between the resistivity (in both absolute value and shape) seems to suggest an A-type antiferromagnetic state induced by pressure in $Nd_{0.55}Sr_{0.45}MnO_3$.

6.4 Electron Transport and Structure of $Nd_{0.5}Sr_{0.5}MnO_3$ under Pressure

6.4.1 Electron Transport

In Figure 6.11 is the resistivity of $Nd_{0.5}Sr_{0.5}MnO_3$. In the low temperature charge ordering insulating state, the resistivity is reduced, indicating that CO is suppressed by increasing pressure. On the other hand, while resistivity is compressed in the CO phase, the insulating manner extends to high temperature so that the FM metallic state is also suppressed. If the temperature where the insulating and metallic state cross (the resistivity minimum) is defined as the CO transition temperature, T_{CO} increases with increasing pressure and it seems to decrease above ~4 GPa (Figure 6.12). Pressure only affects the metal-insulator transition slightly. With pressure increase, T_{MI} increases and above ~3 GPa, T_{MI} drops. Under pressure, the highest T_{MI} is only ~4 K difference from that at ambient pressure. With pressure increase, the resistivity in the paramagnetic insulating phase is also suppressed.

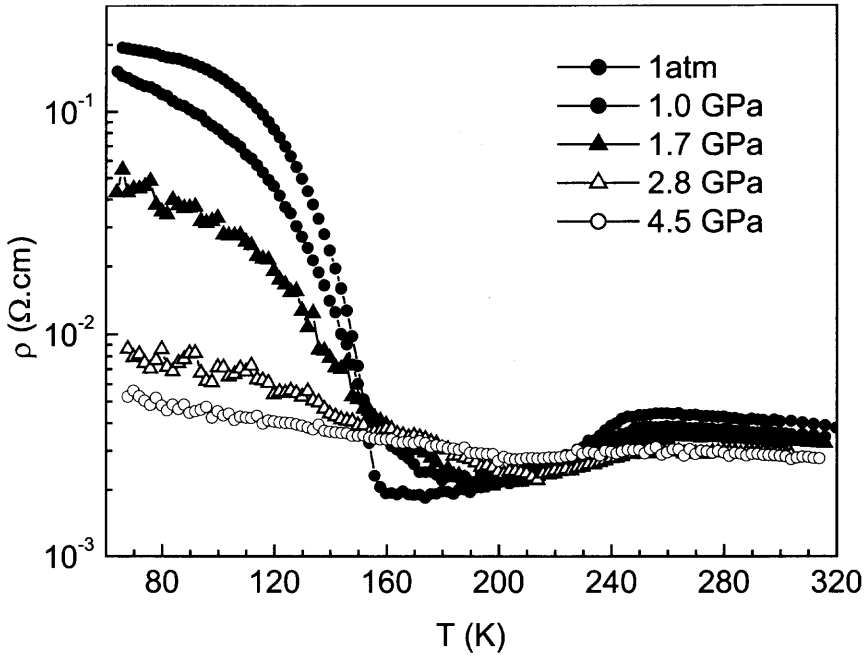

Figure 6.11 Resistivity of $Nd_{0.5}Sr_{0.5}MnO_3$ as a function at different pressures.

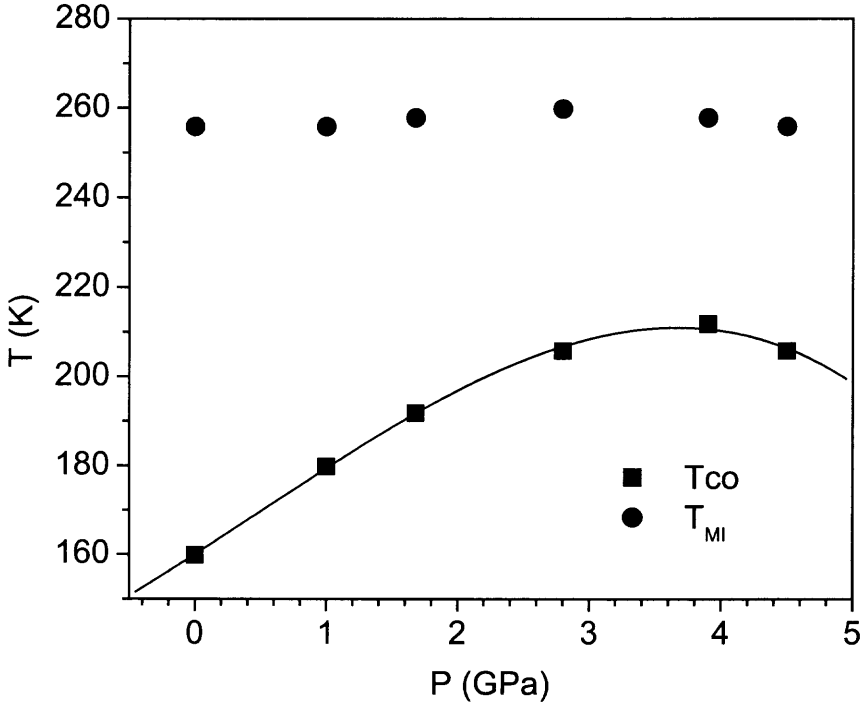

Figure 6.12 Pressure dependence of charge order transition and metal-insulator transition temperature of $Nd_{0.5}Sr_{0.5}MnO_3$.

Note: the solid line is a third-order polynomial fitting which gives a $dT_{CO}/dP = 19 \pm 2$ K at ambient pressure.

6.4.2 Structure at Room Temperature

In Figure 6.13, the compressibility of the three lattice parameters is only slightly different [Figure 6.13(d)], leading to a small orthorhombic strain changes [Figure 6.13(c)]. The c-axis strain is increased while ab-plane strain is decreased.

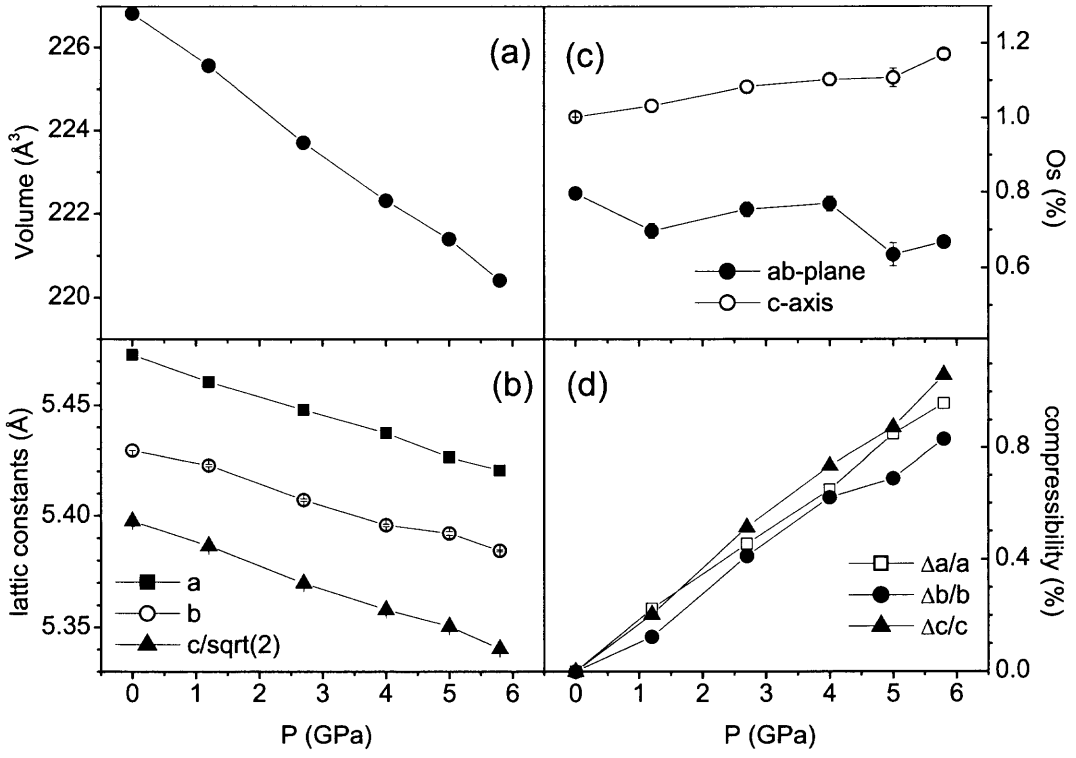

Figure 6.13 Lattice parameter of $Nd_{0.5}Sr_{0.5}MnO_3$ under pressure.

Note: (a) unit cell volume; (b) lattice parameters a, b, c; (c) ab-plane and c-axis orthorhombic strain; (d) compressibility of lattice parameters

6.4.3 Discussion and Summary

Resistivity measurements show that T_{CO} increases with pressure at least at pressures below ~3.8 GPa, but T_{MI} does not change (Figure 6.12). This is different from that hydrostatic pressure below 1 GPa increases T_C and decreases T_{CO} reported by other authors.[273] On the other hand, our results are similar to the result of uniaxial pressure along c-axis that increases T_{CO} and decrease T_C.[274] The CO temperature increase with pressure is a little puzzling. When we look at the structure, it is found that the

orthorhombic strain along c-axis is increased while in ab-plane is decreased. According to the structure measurements of Kuwahara *et al.*,[31] the CO state corresponds to a higher orthorhombic strain state.

Roy *et al.*[167] reported that pressure above ~1.5 GPa can split the coincident AFI and transitions in which T_{CO} increases while T_N decreases. That resistivity rises up at the magnetic transition but not at CO transition implies that the abrupt resistivity increase comes mostly from the CE-type antiferromagnetic state but not CO state. We did not observe the T_{CO} and T_N splitting in a larger pressure range, possibility because our sample is polycrystalline. The large suppression of resistivity indicates that the AF state, specifically the CE-type AF state, is suppressed. This is also consistent to the ab-plane orthorhombic strain reduction.

In $Nd_{0.5}Sr_{0.5}MnO_3$, by substituting Nd^{3+} with larger size La^{3+} in $(Nd_{1-z}La_z)_{1/2}Sr_{1/2}MnO_3$ ($0< z <1$), the bandwidth W is increased and hence both resistivity in CO phase and T_{CO} decrease while T_C increasing. The compounds of $z < 0.5$ still have CE-type CO phase and FMM phase but with lower resistivity than the parent compound due to larger bandwidth. When applied pressure, possibility a transition from CO CE-type AFI to A-type AFI is induced, in which resistivity is suppressed and T_{CO} gradually increased with pressure.[144] This is consistent to our result in the small bandwidth parent compound but at a much higher pressure. The smaller ab-plane strain and larger c-axis strain at high pressures may favor an A-type antiferromagnetic state and $d_{x^2-y^2}$ orbital ordering as in the $x = 0.55$ compound. In this A-type antiferromagnetic insulating state, resistivity is decreased due to enhanced in-plane transfer integral by reducing in-plane strain. In the phase-separation model,[271] the A-type antiferromagnetic phase is enhanced and the charge ordering CE-type antiferromagnetic phase is suppressed concomitantly by pressure. Because bandwidth is sensitive to the local atom structure of MnO_6 octahedra, especially the Mn-O-Mn bond angle, it is highly desired to measure the local atomic structure to explain the electronic and magnetic behavior under pressure.

6.5 Summary to $Nd_{1-x}Sr_xMnO_3$ Doping System

In the DE sample $Nd_{0.55}Sr_{0.45}MnO_3$, as in other systems, the ferromagnetic state experiences similar process, with conductivity and T_C (T_{MI}) first increasing below P* and decreasing above P*. However, in this sample, with pressure increase, a low temperature insulating component arises and dominates so that the material becomes insulating at high pressures.

In the CO sample $Nd_{0.5}Sr_{0.5}MnO_3$, with pressure increase, the resistivity of the CO phase is suppressed. But T_{CO} increases with pressure and also there is a critical pressure for T_{CO}. In this compound, under pressure, T_{MI} only changes slightly with pressure, which may result from the robust charge ordering.

At ambient pressure, the x = 0.45 compound has smaller orthorhombic strains than $Nd_{0.5}Sr_{0.5}MnO_3$. The difference between in-plane and c-axis strain is small, indicating a more cubic structure (Figure 6.10). Under pressure, the lattice parameters of the x = 0.45 compound have different compressibility. The orthorhombic strains increase with pressure. For the x = 0.5 compound, the difference between the compressibility of lattice parameters is small. The ab-plane orthorhombic strain slightly decreases and the c-axis strain increases on pressure increase.

If we compare the resistivity of these two compounds much different, we can find a surprising similarity between the resistivity curves under pressure (Figure 6.6 and Figure 6.11). Figure 6.14 is the resistivity of these two compounds under pressure. The similarity seems to imply that they have also a similar electronic and magnetic state. The structure measurements partly justify this assumption. The orthorhombic strain of x = 0.45 is increased by pressure to almost same as that of the x = 0.5 compound at ambient pressure (Figure 6.10 and Figure 6.13). In addition, the high pressure resistivity of both of them is also similar to that of $Nd_{0.45}Sr_{0.55}MnO_3$ at ambient pressure, suggesting that pressure induces an A-type AFI phase in them in the high pressure range.

Due to the importance of thin films in applications, it will be interesting to compare

the effects or pressure and strain in thin films. The inset of Figure 6.14 is the resistivity of $Nd_{0.5}Sr_{0.5}MnO_3$ thin films of several typical thickness from Prellier *et al.*[172] With thickness decrease, the strain in thin films is regarded to increase. Compared with $Nd_{0.55}Sr_{0.45}MnO_3$, the resistivity evolution with thickness decreasing (strain increasing) is an analogy to pressure increasing in bulk $Nd_{0.55}Sr_{0.45}MnO_3$, indicating that pressure increases strain in FMM sample proved by structure measurements.

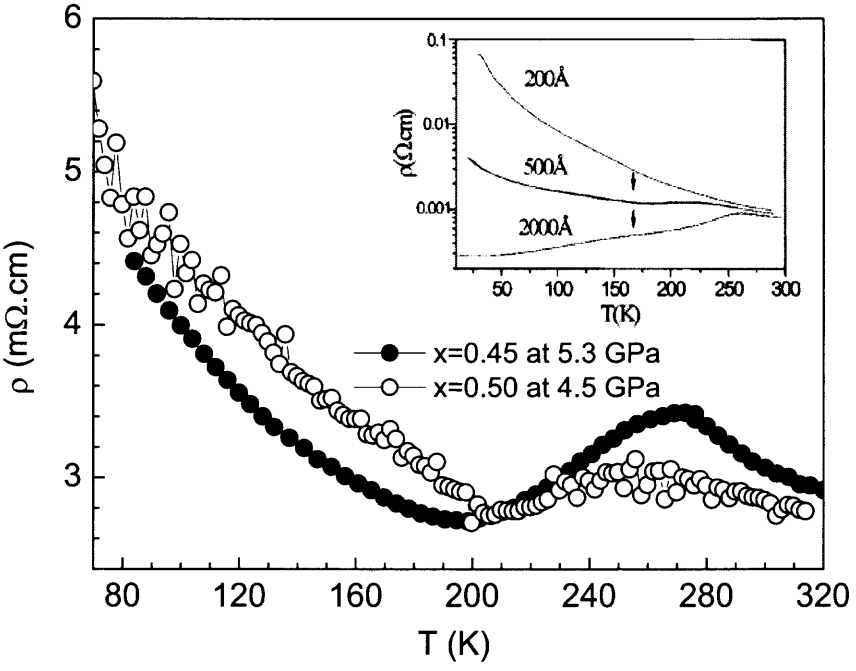

Figure 6.14 Comparison of resistivity of $Nd_{0.55}Sr_{0.45}MnO_3$ and $Nd_{0.5}Sr_{0.5}MnO_3$ under pressure.

Note: the inset is the resistivity of $Nd_{0.5}Sr_{0.5}MnO_3$ thin films with different thickness.[172]

CHAPTER 7

PRESSURE AND BANDWIDTH: SUMMARY AND FUTURE WORK

7.1 Introduction

The bandwidth W is an important parameter in manganites. It is characterized by the overlap between the Mn-3d orbital and O-2p orbitals. In perovskite compounds ABX_3, it can be described empirically by equation (2.1). In double exchange theory, it is described as the electron hopping rate or the transfer integral [equation (1.3)].

In manganites, the Mn 3d orbital is split into t_{2g} and e_g orbitals by the octahedra crystal field. The conduction is mediated by the e_g electrons. Because the e_g orbital is Jahn-Teller active, Jahn-Teller distortion can further split the two-fold degenerate e_g orbital to trap the electron. So the bandwidth is correlated with the local atomic structure of MnO_6 octahedra: cooperative tilting (Mn-O-Mn bond angle), Jahn-Teller distortion (Mn-O distances) and coherence of JTD.

Two ways to modify the structures are chemical doping and high pressure. In chemical doping, by selecting different doping elements and doping concentration, the average A-site atom size $\langle r_A \rangle$ is changed, because of the mismatch between $\langle r_A \rangle$ and Mn-site ion size, the local atomic structure of MnO_6 octahedra is modified. Therefore, the bandwidth is tuned by chemical doping so that complicated electronic and magnetic phase diagrams are induced. High pressure only modifies lattice structure, without inducing chemical complexity.

Currently, most of the high pressure studies on manganites are on metal-insulator transitions. In the low pressure range, this electronic transition is coupled to the ferromagnetic transition, which can be explained qualitatively by double exchange theory.[143,144] In CMR manganites, the metal-insulator transition occurs in two cases: low temperature metallic ground state in some doping system at certain doping

concentrations, such as: $La_{1-x}Sr_xMnO_3$ (x~0.16-0.50), $La_{1-x}Ca_xMnO_3$ (x~0.18-0.50), $Nd_{1-x}Sr_xMnO_3$ (x~0.25-0.50); induced metallic state by other factors, such as magnetic field, photons, pressure, etc., a typical is $Pr_{0.7}Ca_{0.3}MnO_3$.

In low pressure range, it is found that hydrostatic pressure has similar effect to chemical doping with larger atom and higher doping concentration. Both increase the Mn-O-Mn bond angle, compresse the Mn-O bond length and hence, lead to larger bandwidth W. Because T_C (or T_{MI}) is approximately proportional to W, T_C (or T_{MI}) increases correspondingly, or in some manganites insulating, a metal-insulator transition can be induced. The effect of chemical doping and pressure can be correlated with a conversion factor $3.75x10^{-4}$ Å/kbar. With this conversion factor, the effect of pressure and chemical doping can be mapped into one phase diagram (Figure 2.6).

By studying effect of pressure on the metal-insulator transition of several manganites, we have found that T_C and T_{MI} do not change monotonically with pressure and these two transitions do not always couple. On the other hand, pressure induces complicated spin, charge and lattice state changes.

7.2 Pressure Effects on Metal-Insulator Transition

In all the samples studied, there is a metal-insulator transition or such a transition can be induced by pressure. Corresponding to the bandwidth phase diagram (Figure 2.6), the $Nd_{1-x}Sr_xMnO_3$ (x = 0.45, 0.50) system has large bandwidth; $La_{0.60}Y_{0.07}Ca_{0.33}MnO_3$ has medium bandwidth; $Pr_{1-x}Ca_xMnO_3$ (x = 0.25, 0.30, 0.35) system has small bandwidth.

In Table 7.1, the $\langle r_A \rangle$, tolerance factor t and metal-insulator transition temperature, which correspond to the bandwidth, are listed. The average Mn-O bond length and Mn-O-Mn bond angle of all samples are plotted in Figure 7.1. According to equation (2.1), with increasing $\langle r_A \rangle$ or t, the decreasing bond length and increasing bond angle lead to increasing bandwidth W and hence, increasing T_{MI}.

Table 7.1 Average A-site Ion Size, Tolerance Factor, T_{MI}, dT_{MI}/dP, and Critical Pressure

Sample	$\langle r_A \rangle$ (Å)	t	T_{MI} (K)	dT_{MI}/dP (K/GPa)	P* (GPa)
Pcmo25	1.17925	0.92711	0	54(14)	3.8
Pcmo30	1.17930	0.92830	0	88(7)	3.6
Pcmo35	1.17935	0.92950	0	67(7)	3.9
Lycmo	1.20230	0.93730	148.8	22(4)	3.8
Nsmo45	1.22915	0.94987	290.8	18(11)	2.6
Nsmo50	1.23650	0.95374	255.8	N/A	3.1

Note: t is the tolerance factor calculated with the data in ref. 107; T_{MI} is the metal-insulator transition temperature at ambient pressure; dT_{MI}/dP is extracted by fitting the data with a third-order polynomial, the numbers in brackets are the fitting error; P* is the pressure where the T_{MI} increase trend reverses.

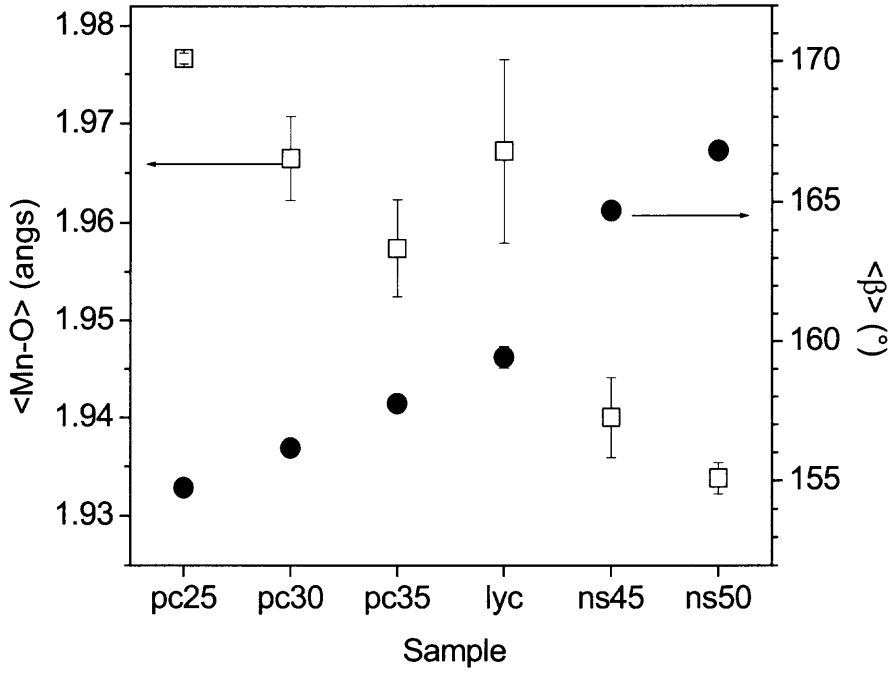

Figure 7.1 Mn-O bond length and Mn-O-Mn bond angle of samples at ambient conditions.

Note: the abscissa is samples: the numbers indicated the concentration of the doping element; p represents Pr, c represents Ca, l represents La, y represents Y, n represents Nd, s represents Sr.

In the small bandwidth system $Pr_{1-x}Ca_xMnO_3$ system, all three samples are insulating. Under pressure, metal-insulator transitions are induced. With pressure increase, the behavior of T_{MI} is similar to other samples with larger bandwidth. The pressure dependence of T_{MI} of all samples is plotted together in Figure 7.2.

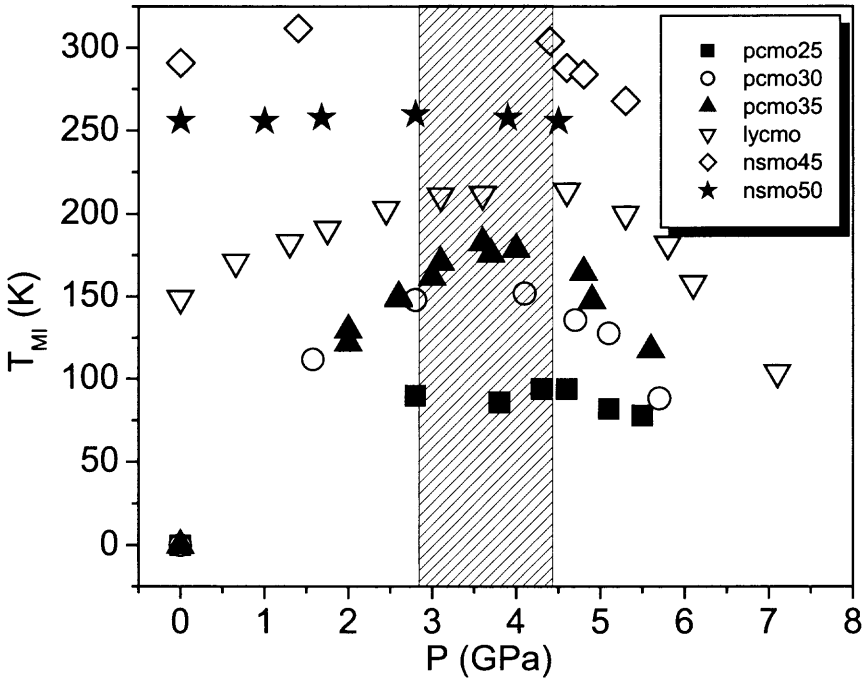

Figure 7.2 Pressure dependence of metal-insulator transition temperatures of $Nd_{1-x}Sr_xMnO_3$ (x = 0.45, 0.50); $La_{0.60}Y_{0.07}Ca_{0.33}MnO_3$; $Pr_{1-x}Ca_xMnO_3$ (x = 0.25, 0.30, 0.35).

In Figure 7.2, the most salient feature is that a critical pressure P* exist in each sample: with pressure increase, below P*, T_{MI} increases; above P*, T_{MI} decreases. By fitting T_{MI} *vs.* P plots with a third-order polynomial, P* for each sample is extracted and listed in Table 7.1. Due to the accuracy, if all the samples have same P* cannot be determined yet at present. By looking at the plots, if the P* is different, this difference is small.

In large bandwidth samples, T_{MI} change with pressure is slower than small bandwidth ones, indicating more stability under pressure. The samples studied are selected with different doping concentration and from different doping systems. The

bandwidth spans a large range. Therefore, the samples also have much different ground electronic and magnetic properties in ambient environment. But the metal-insulator transitions in these samples all follow a similar behavior, so it is reasonable to speculate that the critical pressure P* is universal for the metal-insulator transitions in manganites. From the structure measurements to $La_{0.60}Y_{0.07}Ca_{0.33}MnO_3$ and $Pr_{1-x}Ca_xMnO_3$ system, the behavior of T_{MI} under pressure could be mostly ascribed to a local atomic structure transformation of the MnO_6 octahedra.

Under pressure, the smaller bandwidth samples have smaller pressure range in which the sample is metallic in low temperature and outside which they are insulating. On the other hand, the samples with large bandwidth is more stable under pressure and the variable range of T_{MI} is small and they do not become insulating in a larger pressure range. The less stability of T_{MI} in small bandwidth samples may come from the small A-site atoms, which leave more space between octahedra for them to rotate - accordingly, a smaller pressure window for the ferromagnetic metallic state.

A less interesting feature in Figure 7.2 is that larger bandwidth samples always have a higher T_{MI}. The only exception is that in the $Nd_{1-x}Sr_xMnO_3$ system, the $x = 0.5$ compound nominally has a larger bandwidth than the $x = 0.45$ compound but has lower T_{MI}. This possibly results from the strong charge ordering effect.

The other interesting thing is the dT_{MI}/dP at $P = 0$ GPa. The value of dT_{MI}/dP extracted from the third-order polynomial fitting results are listed in Table 7.1. Clearly, the smaller the bandwidth, the larger dT_{MI}/dP, indicating that the local structure of smaller bandwidth sample is more distorted and has relatively large degree distortion to be suppressed by pressure.

7.3 Metal-Insulator Transition and Curie Temperature Coupling under Pressure

In some low pressure (below ~2 GPa) studies, it was shown that the FM state and metallic state are coupled, which was explained qualitatively by double exchange theory.[143,144] At higher pressure, the question if the FM state and the metallic state are still coupled is unanswered. Two methods could be used to determine it: high pressure magnetic measurement and high pressure neutron scattering. But both methods are extremely difficult in high pressure range. Therefore, this question has been untouched up to date. Fortunately, in our samples, the small bandwidth $Pr_{1-x}Ca_xMnO_3$ samples are semiconductor in paramagnetic phase. Corresponding to the magnetic transition, there is a reduction of activation energy. The Curie temperature can be extracted through the temperature dependence of the activation energy. By doing high pressure resistivity measurement, both electronic and magnetic transitions can be explored.

In $Pr_{0.75}Ca_{0.25}MnO_3$, T_C and T_{MI} are decoupled, and never coincide in the measured pressure range (Figure 5.8). T_C and T_{MI} have different behavior under pressure. With pressure increase, T_C decreases and T_{MI} increases below P*; above P*, T_C increases and T_{MI} decreases. At P*, the difference between T_{MI} and T_C is the smallest. In $Pr_{0.7}Ca_{0.3}MnO_3$, between ~0.8-5 GPa, T_C and T_{MI} are coupled; outside this range, T_C and T_{MI} are decoupled (Figure 5.12). For $Pr_{0.65}Ca_{0.35}MnO_3$, because of the data quality, T_C cannot be determined. From the E_g plots, it seems that T_C and T_{MI} are coupled when the metallic state present (Figure 5.19).

The behavior of T_C and T_{MI} under pressure reveals that bandwidth mediates the relation between T_C and T_{MI}. From above, conclusions can be drawn: if the bandwidth is not large enough, T_C and T_{MI} will not be coupled even under pressure; only in large bandwidth materials, can T_C and T_{MI} possibly be coupled; for materials with critical bandwidth, there is an optimum pressure range in which T_C and T_{MI} are coupled. As shown in chapter 5, the decoupled T_C and T_{MI} could be ascribed to the competition between DE and SE interactions between Mn ions, both are a function of bandwidth.

7.4 Charge Ordering under Pressure

From $Pr_{1-x}Ca_xMnO_3$ system and $Nd_{0.5}Sr_{0.5}MnO_3$, the pressure effect on charge ordering was observed:

In all the three $Pr_{1-x}Ca_xMnO_3$ samples, below T_C, CO is completely suppressed and the material is in FM and/or metallic state. Between the temperature above T_C and T_{CO}, CO is gradually suppressed with pressure increase (Figure 5.9, Figure 5.14, and Figure 5.19). Above a critical pressure P*, instead of CO, an electronic state with unknown conducting mechanism arises. In this system, T_{CO} decreases monotonically with pressure until CO disappears. In all three samples, orthorhombic strains decrease with pressure.

In $Nd_{0.5}Sr_{0.5}MnO_3$, CO has a different behavior, it seems that T_{CO} increases with pressure while the resistivity of the CO state decrease. The high pressure structure measurement indicates that the c-axis orthorhombic strain increases and ab-plane strain decreases with pressure. The structure measurements and comparison with the resistivity of the x = 0.45 and 0.55 compound imply that the CE-type antiferromagnetic state is destroyed, and possibly an A-type antiferromagnetic state is induced.

7.5 Structure under Pressure

In manganites, the local atomic structure of the MnO_6 octahedra is crucial to their various properties. To explain the electron transport results, high pressure measurements of both crystal lattice and magnetic structures are necessary. Neutron diffraction is ideal, which can measure both lattice and magnetic structures. But it requires large amount sample, which limits its use in higher pressure ranges. The other one practical method is x-ray diffraction. It also has many disadvantages: to penetrate the diamond anvils and to shine on sample, high energy, high intensity and focused synchrotron radiation x-ray beam ($\sim 50\times 50\mu m^2$) is needed; because of the small amount sample ($<200\times 200\times 50\mu m^3$), the detector counting time is very long and signal is noisy. The most serious problem is that

because of the very high x-ray energy (>30 keV), the scattering cross section of oxygen is small so that the error of oxygen positions is large.

With the present structure data, it seems that a local atomic structure transformation happens at the critical pressure P*. This transformation can partly explain the non-monotonic behavior of the metal-insulator transition behavior. In addition to the MnO_6 octahedra, orthorhombic strains are also changed under pressure, which may contribute to the electronic and magnetic properties change. In the PCMO system, it was found that the orthorhombic strains of all three samples decrease under pressure. In NSMO system, the strains in $Nd_{0.55}Sr_{0.45}MnO_3$ increase with pressure, which may be correlated to the insulating trend of resistivity; in $Nd_{0.5}Sr_{0.5}MnO_3$, the c-axis strain increases and ab-plane strain decreases slightly with pressure.

7.6 Future Work

As highly correlated electron system, the various properties of manganites are sensitive to changes in charge, spin, orbital and lattice states and interactions between them. Through high pressure electron transport measurements, it has been shown that pressure induces far more complicated electronic and magnetic state changes than in the low pressure range. To understand these effects, more explorations are necessary of both experimental and theoretical aspects.

The electron transport measurements imply that through lattice modification, spin states are correspondingly changed. So magnetic measurements, for example, high pressure susceptibility measurement, are useful to determine the spin states. For different doping systems, the spin structures are much different. So is it under pressure. Neutron diffraction will contribute to observe the evolution of spin structure under pressure.

Because of the strong coupling to lattice structure, especially the local structure of MnO_6 octahedra, structure measurements are desired. For high pressure measurements,

because of small scattering cross section of oxygen in x-ray diffraction and large amount sample requirement in neutron diffraction, more advanced high pressure techniques and better experiment conditions are needed. At present, high pressure Raman scattering seems practical. With Raman scattering measurements, the Jahn-Teller distortion and vibration of the octahedra can be determined.

Due to the importance of electronic structure, high pressure electronic structure investigation is desired. High pressure x-ray absorption spectroscopy is a useful tool although sophisticated experimental skill and instruments are required.

Most of the present high pressure studies are on hydrostatic pressure. But many applications require the material to be in thin film state. To study the lattice effects in thin films, uniaxial pressure studies on single crystal and hydrostatic pressure studies on thin films will provide useful information for applications.

In the theoretical aspect, band structure calculation is necessary to understand the high pressure electron transport results. In the calculation, lattice structure, spin structure and orbital structure changes need to be considered simultaneously.

In summary, the high pressure study on electron transport and structure has shown that high pressure can induce complicated electronic and magnetic property changes. Pressure is not equivalent to chemical doping except in a small low pressure range. Our work is just a start. Much more work needs to be done to understand this complicated correlated system. The high pressure study will also provide useful information in device fabrication in which the material is in the thin film state with high anisotropic strain.

REFERENCES

[1] G. H. Jonker and J. H. Van Santen, Physica **16**, 337 (1950).

[2] E. O. Wollan and W. C. Koehler, Phys. Rev. **100**, 545 (1955).

[3] J. Volger, Physica **20**, 49 (1954).

[4] R. von Helmolt, J. Wecker and B. Holzapfel *et al.*, Phys. Rev. Lett. **71**, 2331 (1993).

[5] S. Jin, T. H. Tiefel, and M. McCormack *et al.*, Science **264**, 413 (1994).

[6] T. Venkatesan, M. Rajeswari, and Z. Dong *et al.*, Phil. Trans. A **356**, 1661 (1998).

[7] W. Prellier, Ph. Lecoeur, and B. Mercey, J. of Phys.: Condens. Matter **13**, R915 (2001).

[8] Paul P. Donohue, Rex Watton, and Michael A. Todd *et al.*, Proceedings of SPIE, **4650**, 234 (2002).

[9] Yu. P. Sukhorukov, E. A. Can'shina, and B. I. Belevtsev *et al.*, J. Appl. Phys. **91**, 4403 (2002).

[10] Y. Sekiguchi, Y. Teramoto, and R. Fujiwara. Jpn. Kokai Tokkyo Koho, Patent number: JP 2001345496, 6 (2001).

[11] Youwei Du, Zaibing Guo, and He Huang *et al.*, Faming Zhuanli Shenqing Gongkai Shuomingshu, Patent number: CN 1170749, 5 (1998).

[12] V. A. Vas'ko, V. A. Larkin, and P. A. Kraus *et al.*, Phys. Rev. Lett. **78**, 1134 (1997).

[13] S. Jin, H. M. O'Bryan, and T. H. Tiefel *et al.*, Appl. Phys. Lett. **66**, 382 (1995).

[14] P. Grünberg, R. Schreiber, and Y. Pang *et al.*, Phys. Rev. Lett. **57**, 2442 (1986).

[15] Y. Tokura and Y. Tomioka, J. of Magn. and Magn. Mat. **200**, 1 (1999).

[16] A. P. Ramirez, J. Phys.: Condens. Matter **9**, 8171 (1997).

[17] E. L. Nagaev, Phys. Reports **346**, 387 (2001).

[18] J. M. D. Coey, M. Viret, and S. von Molnár, Advances in Phys. **48**, 167 (1999).

[19] J. F. Mitchell, D. N. Argyriou, and J. D. Jorgensen, *Colossal Magnetoresistive Oxides*, Yoshinori Tokura (ed.), Gordon and Breach Science Publishers, 187 (2000).

[20] M. N. Baibich, J. M. Broto, and A. Fert *et al.*, Phys. Rev. Lett. **61**, 2472 (1988).

[21] J. Rodríguez-Carvajal, M. Hennion, and F. Moussa *et al.*, Phys. Rev. B **57**, R3189 (1998).

[22] F. Moussa, M. Hennion, and J. Rodríguez-Carvajal *et al.*, Phys. Rev. B **54**, 15149 (1996).

[23] C. N. R. Rao and A.K. Raychaudhuri, *Colossal magnetoresistance, charge ordering and related properties of manganese oxides*, C.N.R. Rao and B. Raveau (ed.), World Scientific, 1998.

[24] S. Satpathy, Zoran S. Popović, and Filip R. Vukajlović, Phys. Rev. Lett. **76**, 960 (1996); J. Appl. Phys. **79**, 4555 (1996).

[25] A. Fujimori, T. Mizokawa, and T. Saitoh, *Colossal magnetoresistance, charge ordering and related properties of manganese oxides*, C.N.R. Rao and B. Raveau (ed.), World Scientific, 1998.

[26] Y. Okimoto, T. Katsufuji, and Y. Okada *et al.*, Phys. Rev. B **51**, 9581 (1995).

[27] H. Y. Hwang, S-W. Cheong, and P. G. Radaelli *et al.*, Phys. Rev. Lett. **75**, 914 (1995).

[28] P. Schiffer, A. P. Ramirez, and W. Bao *et al.*, Phys. Rev. Lett. **75**, 3336 (1995).

[29] Y. Moritomo, A. Asamitsu, and Y. Tokura, Phys. Rev. B **51**, 16491 (1995).

[30] A. Urushibara, Y. Moritomo, and A. Arima *et al.*, Phys. Rev. B **51**, 14103 (1995).

[31] H. Kuwahara, Y. Tomioka, and A. Asamitsu *et al.*, Science **270**, 961 (1995).

[32] Y. Tomioka, A. Asamitsu, and H. Kuwahara *et al.*, Phys. Rev. B **53**, 1689 (1996).

[33] A. Asamitsu, Y. Moritomo, and Y. Tomioka *et al.*, Nature (London) **373**, 407 (1995).

[34] C. Zener, Phys. Rev. **82**, 403 (1951).

[35] P. W. Aderson and H. Hasegawa, Phys. Rev. **100**, 675 (1955).

[36] P.-G. de Gennes, Phys. Rev. **118**, 141 (1960).

[37] A. J. Millis, P. B. Littlewood, and B. I. Sharaiman, Phys. Rev. Lett. **74**, 5144 (1995).

[38] A. J. Millis, B. I. Shraiman, and R. Mueller, Phys. Rev. Lett. **77**, 175 (1996).

[39] A. J. Millis, Phys. Rev. B **53**, 8434 (1996).

[40] A. J. Millis, R. Mueller, and B. I. Shraiman, Phys. Rev. B **54**, 5389 (1996).

[41] A. J. Millis, R. Mueller, and B. I. Shraiman, Phys. Rev. B **54**, 5405 (1996).

[42] H. A. Kramers, Physica **1**, 182 (1934).

[43] J. Kanamori, J. Phys. Chem. Solids **10**, 87 (1959).

[44] T. Nagamiya, *State of Atoms in Magnetic Crystals*, Cofference of Welsh Foundation, December, 1958.

[45] E. O. Wollan, H. R. Child, and W. C. Koehler *et al.*, Phys. Rev. **112**, 1132 (1958).

[46] J. B. Goodenough, J. Phys. Chem. Solids **6**, 287 (1958).

[47] P. W. Anderson, Phys. Rev. **115**, 2 (1959).

[48] J. B. Goodenough, Phys. Rev. **100**, 564 (1955).

[49] R. R. Heikes, Phys. Rev. **99**, 1232 (1955).

[50] J. B. Goodenough, A. Wold, R. J. Arnott, and N. Menyuk, Phys. Rev. **124**, 373 (1961).

[51] J. B. Goodenough, Phys. Rev. **171**, 466 (1968).

[52] J. B. Goodenough, J. App. Phys. **81**, 5330 (1997).

[53] G. Jackeli, N. B. Perkins, and N. M. Plakida, Phys. Rev. B **62**, 372 (2000).

[54] O. N. Mryasov, R. F. Sabiryanov, A. J. Freeman, and S. S. Jaswal, Phys. Rev. **56**, 7255 (1997).

[55] A. K. Heilman, Y. Y. Xue, and B. Lorenz *et al.* Phys. Rev. B **65**, 214423 (2002).

[56] M. Paraskevopoulos, F. Mayr, and C. Hartinger *et al.*, J. of Magn. and Magn. Mat. **211**, 118 (2000).

[57] H. Nojiri, K. Kaneko, and M. Motokawa *et al.*, Phys. Rev. B **60**, 4142 (1999).

[58] R. V. Krishnan and A. Banerjee, J. Phys.: Condens. Matter **12,** 7887 (2000).

[59] C. H. Chen and S-W. Cheong, Phys. Rev. Lett. **76**, 4042 (1996).

[60] S-W Cheong and C. H. Chen, *Colossal magnetoresistance, charge ordering and related properties of manganese oxides*, C. N. R. Rao and B. Raveau (ed.). World Scientific, 1998.

[61] C. N. R. Rao, Anthony Arulraj, A. K. Cheetham, and Bernard Raveau, J. Phys.: Condens. Matter **12**, R83 (2000).

[62] J. Fontcuberta, V. Laukhin, and X. Obradors, Phys. Rev. B **60**, 6266 (1999).

[63] T. Okuda, T. Kimura, and H. Kuwahara *et al.*, Mater. Sci. and Engin. B **63**, 163 (1999).

[64] R. Maezono, S. Ishihara, and N. Nagaosa, Phys. Rev. B **57**, R13993 (1998).

[65] A. J. Millis, Phys. Rev. B **55**, 6405 (1997).

[66] K. H. Ahn and A. J. Millis, Phys. Rev. B **58**, 3697 (1998).

[67] Y. Tokura and N. Nagaosa, Science **288**, 462 (2000).

[68] E. Saitoh, S. Okamoto, and K. T. Takahashi *et al.*, Nature (London) **410**, 180 (2001).

[69] K. Terakura, J. Lee, and J. Yu *et al.*, Mater. Sci. and Engin. B **63**, 11 (1999).

[70] Z. Popovic and S. Satpathy, Phys. Rev. Lett. **88**, 197201 (2002).

[71] Andrzej M. Oleś and Louis Felix Feiner, Lecture Notes in Phys. **580**, 226 (2001); Phys. Rev. B **65**, 052414 (2002).

[72] Jan Bała and Andrzej M. Oleś, Phys. Rev. B **62**, R6085 (2000).

[73] S. Okamoto, S. Ishihara, and S. Maekawa, Phys. Rev. B **61**, 14647 (2000).

[74] Zhenghuang Shu, Jinming Dong, and D. Y. Xing, Phys. Rev. Lett. **86**, 6049 (2001).

[75] Y. Murakami, J. P. Hill, and D. Gibbs *et al.*, Phys. Rev. Lett. **81**, 582 (1998).

[76] H. Kuwahara, T. Okuda, and Y. Tomioka *et al.*, Phys. Rev. Lett. **82**, 4316 (1999).

[77] Bas B. Van Aken, Auke Meetsma, and Y. Tomioka *et al.*, Phys. Rev. Lett. **90**, 066403 (2003).

[78] M. von Zimmermann, C. S. Nelson, and J. P. Hill *et al.*, Phys. Rev. B **64**, 195133 (2001).

[79] M. von Zimmermann, J. P. Hill, and Doon Gibbs *et al.*, Phys. Rev. Lett. **83**, 4872 (1999).

[80] I. Loa, P. Adler, and A. Grzechnik *et al.*, Phys. Rev. Lett. **87**, 125501 (2001).

[81] T. Ishikawa, K. Ookura, and Y. Tokura Phys. Rev. B **59**, 8367 (1999).

[82] A. Shiraga, M. Milyaev, and H. Honda *et al.*, Physical Review B **66**, 052412 (2002).

[83] Masaki Takata, Eiji Nishibori, and Kenichi Kato *et al.*, J. of Phys. Soc. of Japan **68**, 2190 (1999).

[84] S. Ishihara and S. Maekawa, Phys. Rev. Lett. **80**, 3799 (1998).

[85] Sumio Ishihara and Sadamichi Maekawa, Theory of anomalous x-ray scattering in a variety of orbital ordered manganites. *Physics and Chemistry of Transition Metal Oxides*, H. Fukuyama and N. Nagaosa (ed.), Springer Verlag, Berlin, 125, 84-94 (1999).

[86] P. D. Hatton, S. B. Wilkins, and P. D. Spencer *et al.*, International J. of Modern Phys. B **16**, 1661 (2002).

[87] K. Nakamura, T. Arima, and A. Nakazawa *et al.*, Phys. Rev. B **60**, 2425 (1999).

[88] B. Jiang, J. M. Zuo, and Q. Chen *et al.*, Acta Crystallographica A **58**, 4 (2002).

[89] A. J. Millis, Nature (London) **392**, 147 (1998).

[90] H. Röder, J. Zhang, and A. R. Bishop, Phys. Rev. Lett. **76**, 1356 (1996).

[91] M. R. Ibarra, P. A. Algarabel, and C. Marquina *et al.*, Phys. Rev. Lett. **75**, 3541 (1995).

[92] D. Emin and M. -N. Bussac, Phys. Rev. B **49**, 14290 (1994).

[93] M. Jaime, M. B. Salamon, and Rubinstein *et al.*, Phys. Rev. B **54**, 11914 (1996).

[94] D. Emin, Phys. Rev. B **48**, 13691 (1993).

[95] Michael Ziese and Chatchai Srinitiwarawong, Phys. Rev. B **58**, 11519 (1998).

[96] J. Chatterjee, M. Mitra, and A. N. Das, Euro. Phys. J. B **18**, 573 (2000).

[97] J. -S. Zhou, J. B. Goodenough, A. Asamitsu, and Y. Tokura, Phys. Rev. Lett. **79**, 3234 (1997).

[98] S. J. L. Billinge, R. G. DiFrancesco, and G. H. Kwei, *et al.*, Phys. Rev. Lett. **77**, 715 (1996).

[99] T. A. Tyson, J. Mustre de Leon, and S. D. Conradson *et al.* Phys. Rev. B **53**, 13985 (1996).

[100] J. M. De Teresa, M. R. Ibarra, and J. Blasco *et al.*, Phys. Rev. B **54**, 1187 (1996).

[101] J. M. De Teresa, M.R. Ibarra, and P. A. Algarabel *et al.*, Nature (London) **386**, 256 (1997).

[102] J. M. De Teresa, K. Dörr, and K. H. Müller *et al.*, Phys. Rev. B **58**, R5928 (1998).

[103] A. J. Millis, *Colossal Magnetoresistive Oxides*, Yoshinori Tokura (ed.), Gorden and Breach Science Publishers, (2000).

[104] K. H. Kim, J. H. Jung, and T. W. Noh, J. of the Korean Phys. Soc. **32**, S1832 (1998).

[105] A. Lanzara, N. L. Saini, and M. Brunelli *et al.*, J. of Phys. and Chem. of Solids **59**, 2220 (1998); Phys. Rev. Lett. **81**, 878 (1998).

[106] S. Yoon, H. L. Liu, and G. Schollerer *et al.*, Phys. Rev. B **58**, 2795 (1998).

[107] R. D. Shannon and C. T. Prewitt, Acta crystallogr. A **32**, 785 (1976).

[108] H. A. Jahn and E. Teller, Proc. Roy. Soc. (London) A **161**, 220 (1937); Phys. Rev. **49**, 874 (1936).

[109] J. B. Goodenough, *Magnetism and the Chemical Bond*, John Wiley and Sons, New York, 1963.

[110] Joachim Deisenhofer, Michalis Paraskevopoulos, Hans-Albrecht Krug von Nidda, and Alois Loidl, Phys. Rev. B **66**, 054414 (2002).

[111] L. E. Gontchar, A. E. Nikiforov, and S. E. Popov, *AIP Conference Proceedings* **554** (Physics in Local Lattice Distortions), 403 (2001); J. of Magn. and Magn. Mat. **223**, 175 (2001); NATO Science Series II: Math., Phys. and Chem. **39**, 307 (2001).

[112] S. Fratini, M. Capone, M. Grilli, and D. Feinberg, *AIP Conference Proceedings*, **554** (Physics in Local Lattice Distortions), 371 (2001).

[113] Michael D. Kaplan and George O. Zimmerman, NATO Science Series II: Math., Phys. and Chem. **39**, 277 (2001).

[114] J. L. García–Muñoz, M. Suaaidi, and J. Fontcuberta *et al.*, Phys. Rev. B **55**, 34 (1997).

[115] P. G. Radaelli, M. Marezio, and H. Y. Hwang *et al.*, Phys. Rev. B **54**, 8992 (1996).

[116] V. Kiryakhin, Y. J. Wang, and F. C. Chou *et al.*, Phys. Rev. B **59**, R6581 (1999).

[117] J. -S. Zhou, W. Archibald, and J. B. Goodenough, Phys. Rev. B **57**, R2017 (1998).

[118] K. Khazeni, Y. X. Jia, and V. H. Crespi *et al.*, J. Phys.: Condens. Matter **8**, 7723 (1996).

[119] N. -C. Yeh, R. Vasquez, and D. Beam *et al.*, J. Phys.: Condens. Matter **9**, 3713 (1996).

[120] N. -C. Yeh, R. Vasquez, and J. Y. Wei *et al.*, *Proceedings of Materials Research Society Meeting*, San Francisco, California (Pittsburgh Pennsylvania: Materials Research Society), 145 (1997).

[121] G. J. Snyder, R. Hiskes, and S. DiCarolis *et al.*, Phys. Rev. B **53**, 14434 (1996).

[122] M. Jaimìe, P. Lin, and M. B. Salamon *et al.*, Phys. Rev. B **58**, R5901 (1998).

[123] T. Okuda, A. Asamitsu, and Y. Tomioka *et al.* Phys. Rev. Lett. **81**, 3203 (1998).

[124] J. M. D. Coey, M. Viret, and L. Ranno *et al.*, Phys. Rev. Lett. **75**, 3910 (1995).

[125] M. B. Salamon and M. Jaime, Rev. of Mod. Phys. **73**, 583 (2001).

[126] J. H. Park, C. T. Chen, and S. -W. Cheong *et al.*, Phys. Rev. Lett. **76**, 4215 (1996).

[127] M. F. Hundley, M. Hawley, and R. H. Heffner *et al.*, Appl. Phys. Lett. **67**, 860 (1995).

[128] J. D. Lee and B. I. Min, Phys. Rev. B **55**, 12454 (1997).

[129] T. T. M. Palstra, A. P. Ramirez, and S-W. Cheong *et al.*, Phys. Rev. B **56**, 5104 (1997).

[130] G. Jakob, W. Westerburg, F. Martin, and H. Adrian, Phys. Rev. B **58**, 14966 (1998).

[131] N. F. Mott and E. Davies, *Electronic Processes in Noncrystalline Materials*, Oxford University Press, 1971.

[132] L. Sheng, D. Y. Xing, D. N. Sheng, and C. S. Ting, Phys. Rev. Lett. **79**, 1710 (1997).

[133] C. M. Varma, Phys. Rev. B **54**, 7328 (1996).

[134] M. Viret, L. Ranno, and J. M. D. Coey, Phys. Rev. B **55**, 8067 (1997).

[135] M. Viret, L. Ranno, and J. M. D. Coey, J. Appl. Phys. **81**, 4964 (1997).

[136] G. P. Triberis and L. R. Friedman, J. Phys. C **18**, 2281 (1985).

[137] J. Z. Sun, L. Krusin-Elbaum, and A. Gupta *et al.*, Appl. Phys. Lett. **69**, 1002 (1996).

[138] V. V. Struzhkin, R. J. Hamley, H. K. Mao, and Y. A. Timofeev, Nature (London) **390**, 382 (1997); V. V. Struzhkin, R. J. Hamley, and H. K. Mao *et al.*, Hyperfine Interact. **128**, 323 (2000); E. Gregoryanz, V. V. Struzhkin, and R. J. Hamley *et al.*, Phys. Rev. B **65**, 064504 (2002).

[139] H. Olijnyk and W. B. Holzapfel, J. Phys. (Paris) **45**, C8-153 (1984).

[140] K. J. Chang, Michel M. Dacorogna, and Marvin L. Cohen *et al.*, Phys. Rev. Lett. **54**, 2375 (1985).

[141] L. Gao, Y. Y. Xue, and F. Chen *et al.*, Phys. Rev. B **50**, 4260 (1994).

[142] M. Medarde, J. Mesot, and P. Lacorre *et al.*, Phys. Rev. B **52**, 9248 (1995).

[143] J. J. Neumeier, M. F. Hundley, J. D. Thompson, and R. H. Heffner, Phys. Rev. B **52**, R7006 (1995).

[144] Y. Moritomo, H. Kuwahara, and Y. Tomika *et al.*, Phys. Rev. B **55**, 7549 (1997).

[145] V. Laukhin, J. Fontcuberta, and J. L. Garcia-Munoz *et al.*, Phys. Rev. B **56**, 10009 (1997).

[146] Z. Arnold, K. Kamenev, and M.R. Ibarra *et al.*, Appl. Phys. Lett. **67**, 2875 (1995).

[147] R. Senis, L. Balcells, and V. Laukhin *et al.*, J. of Appl. Phys. **87**, 5609 (2000).

[148] V. G. Tissen, E. G. Ponyatovskii, and M. V. Nefedova *et al.*, J of Magn. and Magn. Mat. **211**, 145 (2000).

[149] V. Markovich, E. Rozenberg, and G. Gorodetsky *et al.*, Phys. Rev. B **63**, 054423 (2001).

[150] Y. Moritomo, A. Asamitsu, and Y. Tokura, Phys. Rev. B **56**, 12190 (1997).

[151] J. Fontcuberta, V. Laukhin, and X. Obradors, Appl. Phys. Lett. **72**, 2607 (1998).

[152] I. S. Maksimov, E. B. Nyeanchi, and Yu. V. Medvedev *et al.*, Physica Status Solidi A **189**, 281 (2002).

[153] G. Srinivasan, T. P. Mullin, and D. Hanna *et al.* Appl. Phys. A **72**, 333 (2001).

[154] S. Jacob, T. Roch, and F. S. Razavi *et al*, J. of Appl. Phys. **91**, 2232 (2002).

[155] M. Itoh, K. Nishi, and J. D. Yu *et al.*, Phys. Rev. B **55**, 14408 (1997).

[156] V. Laukhin, B. Martinez, and J. Fontcuberta *et al.*, Phys Rev B **63**, 214417 (2001).

[157] L. Pinsard-Gaudart, J. Rodríguez-Carvajal, and A. Daoud-Aladine *et al.*, Phys. Rev. B **64**, 64426 (2001).

[158] B. Lorenz, A.K. Heilman, and Y.S. Wang *et al.*, Phys. Rev. B **63**, 144405 (2001).

[159] R. Senis, V. Laukhin, and B. Martinez *et al.*, Phys. Rev. B **57**, 14680 (1997).

[160] X. Wang, Y. W. Pan, and Q. L. Cui, Journal of Solid State Chemistry **160**, 307 (2001); Xin Wang, Qi-liang Cui, and Yue-wu Pan *et al.*, Gaoya Wuli Xuebao **15**, 60 (2001).

[161] A. Congeduti, P. Postorino, and E. Carmagno *et al.*, Phys. Rev. Lett. **86**, 1251 (2001).

[162] C. Meneghini, D. Levy, and S. Mobilio *et al.*, Phys. Rev. B **65**, 012111 (2002).

[163] M. Itoh, T. Shimura, and J.-D. Yu *et al.*, Phys. Rev. B **52**, 12522 (1995).

[164] A. Nossov, J. Pierre, and J. Beille *et al.*, European Phys. J. B **6**, 467 (1998).

[165] J. -S. Zhou, W. Archibald, and J. B. Goodenough, Nature (London) **381**, 770 (1996).

[166] N. N. Sirota and A. P. Karavai, Fiz. Tverd. Tela (Leningrad) **18**, 2666 (1976).

[167] A. S. Roy, A. Husmann, and T. F. Rosenbaum *et al.*, Phys. Rev. B **63**, 094416 (2001).

[168] Q. Qian, T. A. Tyson, and C. Dubourdieu *et al.*, Appl. Phys. Lett. **80**, 2663 (2002).

[169] A. J. Millis, T. Darling, and A. Migliori, J. App. Phys. **83**, 1588 (1998).

[170] A. J. Millis, A. Goyal, and M. Rajeswari *et al.*, unpubulished.

[171] K. H. Ahn and A. J. Millis, Physica B **312-313**, 766 (2002); Phys. Rev. B **64**, 115103 (2001).

[172] W. Prellier, A. Biswas, and M. Rajeswari *et al.*, Appl. Phys. Lett. **75**, 397 (1999).

[173] Q. Qian, T. A. Tyson, and C.-C. Kao *et al.*, Phys. Rev. **63**, 224424 (2001).

[174] S. B. Ogale, Y. H. Li, and M. Rajeswari *et al.*, J. of Appl. Phys. **87**, 4210 (2000).

[175] A. Biswas, M. Rajeswari, and R. C. Srivastava *et al.*, Phys. Rev. B **61**, 9665 (2000).

[176] A. Biswas, M. Rajeswari, and R. C. Srivastava *et al.* Phys. Rev. B **63**, 184424 (2001).

[177] J. H. Song, J.-H. Park, Y. H. Jeong, and T. Y. Koo, Physica B **312-313**, 729 (2002).

[178] Z.-H. Wang, H. Kronmüller, and O. I. Lebedev et al., Phys. Rev. B **65**, 054411 (2002)

[179] J. Zhang, H. Tanaka, and T. Kanki *et al.* Phys. Rev. B **64**, 184404 (2001).

[180] T. Kanki, H. Tanaka, and T. Kawai, Phys. Rev. B **64**, 224418 (2001).

[181] Qingshan Yuan. http://xxx.lanl.gov/pdf/cond-mat/0112480, Preprint Archive.

[182] V. Moshnyaga, S. Klimm, and E. Gommert *et al.*, J of Appl. Phys. **88**, 5305 (2000).

[183] P.G. Radaelli, G. Iannone, and M. Marezio *et al.*, Phys. Rev. B **56**, 8265 (1997).

[184] Y. Tokura, H. Kuwahara, and Y. Moritomo *et al.*, Phys. Rev. Lett. **76**, 3184 (1996).

[185] H. Y. Hwang, T. T. M. Palstra, S- W. Cheong, and B. Batlogg, Phys. Rev. B **52**, 15046 (1995).

[186] Arthur L. Ruoff, Hui Xia, and Qing Xia, Rev. of Sci. Instru. **63**, 4342 (1992).

[187] A. Jayaraman, Rev. of Modern Phys. **55**, 65 (1983).

[188] M. Eremets, *High Pressure Experimental Methods*, Oxford Science Publications, 1996.

[189] A. Jayaraman, Rev. of Sci. Instrum. **57**, 1013 (1986).

[190] D. J. Dunstan and I. L. Spain, J. Phys. E: Sci. Instrum. **22**, 913 (1989).

[191] I. L. Spain and D. J. Dunstan, J. Phys. E: Sci. Instrum. **22**, 923 (1989).

[192] H. K. Mao, J. Xu, and P. M. Bell, J. Gerophys. Res. **91,** 4673 (1986).

[193] K. A. Goettel, H. K. Mao, and P. M. Bell, Rev. Sci. Instrum **56**, 1420 (1985).

[194] B. Birang, B. DiBartolo, and R. C. Powell, J. Appl. Phys. **38**, 5113 (1967).

[195] R. C. Powell, B. DiBartolo, B. Birang, and C. S. Naiman, J. Appl. Phys. **37**, 4973 (1966).

[196] J. Yen and M. Nicol, J. Appl. Phys. **72**, 5535 (1992).

[197] S. L. Wunder and P. E. Schoen, J. Appl. Phys. **52**, 3772 (1981).

[198] S. Rekhi, L. S. Dubrovinsky, and S. K. Saxena, High Temperatures - High Pressures **31**, 299 (1999).

[199] K. Nakano, Y. Akahama, Y. Ohishi, and H. Kawamura, Japan. J. of Appl. Phys. **39**, 1249 (2000).

[200] L. -W. Xu, R. - Z. Che, and C. -Q Jin, Chinese Phys. Lett. **17**, 555 (2000).

[201] W. L. Vos and J. Schouten, J. App. Phys. **69**, 6744 (1991).

[202] D. D. Ragan, R. Gustavsen, and D. Schiferl, J. J. App. Phys. **72**, 5539 (1992).

[203] http://www.loto-eng.com/TecRep_dac.htm, retrieved from world wide web, March, 2001.

[204] This correction is from a pressure calculation program used in the Geophysical Laboratory of the Carnegie Institution of Washington.

[205] N. J. Hess and D. Schiferl, J. Appl. Phys. **68**, 1953 (1990); **71**, 2082 (1992).

[206] Y. Zhao, W. Barvosa-Carter, and S. D. Theiss *et al.*, J. of Appl. Phys. **84**, 4049 (1998).

[207] Jun Liu and Y. K. Vohra, AIP Conference Proceedings **309**, 1681 (1994).

[208] Q. Bi, J. M. Brown, and Y. Sato-Sorensen, J. Appl. Phys. **68**, 5357 (1990).

[209] K. Brister, Rev. Sci. Instrum. **68**, 1629 (1997).

[210] H. K. Mao, *Simple Molecular systems at very high density*, A. Polian, P. Loubeyre, and N. Boccara (ed.), Plenum Pressure, New York, 221 (1989).

[211] H. E. Lorenzana, M. Bennahmias, H. Radousky, and M. B. Kruger, Rev. Sci. Instrum. **65**, 3540 (1994).

[212] P. La B. Walling and J. R. Ferraro, Rev. Sci. Instrum. **49**, 1557 (1978).

[213] H. K. Mao and P. M. Bell, Rev. Sci. Instrum. **52**, 615 (1981).

[214] R. L. Reichlin, Rev. Sci. Instrum. **54**, 1674 (1983).

[215] Pu Feng-Nian, Ding Yu-Zheng, and Gou Qing-Quan, Sci. in China A **34**, 1339 (1991).

[216] D. Erskine and P. Y. Yu, Rev. Sci. Instrum. **58**, 406 (1987).

[217] T. A. Grzybowski and A. L. Ruoff, Phys. Rev. Lett. **53**, 489 (1984).

[218] D. Patel, T. E. Crumbaher, and J. R. Sites *et al.*, Rev. Sci. Instrum. **57**, 2795 (1986).

[219] N. Sakai, T. Kajiwara, K. Tsuji, and S. Minomura, Rev. Sci. Instrum. **53**, 499 (1982).

[220] J. van Straaten and I. F. Silvera, Rev. Sci. Instrum. **58**, 994 (1987).

[221] S. W. Tozer and H. E. King Jr, Rev. Sci. Instrum. **56**, 260 (1985); S. W. Tozer, Rev. Sci. Instrum. **64**, 2607 (1993).

[222] J. Gonzalez and J. M. Besson, Rev. Sci. Instrum. **57**, 106 (1986).

[223] J. Thomasson, Y. Dumont, J.-C. Griveau, and C. Ayache, Rev. Sci. Instrum. **68**, 1514 (1997).

[224] T. Hashimoto and A. Ikushima, Rev. Sci. Instrum. **51**, 378 (1980).

[225] M. J. Mackowski, K. E. West, and D. A. Samsel *et al.*, Cryogenics **16**, 45 (1976).

[226] G. J. Piermarini, S. Block, and J. d. Barnett, J. Appl. Phys. **44**, 5377 (1973).

[227] J. H. Burnett, H. M. Cheong, and W. Paul, Rev. Sci. Instrum. **61**, 3904 (1990).

[228] C. W. Chu, L. Gao, and F. Chen *et al.*, Nature (London) **365**, 323 (1993).

[229] M. Isobe, T. Ohta, and M. Onoda *et al.*, Phys. Rev. B **57**, 613 (1998).

[230] C. Y. Huang, J. G. Lin, and Z. J. Huang, Modern Phys. Lett. **9**, 1259 (1995).

[231] A. Matsushita, T. Yamanishi, and Y. Yamada *et al.*, Phyica C **227**, 254 (1994).

[232] *Low level measurements, precision DC current, voltage and resistance measurements*, Keithley.

[233] M. Imada, A. Fujimori, and Y. Tokura, Rev. of Mod. Phys. **70**, 1039 (1998).

[234] C. N. R. Rao and A. K. Cheetham, Adv. Mater. **9**, 1009 (1997).

[235] Hirotoshi Terashita and J. J. Neumeier, Phys. Rev. B **63**, 174436 (2001).

[236] R. Mahendiran, R. Mahesh, A. K. Raychaudhuri, and C. N. R. Rao, Phys. Rev. B **53**, 12160 (1996).

[237] C. Kapusta, P. C. Riedi, and W. Kocemba *et al.*, J. Phys.: Condens. Matter **11**, 4079 (1999).

[238] A. Maignan, C. Simion, V. Caignaert, and B. Raveau, J. Appl. Phys. **79**, 7891 (1996).

[239] J. Fontcuberta, B. Martínez, and A. Seffar *et al.*, Solid State Commun. **97**, 1033 (1996).

[240] J. Fontcuberta, B. Martínez, and A. Seffar *et al.*, Phys. Rev. Lett. **76**, 1122 (1996).

[241] Y. Tomioka, A. Asamitsu, and Y. Moritomo *et al.*, J. Phys. Soc. Jpn. **64**, 3626 (1995).

[242] A. Asamitsu, Y. Tomioka, and H. Kuwahara et al., Nature (London) **388**, 59 (1997).

[243] V. Kiryukhin, D. Casa, and J.P. Hill *et al.*, Nature (London) **386**, 813 (1997).

[244] D. E. Cox, P. G. Radaelli, M. Marezio, and S-W. Cheong, Phys. Rev. **57**, 3305 (1998).

[245] K. Miyano, T. Tanaka, Y. Tomioka, and Y. Tokura, Phys. Rev. Lett. **78**, 4257 (1997); T. Mori, K. Ogawa, and K. Yoshida *et al.*, J. Phys. Soc. Jpn. **66**, 3570 (1997).

[246] M. R. Lees, J. Barratt, and G. Balakrishnan *et al.*, Phys. Rev. B **52**, R14303 (1995).

[247] M. R. Lee, J. Barratt, and G. Balakrishnan *et al.*, J. Phys.: Condens. Matter **8**, 2967 (1996).

[248] J. Barratt, M. R. Lee, and G. Balakrishnan *et al.*, Appl. Phys. Lett. **68**, 424 (1996).

[249] V. Kiryukhin, D. Casa, and B. Keimer *et al.*, Mat. Res. Soc. Symp. Proc. **494**, 65 (1998).

[250] K. Ogawa, W. Wei, and K. Miyano *et al.*, Phys. Rev. B **57**, R15033 (1998).

[251] M. Fiebig, K. Miyano, and T. Satoh *et al.*, Phys. Rev. B **60**, 7944 (1999).

[252] M. Fiebig, K. Miyano, Y. Tomioka, and Y. Tokura, J. of Appl. Phys. **85**, 5561 (1999).

[253] V. Dediu, C. Ferdeghini, and F. C. Matacotta *et al.*, Phys. Rev. Lett. **84**, 4489(2000).

[254] H. Yoshizawa, H. Kawano, and Y. Tomioka *et al.*, Phys. Rev. B **52**, R13145 (1995).

[255] V. Dediu, C. Ferdeghini, and F. C. Matacotta *et al.*, Phys. Rev. Lett. **84**, 4489 (2000).

[256] Z. Jirák, S. Krupička, and Z. Šimša *et al.*, J. Magn. and Magn. Mat. **53**, 153 (1985).

[257] J. Aarts, S. Freisem, and R. Hendrikx *et al.*, Appl. Phys. Lett. **72**, 2975 (1998).

[258] R. A. Rao, D. Lavric, and T. K. Nath *et al.*, J. of Appl. Phys. 85, 4794 (1999).

[259] H. Yoshizawa, R. Kajimoto, and H. Kawano *et al.*, Phys. Rev. B 55, 2729 (1997).

[260] Congwu Cui, Trevor A. Tyson, and Zhong Zhong *et al.*, Phys. Rev. B **67**, 104107 (2003).

[261] H. Yoshizawa, H. Kawano, and Y. Tomioka *et al.*, Phys. Rev. B **52**, R13145 (1995).

[262] V. Dediu, C. Ferdeghini, and F. C. Matacotta *et al.*, Phys. Rev. Lett. **84**, 4489(2000).

[263] F. Rivadulla, M. A. López-Quintela, and L. E. Hueso *et al.*, Solid State Commun. **110**, 179 (1999).

[264] H. Kawano, R. Kajimoto, and H. Yoshizawa *et al.*, Phys. Rev. Lett. **78**, 4253 (1997).

[265] R. Mahendiran, M. R. Ibarra, and A. Maignan *et al.*, Phys. Rev. Lett. **82**, 2191 (1999).

[266] S. Zvyagin, A. Angerhofer, and K. V. Kamenev *et al.*, Solid State Commun. **121**, 117 (2002).

[267] H. Kuwahara, T. Okuda, and Y. Tomioka *et al.*, Mat. Res. Soc. Symp. Proc. **494**, 83 (1998).

[268] T. Hayashi, N. Miura, and K. Noda *et al.* Phys. Rev. B **65**, 024408 (2002).

[269] R. Kajimoto, H. Yoshizawa, and H. Kawano *et al.*, Phys. Rev. B **60**, 9506 (1999).

[270] V. Eremenko, S. Gnatchenko, and N. Makedonska *et al.*, Fizika Nizkikh Temperatur **27**, 1258 (2001).

[271] C. Ritter, R. Mahendiran, and M. R. Ibarra *et al.*, Phys. Rev. B **61**, R9229 (2000).

[272] P. Laffez, G. Van Tendeloo, and F. Millange *et al.*, Mater. Res. Bull. **31**, 905 (1996).

[273] Y. Moritomo, H. Kuwahara, and Y. Tokura, J. Phys. Soc. Jpn. **66**, 556 (1997).

[274] Taka-hisa Arima and Kenji Nakamura, Phys. Rev. B **60**, R15013 (1999).

[275] A. I. Abramovich, A. V. Michurin, O. Yu Gorbenko, and A. R. Kaul, J. Phys.: Condens. Matter **12**, L627 (2000).